On the Electrolytic Nature of Molten Aluminum and Rare Earth Oxides

by

Bradley Rex Nakanishi

B.S., Tufts University (2013)

Submitted to the Department of Materials Science and Engineering
in partial fulfillment of the requirements for the degree of

Doctor of Philosophy

at the

MASSACHUSETTS INSTITUTE OF TECHNOLOGY

February 2018

Author .....
Department of Materials Science and Engineering
November 22, 2018

Certified by .....
Antoine Allanore
Associate Professor of Metallurgy
Thesis Supervisor

Accepted by .....
Donald R. Sadoway
John F. Elliott Professor of Materials Chemistry
Chairman, Department Committee for Graduate Students

On the Electrolytic Nature of Molten Aluminum and Rare Earth Oxides

by

Bradley Rex Nakanishi

Submitted to the Department of Materials Science and Engineering
on November 22, 2018, in partial fulfillment of the
requirements for the degree of
Doctor of Philosophy

Abstract

The electrolytic cell method and its application for Gibbs energy measurement in high temperature, concentrated ionic melts was investigated. Previous challenges related primarily to signal interpretation during decomposition voltage measurement have hindered determination of Gibbs energy. An electrolytic cell method is proposed herein utilizing the sensitivity of large amplitude alternating current voltammetry, which enabled precise measurement of chemical potential during electrolytic decomposition.

A novel, containerless approach for electrochemical study of high temperature, reactive electrolytes in a molten pendant droplet is described. For the first time, melts of pure alumina, lanthana and yttria were electrolytically decomposed to metal alloy and oxygen gas using iridium electrodes.

The method was validated in molten alumina. Systematic investigation of the half-cell reactions corresponding to oxygen evolution and aluminum deposition revealed their electrochemical nature. Measurements of the chemical potential and partial molar entropy of aluminum in an iridium-rich, binary alloy liquid were obtained in close agreement with previous predictions.

The method was extended to the pseudo-binary system molten lanthana-yttria. The results revealed selective extraction of lanthanum and indicated that molten lanthana-yttria does not exhibit ideal mixing behavior, contradicting previous predictions. However, data interpretation in multicomponent electrolyte compositions were challenged primarily by a lack of thermodynamic data for the attendant alloy system and influence of dissolved oxygen on the observed alloy composition.

This work represents a pioneering effort for electrochemical operation in molten refractory oxides at temperatures above 2000 K.

Thesis Supervisor: Antoine Allanore
Title: Associate Professor of Metallurgy

Acknowledgments

This project would not have been possible without the contributions and support of many. In the words of Sir Isaac Newton, "If I have seen further than others, it is by standing upon the shoulders of giants." Thank you to those "giants" that stood before me.

My sincerest thank you to Professor Antoine Allanore, my mentor and thesis advisor, for all of your support and guidance. Our many conversations over the years going back to my days at Tufts have proven without fail to be energizing and inspiring. Thank you for challenging and believing in me. I am humbly grateful for the many opportunities and experiences I have had at MIT and beyond that without your enthusiasm would not have been possible.

To my committee members, Professors Don Sadoway, Ron Ballinger and Mike Short, thank you for all of your feedback, which significantly improved the quality of this work. I will continue to reflect on our conversations with great fondness.

A special thanks to Ms. Hilary Sheldon for your kindness and assistance.

To the Allanore Group members, you folks are amazing and inspiring. Thank you for your generous support and feedback. Many ideas that contributed to this project were conceived during our conversations with the help of a white board. In particular, I wish to thank Dr. Guillaume Lambotte and Ms. Sara Warkander for your pioneering efforts at the early stages of this project and Ms. Melody Wang and Mr. Erick Hernandez for your contributions to this work.

Thank you to the DMSE staff and instructors for your assistance. You have contributed in various ways to this project and beyond for which I will forever be grateful.

Thank you, Professor Checkelsky, for allowing me to use your laboratory's thermal imaging furnace at the early stages of this work. Thank you, Dr. Nilanjan Chatterjee, for all your help with the electron probe microanalyzer work.

To the folks I met from Tohoku University, thank you for making my stay in Japan so rewarding and enjoyable. Thanks to the Tohoku MD Program for sponsoring my

visit. Professor Osamu Takeda, thank you for your help and guidance. Our brief time collaborating was inspiring. Also, thank you, Professor Hongmin Zhu, for hosting me in your laboratory and our exhilarating discussions. Thank you Dr. Lu Xin for your generous help and support during my stay with the Zhu Group.

I would like to acknowledge that various funding sources that enabled this work and my studies at MIT: the Danae and Vasilis Salapatas Endowed Fellowship and the US Office of Naval Research under grant Contract # N00014-11-1-0657.

Thank you to my friends from MIT and afar for the laughs and encouragement during times good and bad.

Thank you to my parents, Greg and Sue, and brother, Kurt, for your unyielding love, support and generosity.

Last but not least, thank you to my fiancé, Kayley, for your continuous love, patience and support through the many challenges we encountered on this journey.

Contents

List of Figures

List of Tables

Nomenclature

Fundamental Physical Constants

F	Faraday constant	$9.64853399(24) \times 10^4$ C mol^{-1}
R	gas constant	8.314472(15) J mol^{-1} K^{-1}

Symbols

β_n	n$^{\text{th}}$ order fitting parameter	*varies*
χ	Pauling electronegativity	
$\varnothing$	diameter	m
η	overpotential	V
γ_i^∞	Henrian (infinite dilution) activity coefficient of species i	
γ_i	activity coefficient of species i	
μ_i^o	standard chemical potential of species i	J mol^{-1}
μ_i	chemical potential (partial molar Gibbs energy) of species i	J mol^{-1}
ν	scan rate	V s^{-1}
ω	angular frequency	rad s^{-1}
ω_{ij}	regular solution model parameter, binary i,j component solution	J mol^{-1}
ϕ	inner electric (Galvani) potential	V

ρ	density	g m^{-3}
σ	electric conductivity	S m^{-1}
σ	standard deviation	*varies*
A	area	m^2
A_G	geometric surface area	m^2
a_i	activity of species i	
C_i	concentration of species i	mol m^{-3}
E	electrode potential (versus a reference)	V
E^o	standard electrode potential	V
E_g	electronic band gap	eV
E_{ac}	applied potential AC amplitude	V
f	frequency	Hz
G	Gibbs energy	J mol^{-1}
G_i^E	partial molar excess Gibbs energy of species i	J mol^{-1}
H	enthalpy	J mol^{-1}
I	electric current	A
$I_{n\omega}$	n^{th} harmonic of electric current	A
j	electric current denisty	A m^{-2}
n	number of electrons	
p	pressure	Pa
p_i^o	vapor pressure of condensed species i	Pa

p_i	partial pressure of species i	Pa
Q	electric charge	C
r	radius	m
R_u	uncompensated resistance	Ω
R_{cell}	cell resistance	Ω
R_{ct}	charge transfer resistance	Ω
R_c	compensated resistance	Ω
R_{ext}	external resistance	Ω
R_s	solution resistance	Ω
S	entropy	J mol^{-1} K^{-1}
S_i	partial molar entropy of species i	J mol^{-1} K^{-1}
T	temperature	K
t	time	s
T_{fus}	melting temperature	K
U	decompostion voltage, cell potential difference	V
V	cell voltage (measured)	V
V_m	molar volume	m^3 mol^{-1}
x	alloy composition parameter (defined in §7)	
X_i	mole fraction of species i	
z	alloy composition parameter (defined in §7)	
Z_i	atomic number	

Abbreviations

ac alternating current

ACV large amplitude alternating current voltammetry

BSE back-scattered electron

CALPHAD CALculation of PHase Diagrams

CE counter electrode

DAQ data acquisition module

dc direct current

EDS energy-dispersive X-ray spectroscopy

EIS electrochemical impedance spectroscopy

FT Fourier transform

MOE molten oxide electrolysis

OCP open circuit potential

RE reference electrode

REE rare earth element

REO rare earth oxide

SPC structure-property-composition

TIF thermal imaging furnace

UHT ultra-high temperature

WDS wavelength-dispersive X-ray spectroscopy

WE working electrode

Chapter 1

Introduction

Materials processing via the liquid state of matter has enabled enhanced productivity and scale in numerous applications ranging from primary materials extraction to energy-matter conversion. In the present "materials age" [1], [2], society demands access to a greater quantity and diversity of materials. Liquid state synthesis and extraction of materials represents a promising approach for scaling technologies to address increasing material demands in the context of *sustainability*. More fundamentally, a description for the properties and behavior of melts are important to understanding phenomena in geophysics and planetary science [3]–[5].

Our understanding of the liquid state has important implications for developing solid state materials, as well. Structural materials for aerospace, and nuclear applications, oftentimes are required to perform in high temperature conditions. Phenomena occurring in the solid state such as diffusion or creep are strongly correlated [6] to the liquidus, or melting temperature. Prediction of the melting temperatures of materials, even pure elements, remains an area of active development [7], [8]. As Grimvall noted [9], "A theory of melting should consider the Gibbs energy of both the solid and the liquid phases." Therefore, a sound description of the behavior and stability of solid state materials at high temperature requires an accurate description for the properties of the liquid state.

Therefore, our understanding of the liquid state of matter has, is and will continue to be essential for the development of technologies that address society's greatest

challenges, such as energy and climate change. Contrasting with this fact is the present lack of understanding and property prediction for liquids.

1.1 The materials problem

The general problem of materials science has been formulated in numerous ways, e.g. see [10]–[12], and is oftentimes related to the generation structure-property-composition (SPC) relationships. In the context of the present work, the materials problem as it pertains to two relevant applications involving oxide melts for high temperature metallurgical processing is summarized in the following subsections. These applications were selected in part due to their mutual significance (present and potential, resp.) with respect to *sustainability*.

A discussion of SPC relationships is incomplete without mentioning thermodynamics and, more specifically, the CALPHAD method (to be reviewed in §1.1.3) in regards to relating structure and composition to the macroscopic, equilibrium properties of materials. Furthermore, thermodynamics represents a rigorous basis for modeling dynamic processes and has been utilized to describe SPC relationships for material transport properties, such as viscosity and diffusivity [13]–[17], as well.

1.1.1 Pyrometallurgical processing

Oxide melts, or *slags*, form upon removal of gangue materials during the pyrometallurgical extraction and refining of metals (e.g. iron) from their oxide ores. Focusing on productivity, the materials problem involves slag design for improved chemical and physical separation of the product metal [18]. Thanks in part to significant commercial smelting interest (also geology and glassmaking communities) [4], [19]–[21], considerable progress has been made towards establishing SPC relationships for silica-based oxide melts aimed at increasing smelting yields for commodity metals, e.g. iron and copper. For instance, consider that 1,600 Mt of raw steel valued at around US$400/t were produced globally in 2016[1]. However, in the same time period, around

[1]Equivalently, enough steel for three Empire State Buildings per hour!

460 to 600 Mt of slag were generated during the pig iron and steelmaking processes with a value of only US$20/t [22]. This situation represents a serious societal challenge in the context of sustainability. As emphasized by Waseda and Toguri, the "beneficial utilization of metallurgical slags and waste reduction techniques are among the more important technological and social developments of the 21st century" [23]. An improved understanding of SPC relationships in oxide melts is foreseen to benefit both improvements to pyrometallurgical processing productivity and developments for economically-viable slag recycling.

1.1.2 Electrometallurgical processing

The electrification of metallurgical extraction and recovery via electrochemical processing is a promising pathway towards significantly reducing anthropogenic greenhouse gas emissions [24]. Using electrochemistry, electrons may replace carbon and other environmentally harmful chemicals as the fuel and selective reductant. Furthermore, liquid state processing, exhibiting superior heat and mass transport and reaction rates versus solid-state processing, is foreseen to benefit the reliable and efficient material supply for societal demands. Aluminum production via the Hall-Héroult process exemplifies liquid state, electrometallurgical extraction, but potential opportunities remain for improving aluminum processing [25] and developing similar technologies for the extraction of other metals, as well [26].

For example, molten oxide electrolysis (MOE), an understudied technique for extracting metals from their oxide ore in a molten oxide electrolyte, features both electrochemical extraction and liquid state processing [24], [27]–[33]. During MOE, molten or gaseous metal is reduced directly from a molten oxide electrolyte using electricity. This process has been studied on the laboratory scale for base metals (e.g. Fe) in silica-based electrolytes [30], [32]. When an inert anode is employed oxygen is produced [24], a valuable resource in extraterrestrial applications for fuel and life support [31]. Today, less than one tonne of metal is produced annually by molten oxide electrolysis. Nevertheless, MOE represents a promising technology for the electrification of oxide ore processing and metal recovery, enabling a significant

reduction in primary carbon emissions and direct integration into the electrical grid [26]. An MOE cell interfaced with an electrical grid composed of significant fractions variable renewable energy (e.g. solar photovoltaic or wind) provides a means for grid-level power regulation [34].

Significant challenges remain for possible extension of MOE to reactive[2] metals. As highlighted by Allanore [28], the design of a suitable supporting electrolyte for the extraction of the targeted metal represents a key challenge. For the extraction of reactive metals, a silica-based electrolyte is unsuitable due to its relatively low stability [35]. Therefore, extension of MOE to reactive metal recovery is foreseen to involve silica-free oxide electrolytes, for which SPC relationships are extremely underdeveloped.

1.1.3 The CALPHAD method

The CALPHAD (CALculation of PHase Diagrams) method is a numerical approach for thermodynamic calculations, see [10], [36]–[40] for more detailed descriptions. Kaufman, one of the founding pioneers of the method, recently described CALPHAD as "unique, in that it is neither empirical nor fundamental" and satisfies the requirements of the materials genome initiative [10]. Early on, CALPHAD competed with electron band theory for describing the features of phase diagrams and chemical equilibria, but ultimately won out for its generality and quantitative nature [36]. The main objective of CALPHAD is to provide a numerical description of the Gibbs energy (G) and its variation with state variables, such as temperature (T), pressure (p), and composition (X_i). Conveniently, G variation for large changes in state variables can oftentimes be modeled with a relatively small set of parameters, allowing ready storage and retrieval from databases for thermodynamic calculations. A CALPHAD assessment of G involves [10]:

1. selection of available data (phase equilibria and thermochemical) to be represented,

[2]Herein, "reactive" applies to elements more reactive with oxygen than silicon, e.g. aluminum, titanium, the lanthanides, etc.

2. selection of thermodynamic models,

3. fitting model parameters to achieve the best representation of data, and

4. incorporation of model parameters into a database.

A key feature of CALPHAD method is that the same diversity of information obtained from G and its derivatives can be used to refine models for G. Today, phase equilibria and thermochemical data are obtained from experiments and *ab initio* methods. At present, application of CALPHAD to high temperature liquids is challenged by [41]: 1) immaturity of *ab initio* prediction in regards to throughput analysis over large changes in composition and state variables, 2) lack of physical basis in current CALPHAD models, and 3) missing experimental data for high temperature liquids.

Prediction by *ab initio* methods (e.g. ab initio molecular dynamics) can be employed to supplement data otherwise inaccessible by experiment, e.g. lattice stabilities [38] or heat capacities [41], and provide high-throughput property prediction for crystalline solids [42]. Some researchers have further asserted that *ab initio* methods have altered the paradigm for the materials design process [38]. Certainly, the reliability of thermochemical data prediction at zero kelvin (prediction of enthalpy H) and moderate temperatures in crystalline, periodic materials is mature [43]. Perhaps, all data will be computed without the need for experimental input one day. However, the time-consuming nature, ambiguity for interatomic potential selection, and present accuracy of computational methods limit at present the utility of *ab initio* methods for predicting properties of liquids [41], [44]. At high temperatures, where entropy S is expected to play a more important role in the Gibbs energy ($G = H - TS$), prediction of S remains a challenge for the solid state [45] and, especially, for the liquid state where long range order is lacking [9], [41], [46]. For instance, melting temperature prediction for the pure elements remains a subject of considerable debate [8], [9], [41].

The selection of appropriate CALPHAD models remains a key challenge [41]. During the early stages of CALPHAD at a time of limited computational power,

the ideal solution model was employed for describing relatively simple binary alloy systems, e.g. Nb-Re or Co-Ni [47]. Today, a multitude of models exist, such as the compound energy formalism [48]–[50] or modified quasichemical model [51]–[54], to account for non-ideal interactions. However, as noted by Navrotsky [3], thermodynamic models become more accurate at the cost of empiricism (less physical) and poor extrapolation. Therefore, the demands of industrial applications (e.g. smelting of steel, copper and aluminum) have contributed to the extensive development of accurate, yet largely empirical databases [55].

Since CALPHAD's beginning, the connection between model parameters and the physical nature of melts has kept many in the scientific community skeptical of the CALPHAD method's utility. To quote the criticisms of Oates et al. [56]:

> A greater effort should be made to adapt the ideas from the ab initio calculations whilst retaining the empirical nature of a solution model rather than remain content with a numerical representation which...fit[s] experimental data [well]...[It] may be difficult to prove these advantages...if the sole aim of the calculation is the empirical fitting of the phase boundaries of a binary system.

Unfortunately, phase boundary fitting remains a popular objective for CALPHAD assessments [38]. When no thermochemical data is available for the liquid, common practice in the literature assumes ideal mixing entropy for the liquid phase and empirically fits mixing enthalpy to match phase boundaries, e.g. [57]–[59]. Perhaps, this approach may originate from demands of mathematical simplicity during the early stages of CALPHAD [47], [60]. Certainly, uncertainty remains for the thermodynamic description of the liquid phase with extrapolation to higher order systems. Despite efforts to include more physics in CALPHAD models [56], the CALPHAD community has continued empirically assessing fitting parameters with the principle goal of reproducing measured phase boundaries [38], [58], [59].

Therefore, the generation of reliable experimental data has and will continue to play an essential role in the utility and development of CALPHAD, especially, as

applied to the liquid state of matter.

1.2 Experimental generation of thermodynamic data for liquids

As discussed in previous section, the generation of experimental data remains an essential part of thermodynamics and the CALPHAD method. An accurate description of G is required for reliable chemical equilibria and phase diagram prediction. Unfortunately, such descriptions of G for high temperature liquids are oftentimes limited or missing, which is likely attributed to the material compatibility challenges. Previous techniques for generating thermochemical data are reviewed in detail elsewhere [3], [20], [61], [62]. The state of the art is briefly reviewed here for equilibration, vapor pressure and electrochemical measurements. Particular attention is given to the electrolytic cell method because treatments in modern texts are severely lacking [3], [20], [36], [61]. Other methods, such as spectroscopy, diffractometry and calorimetry, have a role in thermodynamic property generation, but the discussion is limited herein to those methods providing direct measurement of G.

For equilibration methods, the experimentalist is tasked with constructing an equilibration cell in which the various phases are allowed to achieve equilibrium under the relevant conditions of (T, p, X_i) [20], [61]. While variation in G can be determined rather straightforwardly in theory, construction of the envisaged equilibration cell may prove challenging in practice. Furthermore, *ex situ* composition measurements following equilibration are required for one data point at a single (T, p, X_i). Optimizing throughput for significant (T, p, X_i) variation may prove extremely challenging in novel or understudied molten systems.

While numerous vapor pressure measurement techniques have been formulated [61], the methods based upon Knudsen effusion and vapor transpiration are the most relevant for investigating melts at high temperature [62]. Since the mid-1960s, mass spectrometers have greatly enhanced Knudsen effusion analysis for materials exhibi-

ting complex vapor species [63]. The lower limit of mass spectrometer detection is around 10^{-2} Pa, which is problematic for materials exhibiting particularly low vapor pressures [61], [63]. Challenges pertaining to the selection of suitable container and lid materials have prevented extension of the coupled Knudsen effusion methods to reactive melts with high melting temperatures. Alternatively for these materials, containerless vapor transpiration methods have been developed, circumnavigating the container-based challenges. For example, Mills et al. [64] determined activities in Fe-Ni melts using electromagnetic levitation from 2178 to 2558 K. Given that this approach relates ratios of evaporative fluxes (vapor species diffusivities) to melt component activities, Gibbs-Duhem integration (investigation over full composition range) is required for determining individual component activities and the accuracy of this method is a concern for melts with a complex vapor phase. Furthermore, practical concerns (e.g. measurement duration) remain for those components exhibiting particularly low vapor pressures (< 100 Pa) [64].

For melts exhibiting ionic behavior, methods based upon the electrochemical principles described by Sir M. Faraday some 183 years ago [65] remain "the most direct method of measuring Gibbs energies of reaction" [61]. Under certain conditions, the reaction Gibbs energy $\Delta_r G$ is proportional to an electric potential difference U:

$$\Delta_r G = -nFU \tag{1.1}$$

where n is the number of electrons passed per mole of reaction and F ($= 96,485$ C mol^{-1}) is Faraday's constant. In theory, employing such an approach enables the direct, continuous, precise, *in situ* determination of G while varying $(T, p, X_i, ...)$ [66]. Electrochemical techniques can be categorized into two groups involving measurements of:

- limiting cell potential at zero current (galvanic cell), or
- decomposition voltage (electrolytic cell).

The relevant features and historical developments of each of these techniques are to

be reviewed in the following two sections. The principal challenges shared by both approaches are electrolyte selection and electrode design.

1.2.1 Galvanic cell method

For galvanic cell measurements, the experimentalist is tasked with constructing a suitable galvanic cell from which the potential difference measured at open circuit conditions is the reversible cell potential (formerly termed electromotive force) for the overall desired reaction. This is achieved when an electrolyte conducting electricity by the migration of ions only is employed. In reality, a very small current must flow through the cell in order to practically obtain a voltage measurement. Therefore, a further constraint is that the electrode processes must obtain equilibrium at a rate much faster than the reactions induced by the very small net current can alter the state of the electrodes (reversibility).

A further reality is that many electrolytes conduct electricity by a mixture of ion *and* electron migration. If the electronic conduction in the electrolyte becomes significant, then the galvanic cell will self-dissipate as the cell potential difference drifts towards null. Prediction of the self-dissipation's influence on the conditions at the electrodes with time is oftentimes untenable. Therefore, minimization of electronic conduction is an essential component for reliable cell potential measurement. Typically, an ion-conducting membrane is inserted between electrodes compartments to serve as an *electron barrier*. The galvanic method has received substantial development in electrolytes based on aqueous solutions, molten salts, molten oxides, ionic liquids, organic solvents, and solid electrolytes (glass, stabilized zirconia, BaF_2 and beta alumina) [refs]. Nevertheless, developments of suitable membranes and materials for cell containers for reactive and high melting materials remains a significant challenge, which has severely limited application of the galvanic method.

1.2.2 Electrolytic cell method

Electrolytic cell methods involving measurements of the decomposition voltage (cell potential difference) have been utilized since the time of Sir Humphrey Davy to measure the minimum electrochemical work required to decompose ionic substances. Historically, decomposition voltage measurements have been regarded as experimentally challenging and "generally much less accurate" [66], [67] for thermodynamic property measurements because the cell is operated with current flow, usually far away from null current conditions. However, where galvanic cells are impractical to construct, the electrolytic cell allows the experimentalist to impose a condition at the anode and cathode and monitor the associated potential difference without the requirements of a membrane or, even, a container.

The most recent and thorough review of the electrolytic cell method to the author's knowledge is that of Delimarskii and Markov [67], which includes a summary of the Soviet literature prior to 1958. Additionally, Janz [68] reviewed decomposition voltage measurements obtained prior to 1967. Nevertheless, applications of the electrolytic cell method in various forms continue to be reported for a variety of high temperature melts (e.g. see [69]–[76]) employing various methodologies. Therefore, an updated review of the fundamental principles of the electrolytic cell method as applied to thermodynamic property measurement is pertinent.

The measured cell voltage V during the passage of current may generally be described by [25], [67], [77]–[79]:

$$V = U^o + \eta_{conc.} + IR_{cell} + \eta_{act.} \tag{1.2}$$

where U^o is the standard decomposition potential difference, IR_{cell} is ohmic drop contribution due to the net current I flowing through the cell with resistance R_{cell}, $\eta_{conc.}$ is the concentration [77] (mass transfer [79]) overpotential, and $\eta_{act.}$ is the activation [77] (charge transfer [79]) overpotential[3]. Although it is somewhat arbitrary,

[3]Here, $\eta_{act.}$ and $\eta_{conc.}$ include contributions from reactions occurring at both the anode and cathode

definition of the standard state in regards to U^o is usually taken as as the cel voltage at null current conditions. The thermodynamic significance of $U = U^o + \eta_{conc.}$ is given by Eq. 1.1. To relate the measurable quantity V to thermodynamic quantities via Eq. 1.1 the various contributions contained in Eq. 1.2 must be determined.

If the reaction taking place at a *working* electrode (WE) is studied[4] via utilization of a *reference* electrode (RE) providing a fixed, well-defined energy level of reference, then a similar expression to Eq. 1.2 describes the *applied* WE potential E:

$$E = E^o + \eta_{conc.}(WE) + IR_u + \eta_{act.}(WE) \tag{1.3}$$

where E^o is the standard electrode potential, R_u is the uncompensated resistance, $\eta_{conc.}(WE)$ and $\eta_{act.}(WE)$ are respectively the concentration and activation overpotentials for the WE with respect to RE. Similarly to V, the problem of relating E to thermodynamic quantities emerges requiring determination of the various contributions in 1.3.

Delimarskii and Markov described two methods of decomposition voltage measurement: 1) "Le Blanc's I-V curves" method and 2) the "commutator" method [67]. Historically, the method of extrapolation to null current has been employed to relate measured voltages to thermodynamic quantities [80]–[82]. However, for situations involving concurrent reactions or electronic conduction, this type of extrapolation is crude at best. A better approach is directly accounting for the various contributions or careful selection of conditions for which one or more of the aforementioned contributions may be neglected.

Nowadays, transient electrochemical techniques are well-established for decomposition voltage measurements involving dilute reacting species, e.g. cyclic voltammetry [70]–[72], [75], square-wave voltammetry [73], [74], [83], chronopotentiometry [84] or chronoamperometry [69]. Exact or approximate expressions have been derived to relate the features of the current (or voltage) response to thermophysical and thermochemical properties of the reactions and species involved [79], which permits

[4] A typical feature in electrochemistry, a third electrode, the *counter* electrode (CE), completes the electrical circuit by supplying the current.

identification of reactions and precise correlation of the measured potential to thermodynamic quantities ($\eta_{conc.}$ and $\eta_{act.}$). Presently, application of transient techniques have been limited to reactions exhibiting specific features (e.g. soluble reactants and products [79] or metal deposition on an inert substrate [85]–[87]) with moderate solute concentrations in a supporting electrolyte (i.e. negligible ion migration). This is precisely the most developed realm of electrochemical polarographic theory [79].

However, there is a broad class of electrolytes for which electrolytic cell investigations have historically been extremely limited [69], [82], i.e. concentrated electrolytes [5]. From an applied perspective, elimination of a supporting electrolyte decreases the work requirement (minimum cell voltage) for decomposition [6] and maximizes productivity [7]. However, practically speaking, industrial applications have avoided such processes due to the solubility of parent metals in their pure, molten halogen salts and concomitant implications for poor faradaic efficiency arising from electronic conduction, e.g Na in NaCl or Mg in $MgCl_2$ [88]. From an electrochemical theory perspective, investigations without the presence of a supporting electrolyte "complicate" the kinetic and mass transport analysis, specifically, resulting in situations involving non-negligible ion migration contributions to mass transfer (diffusion is no longer the sole operative mode), higher solution resistance, "thickening" of the double-layer structure, and non-uniform ionic strength throughout the solution during the consumption or production of ions at electrodes [79].

The recently reported investigation by Uda et al. [82] illustrates the general challenges for reliable and accurate implementation of the electrolytic cell method in concentrated electrolytes Uda et al. measured the Gibbs energy of formation of $DyCl_2$(l) $\Delta_f G^o_{DyCl_2}$ at $T = 1073$ K with a discrepancy of approximately 38 kJ mol^{-1} (7%) between those values determined by decomposition voltage and phase equilibration measurements. Despite the approximate nature of their calculations (missing thermodynamic data for the Mg-Dy liquid alloy phase), they reasoned that the va-

[5]Herein "concentrated" is tentatively defined as electrolytes where the reacting species has a concentration $C_i \gg 0.1$ M

[6]$\Delta_r G$ is proportional to logarithm of activity of the reacting species in the electrolyte (a_i), so U^o is minimum when $a_i \to 1$.

[7]current density is proportional to the reacting specie's concentration, i.e. $j \propto C_i$.

lue determined from phase equilibration measurements to be more reliable given its agreement with their experimentally determined phase diagram and estimates for $\Delta_f G^o_{DyCl_2}(1073\ K)$ from previous calorimetric measurements. They attributed the more positive (lower magnitude) value for $\Delta_f G^o_{DyCl_2}(1073\ K)$ obtained from decomposition voltage measurements to the presence of electronic conduction giving rise to a partial short-circuiting of the cell. Despite the very thorough analysis of their work, they did not mention ohmic drop (currents 1 A at the decomposition voltage) nor verify the behavior of the RE employed. Furthermore, their method for determining the standard potential for chlorine evolution lacks justification and rigor, given the obscuring effect of the detected Dy^{2+}/Dy^{3+} oxidative wave, likely influence of double layer charging current and possibility of kinetic effects (activation overpotential).

Generally, it may be concluded that the electrolytic cell method as applied to concentrated electrolytes has been challenged by the following [67], [69], [82]:

- inconsistent or unreliable ohmic drop compensation,
- electronic conductivity depolarization,
- activation polarization contributions, and
- signal interpretation and their correlation with the states of reactants and products.

1.3 Focus of the present work

In the previous sections, it was observed that the electrolytic cell method is underdeveloped for Gibbs energy measurement in concentrated ionic melts. Interestingly, the CALPHAD method oftentimes utilizes descriptions for binary systems as a basis for extrapolation of properties in higher-order systems. The Gibbs energy description for liquid phase in such concentrated systems is usually poorly informed at high temperature, which presents a serious problem for extrapolation within the CALPHAD framework. Therefore, the present work seeks to explore conditions where the elec-

trolytic cell method provides reliable measurement of Gibbs energy in concentrated melts.

1.4 Summary

Thermodynamics and its embodiment within the CALPHAD framework represents a powerful way of quantitatively describing structure-property-composition relationships for the liquid state. However, the generation of reliable Gibbs energy data remains an essential part of the CALPHAD approach, and significant challenges remain for property prediction and measurement in high temperature melts.

Methods of property prediction involving *ab initio* calculations remain computationally prohibitive for the complex, disordered liquid state. On the other hand, experimental difficulties at high temperature are often associated with material compatibility challenges for the container or membrane.

Alternatively, the electrolytic cell method does not necessarily require such components while implicitly offering *in situ*, precise, continuous, direct measurement of Gibbs energy. The electrolytic cell method as applied to Gibbs energy measurement for dilute components in a supporting electrolyte are well-established. However, application of the electrolytic cell method to concentrated melts has been extremely limited, and the apparent challenges for studying such systems by means of decomposition voltage measurements were examined.

References

[1] D. S. Abraham, *The Elements of Power: Gadgets, Guns, and the Struggle for a Sustainable Future in the Rare Metal Age*. New Haven: Yale University Press, 2015.

[2] T. E. Graedel, E. M. Harper, N. T. Nassar, and B. K. Reck, "On the materials basis of modern society.," *Proc. Natl. Acad. Sci. U. S. A.*, vol. 2013, 2013.

[3] A. Navrotsky, *Physics and Chemistry of Earth Materials*. Cambridge: Cambridge University Press, 1994, p. 417.

[4] B. O. Mysen and P. Richet, *Silicate Glasses and Melts Properties and Structure*, 1st ed. Boston: Elsevier, 2005, p. 560.

[5] K. Hirose, G. Morard, R. Sinmyo, K. Umemoto, J. W. Hernlund, and S. Labrosse, "SiO_2 crystallization and compositional evolution of the Earth's core," *Nature*, vol. 543, no. 7643, pp. 99–102, 2016.

[6] A. Brown and M. Ashby, "Correlations for diffusion constants," *Acta Metall.*, vol. 28, no. 8, pp. 1085–1101, 1980.

[7] R. W. Cahn, "Melting from within," *Nature*, vol. 413, no. October, pp. 582–583, 2001.

[8] Z. Jin, P. Gumbsch, K. Lu, and E. Ma, "Melting mechanisms at the limit of superheating," *Phys. Rev. Lett.*, vol. 87, no. 5, p. 055 703, 2001.

[9] G. Grimvall, *Thermophysical Properties of Matter*. Amsterdam: North-Holland, 1999, p. 424.

[10] L. Kaufman and J. Ågren, "CALPHAD, first and second generation - Birth of the materials genome," *Scr. Mater.*, vol. 70, no. 1, pp. 3–6, 2014.

[11] A. Jain, S. P. Ong, G. Hautier, W. Chen, S. Richards, William Davidson Dacek, S. Cholia, D. Gunter, D. Skinner, G. Ceder, and K. A. Persson, "The Materials Project: A materials genome approach to accelerating materials innovation," *APL Mater.*, vol. 1, no. 1, p. 011 002, 2013.

[12] W. Xiong and G. B. Olson, "Integrated computational materials design for high-performance alloys," *Mater. Res. Soc. Bull.*, vol. 40, no. 12, pp. 1035–1044, 2015.

[13] R. F. Brooks, A. T. Dinsdale, and P. N. Quested, "The measurement of viscosity of alloys–a review of methods, data and models," *Meas. Sci. Technol.*, vol. 16, no. 2, pp. 354–362, 2005.

[14] R. E. Aune, M. Hayashi, and S. Sridhar, "Thermodynamic approach to physical properties of silicate melts," *Ironmak. Steelmak.*, vol. 32, no. 2, pp. 141–150, 2005.

[15] B. A. Shakhmatkin, N. M. Vedishcheva, and A. C. Wright, "Can thermodynamics relate the properties of melts and glasses to their structure?" *J. Non. Cryst. Solids*, vol. 293-295, no. 1, pp. 220–226, 2001.

[16] B. A. Shakhmatkin and N. M. Vedishcheva, "A thermodynamic approach to the modeling of physical properties of oxide glasses," *Glas. Phys. Chem.*, vol. 24, no. 3, pp. 229–236, 1998.

[17] D. U. Sichen, J. N. Bygdi, and S. Seetharaman, "A model for estimation of viscosities of complex metallic and ionic melts," *Metall. Mater. Trans. B*, vol. 25, pp. 519–525, 1994.

[18] Nobuo Sano, "Thermodynamics of slags," in *Adv. Phys. Chem. Process Metall.* N. Sano, W.-K. Lu, and P. V. Ribound, Eds., Academic Press, 1997, pp. 45–86.

[19] F. D. Richardson, *Physical Chemistry of Melts in Metallurgy*. New York: Academic Press Inc., 1974, p. 537.

[20] E. Turkdogan, *Physicochemical Properties of Molten Slags and Glasses*. London: Metals Society, 1983.

[21] M. Allibert, H. Gaye, J. Geiseler, D. Janke, B. Keene, D. Kirner, M. Kowalski, J. Lehmann, K. C. Mills, D. Neuschutz, R. Parra, C. Saint-Jours, P. Spencer, M. Susa, M. Tmar, and E. Woermann, *Slag Atlas*, 2nd ed., V. D. Eisenhuttenleute, Ed. Verlag Stahleisen GmbH, 1995, p. 616.

[22] U.S. Geological Survey, *Mineral Commodity Summaries 2017: U.S. Geological Survey*. 2017, p. 202.

[23] Y. Waseda and J. M. Toguri, *The structure and properties of oxide melts*. River Edge: World Scientific, 1998, p. 236.

[24] A. Allanore, L. Yin, and D. R. Sadoway, "A new anode material for oxygen evolution in molten oxide electrolysis.," *Nature*, vol. 497, no. 7449, pp. 353–6, 2013.

[25] N. Jarrett, "United States extractive metallurgy-The 80's and beyond," *Metall. Trans. B*, vol. 18, no. 6, pp. 289–313, 1987.

[26] A. Allanore, "Electrocehmical engineering for commodity metals extraction," *Electrochem. Soc. Interface*, vol. 26, no. 2, pp. 63–68, 2017.

[27] D. R. Sadoway, "The electrochemical processing of refractory metals," *JOM*, vol. 43, no. 7, pp. 15–19, 1991.

[28] A. Allanore, "Features and challenges of molten oxide electrolytes for metal extraction," *J. Electrochem. Soc.*, vol. 162, no. 1, pp. 13–22, 2014.

[29] D. Fray and F. Derek, "Iron production electrified," *Nature*, vol. 497, no. 7449, pp. 324–325, 2013.

[30] D. Wang, A. J. Gmitter, and D. R. Sadoway, "Production of oxygen gas and liquid metal by electrochemical decomposition of molten iron oxide," *J. Electrochem. Soc.*, vol. 158, no. 6, E51–E54, 2011.

[31] A. H. C. Sirk, D. R. Sadoway, and L. Sibille, "Direct electrolysis of molten lunar regolith for the production of oxygen and metals on the moon," *ECS Trans.*, vol. 28, no. 6, pp. 367–373, 2010.

[32] H. Kim, J. Paramore, A. Allanore, and D. R. Sadoway, "Stability of iridium anode in molten oxide electrolysis for ironmaking: influence of slag basicity," *ECS Trans.*, vol. 33, no. 7, pp. 219–230, 2010.

[33] N. A. Fried and D. R. Sadoway, "Titanium extraction by molten oxide electrolysis," *TMS Conf. (Charlotte, NC)*, 2004.

[34] B. Kroposki, B. Johnson, P. Denholm, and B.-m. Hodge, "Achieving a 100% renewable grid," *IEEE Power Energy Mag.*, pp. 61–73, 2017.

[35] B. R. Nakanishi, G. Lambotte, and A. Allanore, "Ultra high temperature rare earth metal extraction by electrolysis," in *Rare Met. Technol. 2015*, N. R. Neelameggham, S. Alam, H. Oosterhof, A. Jha, D. Dreisinger, and S. Wang, Eds., TMS (The Minerals, Metals & Materials Society), 2015, pp. 177–183.

[36] N. Saunders and A. P. Miodownik, *CALPHAD (Calculation of Phase Diagrams): A Comprehensive Guide*. New York: Elsevier Science Inc., 1998, p. 479.

[37] G. Kaptay, "Nano-Calphad : extension of the Calphad method to systems with nano-phases and complexions," *J. Mater. Sci.*, vol. 47, pp. 8320–8335, 2012.

[38] Z.-K. Liu, "First-principles calculations and CALPHAD modeling of thermodynamics," *J. Phase Equilibria Diffus.*, vol. 30, no. 5, pp. 517–534, 2009.

[39] H. L. Lukas, S. G. Fries, and B. Sundman, *Computational Thermodynamics*. New York: Cambridge University Press, 2007, p. 313.

[40] C. H. P. Lupis, *Chemical Thermodynamics of Materials*. New York: North-Holland, 1983, p. 581.

[41] C. A. Becker, J. Ågren, M. Baricco, Q. Chen, S. A. Decterov, U. R. Kattner, J. H. Perepezko, G. R. Pottlacher, and M. Selleby, "Thermodynamic modelling of liquids: CALPHAD approaches and contributions from statistical physics," *Phys. Status Solidi Basic Res.*, vol. 251, no. 1, pp. 33–52, 2014.

[42] S. Curtarolo, G. L. W. Hart, M. B. Nardelli, N. Mingo, S. Sanvito, and O. Levy, "The high-throughput highway to computational materials design.," *Nat. Mater.*, vol. 12, no. 3, pp. 191–201, 2013.

[43] S. Curtarolo, D. Morgan, and G. Ceder, "Accuracy of ab initio methods in predicting the crystal structures of metals: A review of 80 binary alloys," *Calphad*, vol. 29, no. 3, pp. 163–211, 2005. eprint: 0502465 (cond-mat).

[44] M. Salanne, C. Simon, P. Turq, and P. A. Madden, "Calculation of activities of ions in molten salts with potential application to the pyroprocessing of nuclear waste," *J. Phys. Chem. B*, vol. 112, pp. 1177–1183, 2008.

[45] B. Fultz, "Vibrational thermodynamics of materials," *Prog. Mater. Sci.*, vol. 55, no. 4, pp. 247–352, 2010.

[46] M. Forsblom and G. Grimvall, "Heat capacity of liquid Al: Molecular dynamics simulations," *Phys. Rev. B - Condens. Matter Mater. Phys.*, vol. 72, no. 13, pp. 1–4, 2005.

[47] L. Kaufman, "The lattice stability of the transition metals," in *Phase Stab. Met. Alloy.* P. S. Rudman, J. Stringer, and R. I. Jaffee, Eds., New York: McGraw-Hill, 1967, pp. 125–150.

[48] M. Hillert, "The compound energy formalism," *J. Alloys Compd.*, vol. 320, no. 2, pp. 161–176, 2001.

[49] M. Hillert, B. Jansson, B. Sundman, and J. Ågren, "A two-sublattice model for molten solutions with different tendency for ionization," *Metall. Trans. A*, vol. 16, no. 1, pp. 261–266, 1985.

[50] B. Sundman, "Modification of the two-sublattic model for liquids," *Calphad*, vol. 15, no. 2, pp. 109–119, 1991.

[51] A. D. Pelton, S. A. Degterov, G. Eriksson, C. Robelin, and Y. Dessureault, "The modified quasichemical model I – binary solutions," *Metall. Mater. Trans. B*, vol. 31B, no. August, pp. 651–659, 2000.

[52] A. D. Pelton and P. Chartrand, "The modified quasi-chemical model: Part II. Multicomponent solutions," *Metall. Mater. Trans. A*, vol. 32A, no. June, pp. 1355–1360, 2001.

[53] P. Chartrand and A. D. Pelton, "The modified quasi-chemical model: Part III. Two sublattices," *Metall. Mater. Trans. A*, vol. 32, no. 6, pp. 1397–1407, 2001.

[54] A. D. Pelton, P. Chartrand, and G. Eriksson, "The modified quasi-chemical model: Part IV. Two-sublattice quadruplet approximation," *Metall. Mater. Trans. A*, vol. 32, no. 6, pp. 1409–1416, 2001.

[55] C. W. Bale, E. Bélisle, P. Chartrand, S. A. Decterov, G. Eriksson, A. Gheribi, K. Hack, I. H. Jung, Y. B. Kang, J. Melançon, A. D. Pelton, S. Petersen, C. Robelin., J. Sangster, and M.-A. V. Ende, "FactSage thermochemical software and databases, 2015-2016," *Calphad*, vol. 54, pp. 35–53, 2016.

[56] W. A. Oates, H. Wenzl, and T. Mohri, "On putting more physics into CALPHAD solution models," *Calphad*, vol. 20, no. 1, pp. 37–45, 1996.

[57] W. J. M. van der Kemp, P. R. van der Linde, J. G. Blok, and H. A. J. Oonk, "The melting properties of the earth alkaline oxides; thermodynamic analysis of the binary system (1-X)MgO + XCaO," *Calphad*, vol. 17, no. 1, pp. 57–65, 1993.

[58] M. Chen, B. Hallstedt, and L. J. Gauckler, "CALPHAD modeling of the La_2O_3-Y_2O_3 system," *Calphad*, vol. 29, no. 2, pp. 103–113, 2005.

[59] T. Abe, C. Kocer, M. Ode, H. Murakami, Y. Yamabe-Mitarai, K. Hashimoto, and H. Onodera, "Thermodynamic re-assessment of the Al-Ir system," *Calphad*, vol. 32, no. 4, pp. 686–692, 2008.

[60] J. L. Meijering, "Calculation of the nickel-chromium-copper phase diagram from binary data," *Acta Metall.*, vol. 5, no. 5, pp. 257–264, 1957.

[61] O. Kubaschewski, C. B. Alcock, and P. Spencer, *Materials Thermochemistry*, 6th ed. Oxford: Pergamon Press Ltd, 1993, p. 363.

[62] O. Kubaschewski, "Experimental thermochemistry of alloys," *Thermochim. Acta*, vol. 129, pp. 11–27, 1988.

[63] P. K. Raychaudhuri and F. E. Stafford, "Alloy thermodynamics by mass spectrometry: A critical review," *Mater. Sci. Eng.*, vol. 20, no. C, pp. 1–18, 1975.

[64] K. C. Mills, K. Kinoshita, and P. Grieveson, "A thermodynamic study of liquid iron + nickel alloys using electromagnetic leviation," *J. Chem. Thermodyn.*, vol. 4, pp. 581–590, 1972.

[65] M. Faraday, "On electrochemical decomposition," *Phil. Trans. R. Soc. Lond.*, vol. 124, p. 77, 1834.

[66] B. A. Rose, G. J. Davis, and H. J. T. Ellingham, "Studies in the thermodynamics of metallurgical reduction processes by electrochemical methods," *Discuss. Faraday Soc.*, vol. 4, pp. 154–162, 1948.

[67] Y. K. Delimarskii and B. F. Markov, *Electrochemistry of Fused Salts (Translated)*, R. E. Wood, Ed. Washington D.C.: The Sigma Press, Publishers, 1961, p. 338.

[68] G. J. Janz, *Molten Salts Handbook*. New York: Academic Press, Inc., 1967, p. 588.

[69] K. Takahashi and Y. Miura, "Electrochemical behavior of glass melts," *J. Non. Cryst. Solids*, vol. 96, pp. 119–130, 1987.

[70] K. Kawamura and T. Yokokawa, "Linear sweep voltammetry of Pb^{2+}/Pb in oxide melts," *J. Electrochem. Soc.*, vol. 135, no. 6, pp. 1447–1451, 1988.

[71] A. Sasahira, K. Kawamura, M. Shimizu, N. Takada, M. Hongo, and T. Yokokawa, "Pb^{2+}/Pb redox equilibria in sodium borate, silicate, and aluminosilicate melts," *J. Electrochem. Soc.*, vol. 136, no. 7, pp. 1861–1864, 1989.

[72] G. R. Stafford and C. L. Hussey, "Electrodeposition of transition metal-aluminum alloys from chloroaluminate salts," in *Advances in Electrochemical Science and Engineering, Vol. 7*, R. C. Alkire and D. M. Kolb, Eds., Weinheim, Germany: Wiley-VCH Verlag GmbH, 2002, pp. 275–347.

[73] C. Rüssel, "Redox behavior and electrochemical behavior of glass melts," in *Properties of Glass-Forming Melts*, D. L. Pye, Ed., CRC Press, 2005, ch. 3, pp. 27–55.

[74] R. O. Colson, A. M. Floden, T. R. Haugen, K. M. Malum, M. Sawarynski, M. K. B. Nermoe, K. Jacobs, and D. Holder, "Activities of NiO, FeO, and O^{2-} in silicate melts," *Geochim. Cosmochim. Acta*, vol. 69, no. 12, pp. 3061–3073, 2005.

[75] P. Masset, R. J. Konings, R. Malmbeck, J. Serp, and J. P. Glatz, "Thermochemical properties of lanthanides (Ln = La, Nd) and actinides (An = U, Np, Pu, Am) in the molten LiCl-KCl eutectic," *J. Nucl. Mater.*, vol. 344, no. 1-3, pp. 173–179, 2005.

[76] S. Vandarkuzhali, N. Gogoi, S. Ghosh, B. Prabhakara Reddy, and K. Nagarajan, "Electrochemical behaviour of $LaCl_3$ at tungsten and aluminium cathodes in LiCl-KCl eutectic melt," *Electrochim. Acta*, vol. 59, pp. 245–255, 2012.

[77] J. N. Agar and F. P. Bowden, "The kinetics of electrode reactions. I and II," *Proc. R. Soc. London A, Math. Phys. Sci.*, vol. 169, no. 937, pp. 206–234, 1938.

[78] Polukarov and Gorbunova, "Some problems in the theory of electrodeposition of alloys," *Zhurnal Fiz. khimii*, vol. 30, no. 3, pp. 515–521, 1956.

[79] A. J. Bard and L. R. Faulkner, *Electrochemical Methods Fundamentals and Applications*, 2nd ed. New York: John Wiley & Sons, Inc., 2001, p. 833.

[80] R. C. Dorward, "Decomposition voltage for the electrolysis of alumina at low temperatures," *J. Appl. Electrochem.*, vol. 12, no. 5, pp. 545–548, 1982.

[81] J. W. Cuthbertson and J. Waddington, "A study of the cryolite-alumina cell with particular reference to decomposition voltage," *Trans. Faraday Soc.*, vol. 32, no. 1, pp. 745–59, 1936.

[82] T. Uda, T. H. Okabe, Y. Waseda, and K. Jacob, "Phase equilibria and thermodynamics of the system Dy-Mg-Cl at 1073 K," *J. Alloys Compd.*, vol. 284, no. 1-2, pp. 282–288, 1999.

[83] R. O. Colson, "In situ voltammetric observation of transitions above the liquidus in silicate melts," *Contrib. Mineral. Petr.*, vol. 159, no. 5, pp. 703–717, 2009.

[84] T. Hirai, Y. Miura, T. Yoshio, and K. Takahashi, "Measurements of decomposition voltage of Na_2O-SiO_2 system at elevated temperature by commutator technique," *Mem. Sch. Eng. Okayama Univ.*, vol. 2, no. 1, pp. 62–67, 1967.

[85] T. Berzins and P. Delahay, "Oscillographic polarographic waves for the reversible deposition of metals on solid electrodes," *J. Am. Chem. Soc.*, vol. 75, no. 3, pp. 555–559, 1953.

[86] N. White and F. Lawson, "Potential sweep voltammetry of metal deposition and dissolution: Part 1. Theoretical analysis," *J. Electroanal. Chem.*, vol. 25, pp. 409–19, 1970.

[87] D. J. Schiffrin, "Theroy of cyclic voltammetry for reversible electrodeposition of insoluble products," *J. Electroanal. Chem.*, vol. 201, pp. 199–203, 1986.

[88] C. J. P. Ball, "The history of magnesium," *J. Inst. Met.*, vol. 84, no. 11, p. 399, 1956.

Chapter 2

Hypothesis

Methods for Gibbs energy measurement were reviewed in the previous chapter, and the electrolytic cell method was identified as a promising, underutilized approach. For conditions where other techniques are prohibitive due to container or membrane requirements, the electrolytic cell method does not necessarily require such features. Such methods are well-established in dilute systems. However, the thermodynamics for numerous high temperature, concentrated melts are poorly informed, and previous investigations of concentrated electrolytes at low temperatures suggest that the electrolytic cell method is unreliable for such systems.

2.1 Scientific gap

As reviewed in §1.2.2, application of the electrolytic cell method for thermodynamic property measurement in concentrated electrolytes has previously been challenged by:

- inconsistent or unreliable ohmic drop compensation,
- electronic conductivity depolarization,
- activation polarization contributions, and
- signal interpretation and correlation with the states of reactants and products.

Modern digital instrumentation combined with the methods of electrochemical impedance spectroscopy (EIS) enables determination of ohmic drop with reasonable efficiency, accuracy and precision at open circuit and *polarized* conditions [1], [2]. Those reactions which influence the condition of the electrode-electrolyte interface (e.g. gas evolution [3]) require particular attention. Alternatively, for conditions where activation polarizations are negligible and the anode-cathode distance may be varied precisely, ohmic drop may be accurately related to variation in anode-cathode distance.

Depolarization effects due to electronic conductivity are anticipated to be negligible for those melts with sufficiently high electronic band gap and low solubility for the parent metal. Furthermore, electronic conductivity due to metal dissolution can be reduced by employing a reactive metal cathode host exhibiting negligible solubility in the electrolyte and minimizing the quantity of parent metal formed at the cathode by employing dynamic electrochemical techniques.

Although, metal deposition oftentimes occurs reversibly at $T > 500$ K [4] with negligible activation polarization, gas evolving electrodes have been shown to exhibit non-negligible activation polarization for $T > 1000$ K [5]–[8]. Kinetic theory suggests the reaction rates become increasingly fast as temperature is increased. However, electrochemical investigations have previously been restricted to $T < 2000$ K.

The interpretation of signals have been challenged by, perhaps, a lack of theoretical development for electrochemical processes occurring in concentrated electrolytes. In lieu of a rigorously physical treatment, oftentimes, workers rely on the method of extrapolation to zero current for obtaining decomposition voltage (e.g. [9]). Such interpretation lacks a physical basis for identifying the states of the reacting species, an essential component for thermodynamic interpretation. Furthermore, non-faradaic contributions (e.g. double layer capacitance or inductance [10]) are anticipated to further challenge interpretation of signals obtained by dynamic techniques, such as direct current (dc) cyclic voltammetry, in concentrated electrolytes. The work of Kawamura and coworkers [11], [12] involving studies of under-potential deposition on a *reactive* cathodes brings forth an interesting idea: *the phase change induced at the*

cathode interface during metal deposition enables one to correlate the reactant and product states and electrode potential for first formation of a liquid alloy. Perhaps, a similar situation exists for other reactions, e.g. gas evolution, allowing a similar correlation between decomposition voltage with reactant and product states in concentrated electrolytes.

2.2 Large amplitude alternating current voltammetry

Large amplitude alternating current voltammetry (ACV) is a voltammetric technique whose application has been restricted primarily to electrochemical studies in low-temperature, dilute electrolytes [13]–[16]. To quote Bond et al. [16], ACV "provides greater sensitivity with respect to resolving parameters derived for many classes of electrode process and hence leads to enhanced reliability in parameter reporting."

The approach has gained traction over the last twenty years thanks to increased accessibility to computing memory and power, a prerequisite for the relatively data-intensive acquisition and processing of signals. In practice, a sinusoidal signal is superimposed onto the usual linear dc ramp employed with dc swept or cyclic voltammetry, the total current response is recorded by a high frequency data acquisition module (DAQ), and the current signals are decomposed into their harmonic components by Fourier transform (FT) analysis (i.e FT total current signal from time domain to frequency domain, followed by extraction of harmonics by inverse FT back to time domain).

The resultant current response contains harmonic contributions arising from the nonlinear behavior of circuit elements present in the electrochemical circuit. Where some circuit elements, e.g. double layer capacitance, behave as essentially linear circuit elements, generating a non-faradaic current response primarily in dc and first harmonic responses, the faradaic (charge-transfer) reaction is inherently nonlinear [13]–[16]. Therefore, analysis of the second and higher harmonics is merited by their

increased sensitivity to the nonlinear, faradaic reaction. Furthermore, the higher harmonics can be interpreted with the aid of numerical modeling for acquisition of kinetic parameters from a single measurement, a significant advantage over dc techniques.

In regards to signal interpretation, the non-linear character of the faradaic reaction is theoretically and experimentally observed to result in a peak-splitting feature observed across higher harmonics at the half-wave potential in dilute electrolytes [13]–[16]. This effectively reduces signal interpretation to a spectroscopic-like procedure with non-faradaic contributions eliminated, a significant improvement over other voltammetric techniques (e.g. dc cyclic and square-wave voltammetry). However, application of ACV to reactions at high temperature in concentrated electrolytes has been severely limited. Sokhanvaran et al. reported ACV measurements for liquid copper (Cu) deposition on a graphite electrode from a sulfide electrolyte composed of 45 mol% Cu_2S-55 mol% BaS at $T = 1378$ K [17]. Interestingly, they observed a peak splitting feature across the harmonics of the current response coinciding with the half-wave potential for Cu depostion. This result suggests the applicability of ACV methods for high temperature study of faradaic reactions.

2.3 Hypothesis

Careful electrochemistry in high temperature, concentrated systems allows for a connection between electrochemical signals and equilibrium properties of the electrolyte and products of decomposition. Furthermore, only ohmic polarization contributes significantly to the decomposition voltage measurement for concentrated ionic melts decomposed at high temperature.

2.4 Verification of hypothesis

For conditions in which the hypothesis is valid, the electrolytic cell method is a relevant means for direct measurement of Gibbs energy of reaction $\Delta_r G$ with appropriate

correction for ohmic drop, i.e. equation Eq. 1.2 reduces to

$$U = V - IR_{cell}$$

and the relation between the measured cell voltage and $\Delta_r G$ described by 1.1 becomes

$$\Delta_r G = -nF\left(V - IR_{cell}\right)$$

Furthermore, if the ACV response is sensitive to the state of the product phase formed, then analysis of the shapes of the current harmonics provide qualitative (quantitative with electrochemical modeling) information about the states of the products and reactants during faradaic reactions. In such conditions, as the electrode potential is dynamically varied (e.g during metal deposition), the ACV response is foreseen to precisely indicate a change in the product state (e.g from solid to liquid metal). At the potential coinciding with a two-phase equilibrium product, the product state is defined by the two-phase equilibrium. If such electrode's potential is measured with respect to a thermodynamically well-defined reference energy level, then such potential difference may be related to a reaction Gibbs energy informing the product chemical potential for the two-phase equilibrium.

In summary, as applied to systems for which the hypothesis is valid, the electrolytic cell method *is* a reliable method for direct measurement of Gibbs energy.

2.5 Limitations of hypothesis

The hypothesis does not extend to liquids that do not conduct electricity solely by the migration of ions (e.g. liquid metals, highly covalent or molecular liquids and liquid semiconductors). Though not necessarily a liquid, but a fluid, gases in low ionization conditions are also not expected to be relevant. At low temperatures, systems exhibiting sluggish kinetics (non-negligible activation overpotential) are not compatible with the hypothesis. Inspired by ideas of Pauling [18], materials that are stable at high temperatures with a large electronegativity difference, large electronic

band gap, and high ionic mobility *are* expected to be of interest. However, the hypothesis is not expected to apply to melts containing ions exhibiting multivalency where electron migration can occur, e.g. due to "electron hopping" [19].

Conditions for which the measured electrode potential is controlled by the product species is considered in more detail in Appendix A and involves considerations of concentration and transport of the electrochemically active species in the various phases involved. For pseudo-unary[1] component electrolytes, charge neutrality constraints suggest that the concentration requirement is satisfied at all practical electric fields [20]. As described in the previous chapter, previous decomposition voltage studies in multi-component electrolytes have been restricted to investigations of a dilute solute in a supporting electrolyte solvent. In such situations, the concentration of solute in the electrolyte varies significantly during reduction or oxidation at the electrode interface.

The focus of the present work is restricted to the decomposition of concentrated electrolytes in the absence or significant lack of a supporting electrolyte on a reactive cathode and inert anode. For metal deposition occurring on an initially pristine, reactive cathode, the maximum concentration of the depositing species in the initial cathode phase is limited by its solubility, and a new phase forms as its concentration exceeds this maximum. Under such conditions, the results from Appendix A, suggest that the requirement for concentrated melts is satisfied for $C_{solute} \gg 0.1$ M when the solubility of the reduced species in the reactive electrode is on the order of 10 mol%.

2.6 Materials selection

For testing the hypothesis of the present work, material compounds exhibiting ionic behavior in the liquid state at ultra-high temperature (UHT, defined herein as $T > 2000\ K$) are required. In this work, the search was restricted to binary compounds of the form MX_z where M is an electropositive metal, X is an electronegative nonmetal

[1]The terminology "pseudo" is herein adopted to describe the isopleth representation of binary and higher order component systems. For example, the pseudo-unary melt of MO(l) is, in fact, a binary mixture of M-O; the pseudo-binary liquid MO-NO is also a ternary mixture of M-N-O.

and z denotes stoichiometry. Higher order compounds, e.g. hydroxides or carbonates, are expected to decompose preventing their study at UHT. Therefore, the electrolytic decomposition of the compound MX_z to M and X is the intended reaction of study. For example, if X occurs as a diatomic gas molecule and M a liquid, then the overall decomposition reaction envisioned is:

$$MX_z(l) \rightarrow M(l) + \frac{z}{2}X_2(g)$$

Facilitating the candidate material selection, the following criteria, to be described in more detail hereafter, were employed:

1. considerations of ionic bonding between M and X,
2. predictions of electronic band gap for solid MX_z at 0 K,
3. temperature range of thermal stability of MX_z at $101,325$ Pa,
4. behavior of M and X as pure elements, and
5. existing body of knowledge for MX_z, viz. thermodynamic data.

Compounds with a Pauling electronegativity difference $\Delta\chi > 1.6$ and electronic band gap $E_g > 1$ eV were considered. Though somewhat primitive, these criteria yield the well-known salts, e.g. chlorides and fluorides, while filtering covalent compounds, e.g. silica or CH_4. Compounds of the halogens, oxides, sulfides and nitrides (i.e. $X = F, Cl, Br, I, O, S, N$) satisfy these two criteria, as presented in Figure 2-1.

In regards to thermal stability, nitrides sublime or decompose before melting at ambient pressures [4]. Many sulfides, iodides, bromides, chlorides and the alkali metal oxides exhibit only a limited temperature range of stability $T < 1500$ K due primarily to their high vapor pressures [4]. The fluorides, although relatively high melting and low vapor pressure, present an extreme experimental challenge due to their reactivity [4].

Remaining are those oxides of the alkaline earth, lanthanide, actinide, transition (Group III to VII) and post-transition (Ga, Al) metals. Many of these oxide

compounds melt at UHT. Their parent metals exhibit good metallic behavior. The alkaline earth metals exhibit a very high vapor pressure at the melting point of their pure oxides.

For those remaining, the oxides of Al, Hf, Zr, Sc, Y, the lanthanides, and the actinides maximize $\Delta\chi$ and E_g. These oxides were found to exhibit similar $\Delta\chi$ and E_g to fluoride and chloride compounds, quintessential molten salts, as shown in Figure 2-1. Although confirmation of the ionic nature for these oxide materials does not exist to the author's knowledge, previous workers (e.g. [21]) have hypothesized their electrolytic behavior utilizing electric conductivity measurements. For some of these compounds, a significant change in the conductivity has been observed upon melting, e.g. yttria (Y_2O_3) [22], a characteristic feature for ionic melts [23]. More recently, structural measurements for some of these liquids confirm a significant rearrangement of atoms and bonds upon melting, which further supports their ionic nature [24], [25].

Of the remaining oxide compounds, alumina (Al_2O_3), Y_2O_3 and lanthana (La_2O_3) are the most thoroughly investigated [22], [28]–[31]. Exhibiting an UHT melting point ($T_{fus} = 2327\ K$) [32], low vapor pressure ($p^o_{Al_2O_3}(T_{fus}) \approx 0.2$ Pa [33]), high conductivity ($\sigma(T_{fus}) \approx 2.7$ S cm^{-1} [28]), and relatively large band gap ($E_g = 5.85$ eV [27]), Al_2O_3 is identified as an exemplary pseudo-unary candidate. Additionally, the CALPHAD community predicts [29], [34] the pseudo-binary system Y_2O_3-La_2O_3 exhibits ideal mixing behavior upon fusion. If Y_2O_3-La_2O_3 is indeed ideal and ionic upon melting, then Y_2O_3-La_2O_3 would represent one of the relatively "simplest" of multi-component systems for testing the hypothesis of the present work. Therefore, pure Al_2O_3 and the binary system Y_2O_3-La_2O_3 were identified as test material systems.

2.7 Framework for testing hypothesis

First, given the limited application of ACV to high temperature electrolytes, the utility of ACV for interpretation of signals and states of reactants and products will be tested in a low temperature, well-known, concentrated melt for which a true reference electrode can be utilized. The chloride salt, equimolar sodium chloride-potassium

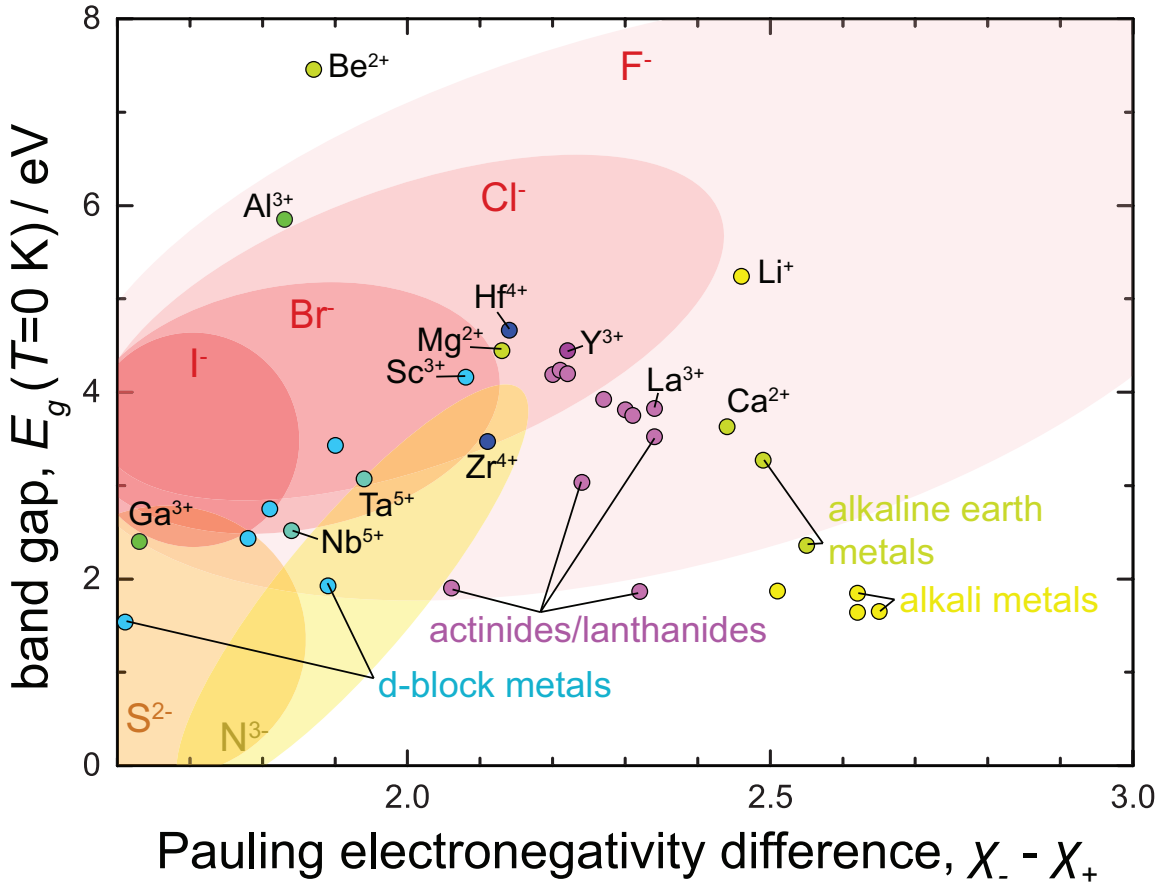

Figure 2-1: E_g ($>$ 1 eV) vs. $\Delta\chi$ [26] for binary oxide compounds (represented as circles). The band gaps are those computed by density functional theory at T = 0 K for the most stable solid compound, retrieved from [27]. The areas in which fluoride, chloride, bromide, iodide, sulfide and nitride binary compounds predominate are shown for comparison.

chloride (NaCl-KCl), is identified as such an electrolyte system satisfying all but the temperature stability requirement from §2.6. The existence of a true reference electrode (i.e. Ag/AgCl) permits ready comparison of half-wave potential measurements with those calculated from thermodynamic data. The half-cell reactions for co-deposition of Na-K on inert and reactive electrodes and chlorine evolution on an inert electrode will be investigated in NaCl-KCl. Described in §3, this effort will serve as a basis for ACV signal interpretation in the UHT concentrated melts.

Second, a significant technical challenge exists for practically contacting electrodes to UHT melts, since no electrochemical methods have been reported for such conditions to the author's knowledge. A novel technique for UHT electrochemistry

is engineered and described in §4. Additionally, difficulties are anticipated for the interpretation of decomposition voltage measurements at UHT in refractory[2] oxides because a true reference electrode does not exist. A novel approach for decomposition voltage measurement providing a rigorous connection to thermodynamic properties of the reactants and products is described in §5.

Finally, the UHT electrolytes selected in §2.6 will be electrolytically decomposed to test their electrolytic nature and their decomposition voltage will be measured using the methods described in §4 and §5. The results will compared with available thermodynamic data to test the hypothesis. First, as presented in §6, the decomposition voltage method will be applied to relatively well-known, pseudo-unary molten Al_2O_3 system. Then, the method will be extended to the pseudo-binary electrolyte Y_2O_3 and La_2O_3, as described in §7.

2.8 Summary

The electrolytic cell method was identified as a promising approach for Gibbs energy measurements in concentrated ionic melts at high temperature. However, challenges related signal interpretation and correlation with the states of reactants and products have challenged application of the method for thermodynamic property measurement in such systems.

It is herein hypothesized that:

- Careful electrochemistry in high temperature, concentrated systems allows for a connection between electrochemical signals and equilibrium properties of the electrolyte and products of decomposition.
- Only ohmic polarization contributes significantly to the decomposition voltage measurement for concentrated ionic melts decomposed at UHT.

The melts of pure Al_2O_3 and the binary system Y_2O_3-La_2O_3 were selected for testing the hypothesis. Their decomposition voltage will be measured and compared

[2]Here "refractory" refers to oxide compounds more stable and higher melting point than SiO_2

with available thermodynamic data. First, the electrolytic decomposition of NaCl-KCl will be investigated using ACV to test the utility of this method for probing high temperature faradaic reactions.

References

[1] A. J. Bard and L. R. Faulkner, *Electrochemical Methods Fundamentals and Applications*, 2nd ed. New York: John Wiley & Sons, Inc., 2001, p. 833.

[2] M. E. Orazem and B. Tribollet, *Electrochemical Impedance Spectroscopy*. Hoboken: John Wiley & Sons, Inc., 2008, p. 538.

[3] H. Vogt and J. Thonstad, "The diversity and causes of current-potential behaviour at gas-evolving electrodes," *Electrochim. Acta*, vol. 250, pp. 393–398, 2017.

[4] G. J. Janz, *Molten Salts Handbook*. New York: Academic Press, Inc., 1967, p. 588.

[5] G. J. Janz, F. Colom, and F. Saegusa, "Oxygen overpotential in molten carbonates," *J. Electrochem. Soc.*, vol. 107, no. 7, p. 581, 1960.

[6] G. J. Janz and F. Saegusa, "Anodic polarization curves in molten carbonate electrolysis," *J. Electrochem. Soc.*, vol. 108, no. 7, pp. 663–9, 1961.

[7] H. Flood and T. Forland, "Some investigations on the oxygen-overpotential in molten salts," *Discuss. Faraday Soc.*, vol. 1, pp. 302–307, 1947.

[8] N. Jarrett, "United States extractive metallurgy-The 80's and beyond," *Metall. Trans. B*, vol. 18, no. 6, pp. 289–313, 1987.

[9] T. Uda, T. H. Okabe, Y. Waseda, and K. Jacob, "Phase equilibria and thermodynamics of the system Dy-Mg-Cl at 1073 K," *J. Alloys Compd.*, vol. 284, no. 1-2, pp. 282–288, 1999.

[10] A. Kisza, "The origin of Inductance in high energy electrode reactions," *Pol. J. Chem.*, vol. 70, no. 7, pp. 922–938, 1996.

[11] K. Kawamura and T. Yokokawa, "Linear sweep voltammetry of Pb^{2+}/Pb in oxide melts," *J. Electrochem. Soc.*, vol. 135, no. 6, pp. 1447–1451, 1988.

[12] A. Sasahira, K. Kawamura, M. Shimizu, N. Takada, M. Hongo, and T. Yokokawa, "Pb^{2+}/Pb redox equilibria in sodium borate, silicate, and aluminosilicate melts," *J. Electrochem. Soc.*, vol. 136, no. 7, pp. 1861–1864, 1989.

[13] D. J. Gavaghan and A. M. Bond, "A complete numerical simulation of the techniques of alternating current linear sweep and cyclic voltammetry: analysis of a reversible process by conventional and fast Fourier transform methods," *J. Electroanal. Chem.*, vol. 480, no. 1-2, pp. 133–149, 2000.

[14] S. O. Engblom, J. C. Myland, and K. B. Oldham, "Must ac voltammetry employ small signals?" *J. Electroanal. Chem.*, vol. 480, no. 1-2, pp. 120–132, 2000.

[15] A. M. Bond, N. W. Duffy, S. X. Guo, J. Zhang, and D. Elton, "Changing the look of voltammetry," *Anal. Chem.*, vol. 77, 186A–195A, 2005.

[16] A. M. Bond, D. Elton, S. X. Guo, G. F. Kennedy, E. Mashkina, A. N. Simonov, and J. Zhang, "An integrated instrumental and theoretical approach to quantitative electrode kinetic studies based on large amplitude Fourier transformed a.c. voltammetry: A mini review," *Electrochem. Commun.*, vol. 57, pp. 78–83, 2015.

[17] S. Sokhanvaran, S.-K. Lee, G. Lambotte, and A. Allanore, "Electrochemistry of molten sulfides: copper extraction from BaS-Cu_2S," *J. Electrochem. Soc.*, vol. 163, no. 3, pp. D115–D120, 2016.

[18] L. Pauling, "The nature of the chemical bond. IV. The energy of single bonds and the relative electronegativity of atoms," *J. Am. Chem. Soc.*, vol. 54, no. 9, pp. 3570–3582, 1932.

[19] M. Barati and K. S. Coley, "Electrical and electronic conductivity of CaO-SiO_2-FeO_x slags at various oxygen potentials: Part II. Mechanism and a model of electronic conduction," *Metall. Mater. Trans. B*, vol. 37, no. February, pp. 51–60, 2006.

[20] Y. K. Delimarskii and B. F. Markov, *Electrochemistry of Fused Salts (Translated)*, R. E. Wood, Ed. Washington D.C.: The Sigma Press, Publishers, 1961, p. 338.

[21] J. D. Mackenzie, "Oxide melts," in *Advances in Inorganic Chemistry and Radiochemistry, Vol. 4*, H. J. Emeleus and A. G. Sharpe, Eds., New York: Academic Press Inc., 1962, pp. 293–318.

[22] E. E. Shpil'rain, D. N. Kagan, L. S. Barkhatov, and L. I. Zhmakin, "Electrical conductivity of yttrium and scandium oxides," *Rev. Int. Hautes Temper. Refract.*, vol. 16, no. 3, pp. 233–236, 1979.

[23] J. O. Bockris and A. K. N. Reddy, *Modern Electrochemistry, vol. 1*, 2nd ed. New York: Plenum Press, 1998, pp. 601–753.

[24] L. B. Skinner, C. J. Benmore, J. K. R. Weber, J. Du, J. Neuefeind, S. K. Tumber, and J. B. Parise, "Low cation coordination in oxide melts," *Phys. Rev. Lett.*, vol. 112, p. 157 801, 2014.

[25] L. B. Skinner, C. J. Benmore, J. K. R. Weber, M. A. Williamson, A. Tamalonis, A. Hebden, T. Wiencek, O. L. G. Alderman, M. Guthrie, L. Leibowitz, and J. B. Parise, "Molten uranium dioxide structure and dynamics," *Science*, vol. 346, no. 6212, pp. 984–987, 2014. eprint: `arXiv:1107.5325v1`.

[26] J. E. Huheey, E. A. Keiter, and R. L. Keiter, *Inorganic Chemistry: Principles of Strucutre and Reactivity*, 4th ed. New York: Harper Collins, 1993.

[27] A. Jain, S. P. Ong, G. Hautier, W. Chen, S. Richards, William Davidson Dacek, S. Cholia, D. Gunter, D. Skinner, G. Ceder, and K. A. Persson, "The Materials Project: A materials genome approach to accelerating materials innovation," *APL Mater.*, vol. 1, no. 1, p. 011 002, 2013.

[28] B. R. Nakanishi and A. Allanore, "Electrochemical study of a pendant molten alumina droplet and its application for thermodynamic property measurements of Al-Ir," *J. Electrochem. Soc.*, vol. 164, no. 13, E460, 2017.

[29] M. Chen, B. Hallstedt, and L. J. Gauckler, "CALPHAD modeling of the La_2O_3-Y_2O_3 system," *Calphad*, vol. 29, no. 2, pp. 103–113, 2005.

[30] V. Swamy, H. J. Seifert, and F. Aldinger, "Thermodynamic properties of Y_2O_3 phases and the yttrium-oxygen phase diagram," *J. Alloys Compd.*, vol. 269, no. 1-2, pp. 201–207, 1998.

[31] A. N. Grundy, B. Hallstedt, and L. J. Gauckler, "Thermodynamic assessment of the lanthanum-oxygen system," *J. Phase Equilibria*, vol. 22, no. 2, pp. 105–113, 2001.

[32] R. E. Bedford, G. Bonnier, H. Maas, and F. Pavese, "Recommended values of temperature on the International Temperature Scale of 1990 for a selected set of secondary reference points," *Metrologia*, vol. 33, pp. 133–154, 1996.

[33] C. W. Bale, E. Bélisle, P. Chartrand, S. A. Decterov, G. Eriksson, A. Gheribi, K. Hack, I. H. Jung, Y. B. Kang, J. Melançon, A. D. Pelton, S. Petersen, C. Robelin., J. Sangster, and M.-A. V. Ende, "FactSage thermochemical software and databases, 2015-2016," *Calphad*, vol. 54, pp. 35–53, 2016.

[34] M. Zinkevich, "Thermodynamics of rare earth sesquioxides," *Prog. Mater. Sci.*, vol. 52, no. 4, pp. 597–647, 2007.

Chapter 3

Electrochemical study of molten NaCl-KCl

As described in the previous chapter, ACV is known to provide increased sensitivity to faradaic reactions due to their nonlinear behavior [1], [2]. However, experimental and theoretical application of the technique to high temperature, concentrated electrolytes remains severely limited [3], [4]. Therefore, decomposition voltage measurements were performed using ACV in a well-studied electrolyte, equimolar NaCl-KCl, to verify that the electrochemical rules for ACV translate to these systems, and supplement the basis for signal interpretation in other high temperature, concentrated melts (e.g. refractory oxides).

3.1 Background

Equimolar NaCl-KCl is a quintessential molten salt. The electrolytic decomposition of NaCl-KCl has previously been investigated on various substrates [5]–[7]. For example, the evolution of chlorine gas on a graphite anode from NaCl-KCl is the well-established and thoroughly studied anodic half-cell reaction in this system [6], [7]. Furthermore, Na and K are known to underpotential co-deposit from NaCl-KCl [5].

3.2 Experimental

3.2.1 Materials & equipment

Equimolar NaCl-KCl (both purity >99.5%, Wako Pure Chemical Industries) was placed in a thoroughly cleaned (ground, polished, rinsed and sonicated) graphite crucible. All salts were melted previously for impurity removal via HCl(g) bubbling. A nichrome-wound resistance furnace was used with the digital controller set to $T = 973$ K. A type-K thermocouple placed between the heating elements and stainless steel vessel in the furnace hot zone provided temperature sensing (accuracy is estimated to be no better than ± 5 K). The salt and crucible charge was placed in a stainless steel vessel that was sealed outside the furnace hot zone by a rubber O-ring and water-cooled stainless steel cap with ports for electrodes and gas lines. Prior to heating, the sealed stainless tube was purged with vacuum and argon (Ar) gas three times.

3.2.2 Electrochemical methods & operation

A three-electrode cell was employed consisting of a high purity graphite rod (⌀6 mm) for the CE and a Ag/AgCl RE [8]. Rods of graphite (same dimension as the CE), molybdenum (⌀2 mm) and gold (⌀0.5 mm) were employed for the WE. Electrical contacts to the WE and CE in the furnace hot-zone were made by threaded molybdenum rods (⌀2 mm) sheathed in alumina. The RE compartment was contained in a ground, closed-one-end alumina tube permitting electrical contact between the electrolyte and RE compartment. All measured potentials are referred to this RE unless specified otherwise. A potentiostat (Model 1287, Solartron) and impedance analyzer (Model 1260, Solartron) were employed for voltammetry and EIS measurements. All potentials were corrected for ohmic drop using the uncompensated resistance obtained via fitting of EIS impedance spectra obtained at open circuit conditions.

For ACV measurements, a sine wave created by a digital signal generator (UltraLite-mk3 Hybrid, MOTU) was passed through an amplifier circuit to the external input of the potentiostat. The total current response was sampled via the potentiostat's

external output at 30 kHz by data acquisition (DAQ, DT9837B, Data Translation). The generated sine wave signal's amplitude, frequency and purity were determined by direct measurement of the post-amplified signal by the DAQ. Forward Fourier transform (FT) and inverse FT signal processing for analysis of the dc, 1st and higher harmonics of the total current signals were performed using Scilab code, similar to that employed by Nakanishi et al. [4] (available in Appendix C).

The current-interrupt method [9]–[12] was employed to determine the Cl^-/Cl_2 standard electrode potential ($E^o_{Cl^-/Cl_2}$) on the graphite WE versus the RE. Galvanostatic electrolysis was performed using a galvanostat (model HZ-7000, Hokuto Denko Co.). The current and WE potential (E) were recorded by the DAQ at 30 kHz. Each current step (anodic current densities $j = 300, 375, 450$ mA cm^{-2}) was 10 s in duration, after which the current was shut off (interrupted) at time $t = 0$ by the potentiostat and the open circuit potential (OCP) was monitored for 10 s. Due to practical limitations for the galvanostat's electronic controller circuit, trace currents were detected following current interrupt, so OCP immediately following current interruption was estimated by extrapolation of E from the time at which $|j| < 1$ mA cm^{-2} to $t = 0$.

3.3 Results & discussion

3.3.1 Investigation of chlorine evolution on a graphite anode

A typical ACV voltammogram for the dc component ($I_{0\omega}$), first ($I_{1\omega}$), second ($I_{2\omega}$) and third ($I_{3\omega}$) harmonics of the current response for a graphite WE are shown in Figure 3-1. As E is swept from OCP to +1.3 V vs. Ag/AgCl, $I_{0\omega}$ increases sharply at approximately +1.1 V vs. Ag/AgCl accompanying the chlorine evolution reaction:

$$Cl^- = e^- + \frac{1}{2}Cl_2(g). \tag{3.1}$$

At $E = E^*_A$, a characteristic peak splitting feature across $I_{1\omega}$ and the higher harmonics was observed. To aid in the identification of the physical significance for E^*_A in regards

to 3.1, $E^o_{Cl^-/Cl_2}$ for Reaction 3.1 occurring on the identical graphite electrode was measured by the current interrupt method.

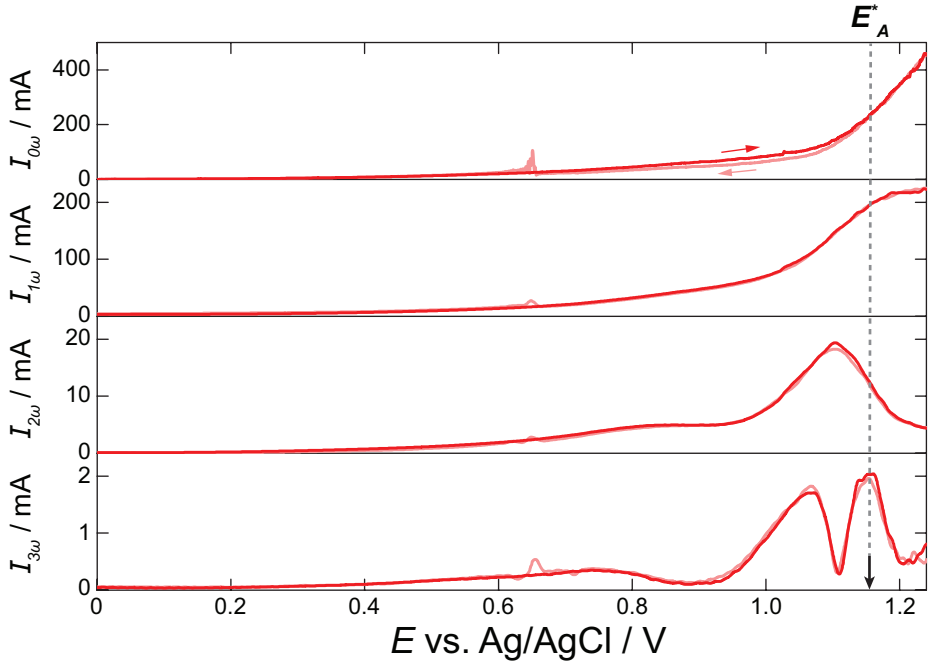

Figure 3-1: From top to bottom panel, typical dc component, first, second and third harmonic current responses obtained during ACV measurements on graphite in 100 mM $AlCl_3$ (NaCl-KCl); $A_G = 0.67$ cm^2, scan limits -0.43 (OCP) to $+1.30$ V vs. Ag/AgCl, $E_{ac} = 74$ mV, $f = 20$ Hz, $\nu = 28$ mV s^{-1}, $T = 973$ K. E^*_A is described in text.

Results for E^*_A were compared with $E^o_{Cl^-/Cl_2}$ as presented in Figure 3-2. The results for E^*_A were observed to be systematically greater than $E^o_{Cl^-/Cl_2}$. This difference between E^*_A and $E^o_{Cl^-/Cl_2}$ may be related by:

$$\eta = E^*_A - E^o_{Cl^-/Cl_2}$$

where η represents an overpotential contribution attributed to the influence of current flow at the graphite electrode interface during ACV measurements. On average, η was determined to be 14.6 ± 3 mV, and the average dc current density was approximately $j_{0\omega}(E = E^*_A) = 325 \pm 30$ mA cm^{-2}.

Nevertheless, given the close agreement for E^*_A and $E^o_{Cl^-/Cl_2}$ along with the fixed energy level of the Ag/AgCl RE, the following observations are deduced for the present

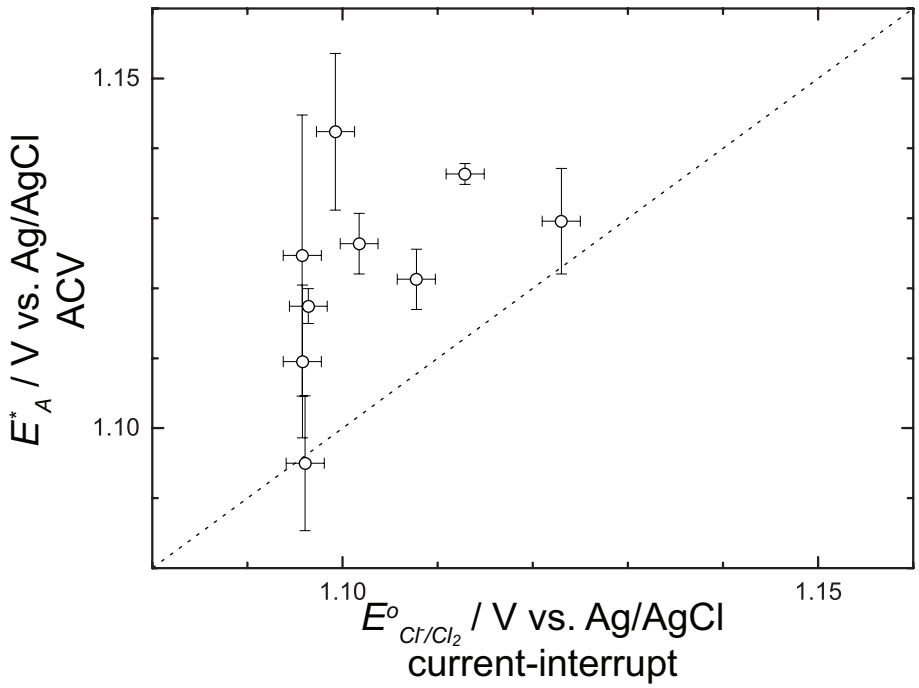

Figure 3-2: Comparison of results for E_A^* and $E^o_{Cl^-/Cl_2}$ obtained by ACV (cf. Figure 3-1) and current-interrupt methods, resp.

conditions:

1. The feature of the ACV response occurring near E_A^*, cf. Figure 3-1, indicates the chlorine evolution (Reaction 3.1) .

2. The electrochemical potentials (states) of Cl^- and Cl_2(g) are identical for E_A^* and $E^o_{Cl^-/Cl_2}$.

3. The difference between these two quantities, namely η, is an overpotential contribution arising from irreversibilities (i.e. activation overpotential) at the WE due to current flow during ACV measurement.

3.3.2 Investigation of reactions on Mo & Au cathodes

The reactions occurring on Mo and Au cathodes during the decomposition of NaCl-KCl were also investigated by ACV. Typical ACV voltammograms showing the dc through third harmonics of the current response obtained on Mo and Au are shown in Figures 3-3 and 3-4, resp.

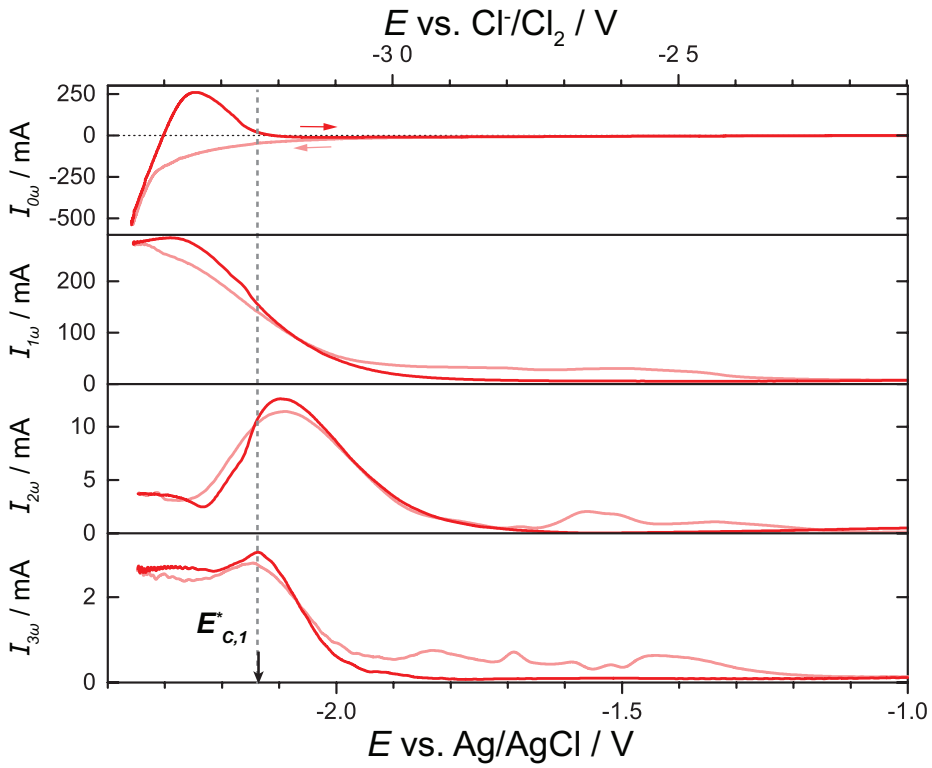

Figure 3-3: From top to bottom panel, typical dc component, first, second and third harmonic current responses obtained during ACV measurements on Mo in NaCl-KCl; $A_G = 0.75$ cm^2, scan limits -0.59 (OCP) to -2.50 V vs. Ag/AgCl, $E_{ac} = 79$ mV, $f = 20$ Hz, $\nu = 37$ mV s^{-1}, $T = 973$ K. The quantity E^*_A is defined in text.

Na and K are known [5] to co-deposit from the equimolar NaCl-KCl electrolyte. Mo is only slightly soluble in liquid Na-K, and no intermetallic compounds are known to form at the conditions investigated [13], [14]. Therefore, Mo represents an "inert" cathode for investigation of the electrodeposition of Na-K. Therefore, it is no surprise that a single reaction occurs at $E^*_{C,1}$ marked in Figure 3-3 accompanying the co-deposition of Na-K liquid. $E^*_{C,1}$ was measured to be -3.233 V vs. Cl^-/Cl_2. For comparison, the standard potentials for pure Na and K liquid formation are $E^o_{Na^+/Na(l)} = -3.367$ and $E^o_{K^+/K(l)} = -3.609$ V vs. Cl^-/Cl_2 for the equimolar electrolyte (calculated using FactSage [15]). Assuming facile kinetics and negligible variation in Na^+ and K^+ concentration, the difference between the standard potentials and $E^*_{C,1}$ are related to the activity of M = Na or K (standard state pure liquid M at T and

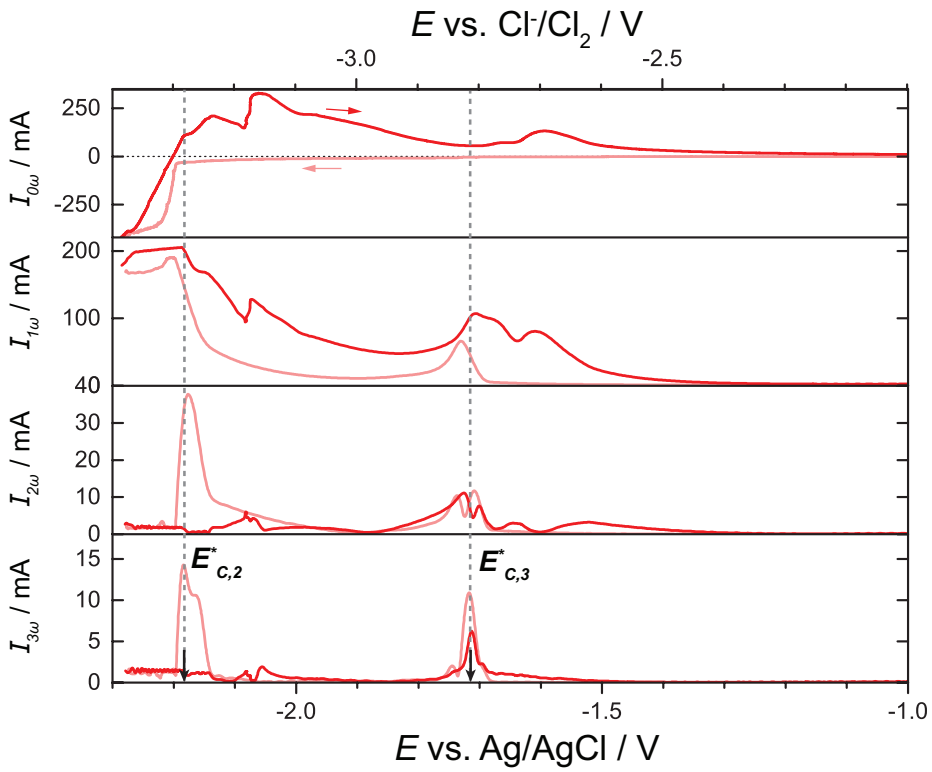

Figure 3-4: From top to bottom panel, typical dc component, first, second and third harmonic current responses obtained during ACV measurements on Au in NaCl-KCl; $A_G = 0.16$ cm^2, scan limits -0.74 (OCP) to -2.50 V vs. Ag/AgCl, $E_{ac} = 79$ mV, $f = 20$ Hz, $\nu = 37$ mV s^{-1}, $T = 973$ K. The quantity E_A^* is defined in text.

$p = 101,325$ Pa) by

$$E^*_{C,1} - E^o_{M^+/M(l)} = -\frac{RT}{F}\ln(a_{\underline{M}}) \tag{3.2}$$

Using Eq. 3.2, the activities are determined as $a_{\underline{Na}} = 0.2$ and $a_{\underline{K}} = 0.01$, which is highly unlikely for the binary Na-K alloy at $T = 973$ K. Perhaps, the presence of Mo has depressed the activities of Na and K or the preceding assumptions require further assessment. Nevertheless, harmonic features in the ACV response are observed to occur coinciding with Na-K liquid alloy formation at a Mo cathode, cf. Figure 3-3.

On the other hand, Au has a liquid solubility at $T = 973$ K of approximately 40 and 50 mol% for the Au-Na [16] and Au-K [17] binary subsystems, resp. Furthermore, the binary intermetallic compounds KAu_5, $NaAu_5$ and $NaAu_2$ are known to be stable at these temperatures. KAu_5 and $NaAu_2$ are quite stable, melting congruently at 1313 and 1275 K, resp. The high temperature reaction for $NaAu_5$ is unknown. Therefore,

Au represents a "reactive" cathode. Two reactions are observed during the negative-going scan at $E^*_{C,2} = -3.265$ and $E^*_{C,3} = -2.811$ V vs. Cl^-/Cl_2 as shown in Figure 3-4. The reaction coinciding with $E^*_{C,2}$ is likely due to liquid alloy formation. If this were the case, $a_{\underline{Na}} = 0.3$ and $a_{\underline{K}} = 0.02$, which is plausible for the ternary liquid alloy containing circa 45 mol% Au. Given the preceding description for the binary intermetallic compounds, a very stable intermetallic compound is hypothesized to form at $E^*_{C,3}$. The possibility that this feature is due to the presence of an impurity ion seems highly unlikely given that the ACV signals observed at $E^*_{C,3}$ for a gold Au cathode were repeatable across experiments employing fresh electrolytes and not observed on other cathode materials (e.g. Mo) utilized within the same experiment. However, further analysis of this reaction was not pursued further.

3.4 Summary

Faradaic reactions and their corresponding half-wave potential were precisely detected with ACV in NaCl-KCl. This the first of such effort in high temperature molten halogen salts to the author's knowledge.

On the anode, chlorine gas evolution exhibits a characteristic peak-splitting feature across the second and higher harmonics. Results for Cl^-/Cl_2 potential determined by ACV were compared with those obtained by the current-interrupt method. Discrepancies for values obtained by ACV and current-interrupt methods were observed, which were attributed to irreversibilities accompanying Cl_2 evolution for the conditions investigated.

On the cathode, peak-splitting features were observed for reactions involving metal deposition and alloy formation accompanying the decomposition of NaCl-KCl on Mo and Au cathodes. The potentials corresponding to those signal features were compared qualitatively and quantitatively where possible with existing phase diagrams and thermodynamic data to support signal interpretation.

Thus, the results confirm the interpretation of ACV signals, i.e. peak-splitting features, found in dilute systems translate to the highly-concentrated salt NaCl-KCl

at $T = 973$ K for gas evolution and metal co-deposition. Modeling efforts are foreseen to improve the interpretation of signals and their correlation with half-wave potentials. Nevertheless, the utility of ACV for the detection and interpretation of faradaic reactions within the present scope has been shown.

References

[1] A. M. Bond, N. W. Duffy, S. X. Guo, J. Zhang, and D. Elton, "Changing the look of voltammetry," *Anal. Chem.*, vol. 77, 186A–195A, 2005.

[2] S. O. Engblom, J. C. Myland, and K. B. Oldham, "Must ac voltammetry employ small signals?" *J. Electroanal. Chem.*, vol. 480, no. 1-2, pp. 120–132, 2000.

[3] S. Sokhanvaran, S.-K. Lee, G. Lambotte, and A. Allanore, "Electrochemistry of molten sulfides: copper extraction from BaS-Cu_2S," *J. Electrochem. Soc.*, vol. 163, no. 3, pp. D115–D120, 2016.

[4] B. R. Nakanishi and A. Allanore, "Electrochemical study of a pendant molten alumina droplet and its application for thermodynamic property measurements of Al-Ir," *J. Electrochem. Soc.*, vol. 164, no. 13, E460, 2017.

[5] G. J. Janz, *Molten Salts Handbook*. New York: Academic Press, Inc., 1967, p. 588.

[6] S. V. Evdokimov, "Kinetics of chlorine evolution on dimensionally stable anodes at high currents: Extending the concept of a self-accelerating electrode process," *Russ. J. Electrochem.*, vol. 36, no. 3, pp. 236–239, 2000.

[7] B. V. Tilak, "Kinetics of chlorine evolution–A comparative study," *J. Electrochem. Soc.*, vol. 126, no. 8, pp. 1343–1348, 1979.

[8] R. Littlewood, "A reference electrode for electrochemical studies in fused alkali chlorides at high temperatures.," *Electrochim. Acta*, vol. 3, no. January 1960, pp. 270–278, 1961.

[9] K. Yasuda, T. Nohira, K. Amezawa, Y. H. Ogata, and Y. Ito, "Mechanism of direct electrolytic reduction of solid SiO_2 to Si in molten $CaCl_2$," *J. Electrochem. Soc.*, vol. 152, no. 4, pp. D69–D74, 2005.

[10] J. Newman, "Ohmic potential measured by interrupter techniques," *J. Electrochem. Soc.*, vol. 117, no. 4, pp. 507–508, 1970.

[11] D. Kiuchi, H. Matsushima, Y. Fukunaka, and K. Kuribayashi, "Ohmic resistance measurement of bubble froth layer in water electrolysis under microgravity," *J. Electrochem. Soc.*, vol. 153, no. 8, E138, 2006.

[12] W. Oelbner, F. Berthold, and U. Guth, "The iR drop–Well-known but often underestimated in electrochemical polarization measurements and corrosion testing," *Mater. Corros.*, vol. 57, no. 6, pp. 455–466, 2006.

[13] P. R. Subramanian, "Mo-Na (molybdenum-sodium)," in *Binary Alloy Phase Diagrams*, T. B. Massalski, H. Okamoto, P. R. Subramanian, and L. Kacprzak, Eds., 2nd ed., vol. 3, ASM International, 1990, pp. 2631–2633.

[14] ——, "K-Mo (potassium-molybdenum)," in *Binary Alloy Phase Diagrams*, T. B. Massalski, H. Okamoto, P. R. Subramanian, and L. Kacprzak, Eds., 2nd ed., vol. 3, ASM International, 1990, pp. 2375–2376.

[15] C. W. Bale, E. Bélisle, P. Chartrand, S. A. Decterov, G. Eriksson, A. Gheribi, K. Hack, I. H. Jung, Y. B. Kang, J. Melançon, A. D. Pelton, S. Petersen, C. Robelin., J. Sangster, and M.-A. V. Ende, "FactSage thermochemical software and databases, 2015-2016," *Calphad*, vol. 54, pp. 35–53, 2016.

[16] A. D. Pelton, "Au-Na (gold-sodium)," in *Binary Alloy Phase Diagrams*, T. B. Massalski, H. Okamoto, P. R. Subramanian, and L. Kacprzak, Eds., 2nd ed., vol. 1, ASM International, 1990, pp. 397–399.

[17] ——, "Au-K (gold-potassium)," in *Binary Alloy Phase Diagrams*, T. B. Massalski, H. Okamoto, P. R. Subramanian, and L. Kacprzak, Eds., 2nd ed., vol. 1, ASM International, 1990, pp. 383–385.

Chapter 4

UHT electrochemistry by pendant droplet technique

A suitable experimental facility permitting electrode contact to Al_2O_3, Y_2O_3 and La_2O_3 melts at UHT is required for testing the hypothesis of this work. Experiments involving the liquid state, particularly at UHT, have been challenged by technical difficulties oftentimes arising from the selection of a suitable container. Therefore, a coupling of electrochemical methods with *containerless* processing is identified as the desirable path for this endeavor.

Unfortunately, no UHT containerless, electrochemical techniques have been reported. Therefore, a survey is made of the relevant containerless approaches for UHT study of melts. The thermal imaging furnace (TIF), providing a thermally stable hot zone and atmosphere flexibility, was identified as the optimal approach and modified to allow contact between a molten pendant droplet and electrodes for electrochemical measurements [1]. Herein, the apparatus and its operation are described.

4.1 Review of containerless methods

A summary of the relevant containerless methods is provided in Table 4.1. Dynamic heating methods (e.g laser flash [2] or ohmic-pulse heating methods [3]) have been omitted due to their transient nature (experiment duration $\ll 1$ s).

Table 4.1: Summary of containerless methods considered

Method	Heat Source	Sample Size (g)	Atmosphere	Challenges	Ref.
electromagnetic levitation	induction	1-100	flexible	electrode contact, electromagnetic interference.	[4]
electrostatic levitation	laser	$<10^{-1}$	vacuum	sample size, electrode contact, atmosphere flexibility.	[5]
aerodynamic levitation	laser	$<10^{-1}$	no vacuum	sample size, electrode contact.	[6], [7]
acoustic levitation	laser	<10	no vacuum	sample size, electrode contact.	[8]
cold crucible	induction	>1	flexible	T-gradients, EM interference.	[9], [10]
thermal imaging furnace (TIF)	Xe lamp or laser	10	flexible	T-gradients.	[1], [11]

Today, levitation methods are preferred for thermophysical property investigation; however, the foreseeable challenge of contacting electrodes to a small molten droplet without interfering with its levitation precludes the union of levitation and electrochemical methods. The cold crucible technique has been utilized for investigating melt behavior at UHT [10], but electromagnetic coupling and signal interference from the inductive heat source poses a severe challenge for most electrochemical techniques.

An alternative containerless approach involves a pendant droplet heated in an thermal imaging (or arc imaging) furnace (TIF) [12], which was extensively developed for and is nearly exclusively associated today with the floating zone crystal growth method [13]–[15]. Historically, TIF's provided for the first time "essentially unlimited" temperature ranges for melting essentially any material in "practically any atmosphere" [15]. Despite their focus on improving crystal growth at the time, Field and Wagner suggested that "the technique can be utilized for other high temperature experiments of importance to material research..." [15]. Diamond and Dragoo were among the first to take advantage of these opportunities to directly observe the solubility of gases (Ar, O_2, H_2, H_2O, N_2, and He) and their effects on vaporization behavior of molten pendant droplets of Al_2O_3 [16]. Soon after the advent of lasers,

they were utilized as a heat source in TIF's for the superior heating efficiency [17], [18]. For example, Nelson et al. revisited the solubility of gaseous species in molten Al_2O_3 and their effects on solidification [19]. Later, Krishnan et al. measured the refractive index of molten Al_2O_3 in a laser-heated pendant droplet [20]. Only recently Katsumata et al. reported electrical measurements in a TIF to measure the thermopower of molten TiO_2 using two iridium (Ir) electrodes [11]. No investigations utilizing electrochemical measurements with a pendant droplet have been reported prior to this work.

4.2 Apparatus design & operation

A TIF equipped with four Xe lamps (12 kW total) and ellipsoidal mirrors, schematically shown in Figure 4-1, was modified for electrochemical measurements [1]. Details regarding sample rod and electrochemical probe preparation are described in Appendix C. The sample rod, suspended from the upper rotating shaft, was positioned with its bottom end at the focal point of the mirrors, hereafter called "hot zone." The electrode probe was introduced through the bottom port. The vertical positions of the sample and probe were controlled independently by stepper motors with sub-millimeter precision. The probe and sample assembly were isolated from ambient atmosphere with a quartz tube (Technical Glass Products Inc.) sealed with Viton O-rings and vacuum-gas purged. A digital camera (EOS Rebel T5i DSLR, Canon Inc.) with a telescopic lens provided continuous monitoring and video recording of the sample and electrodes in the hot zone.

For a typical experiment, the Xe lamps were powered on, and the lamp power was gradually increased until the bottom of the rotating sample was visually molten. A stable pendant droplet formed, suspended by a balance between the melt surface tension and gravity. Rotation was halted, and the electrodes were raised upwards while monitoring the OCP. Visual observation and OCP stabilization confirmed electrode insertion into the droplet.

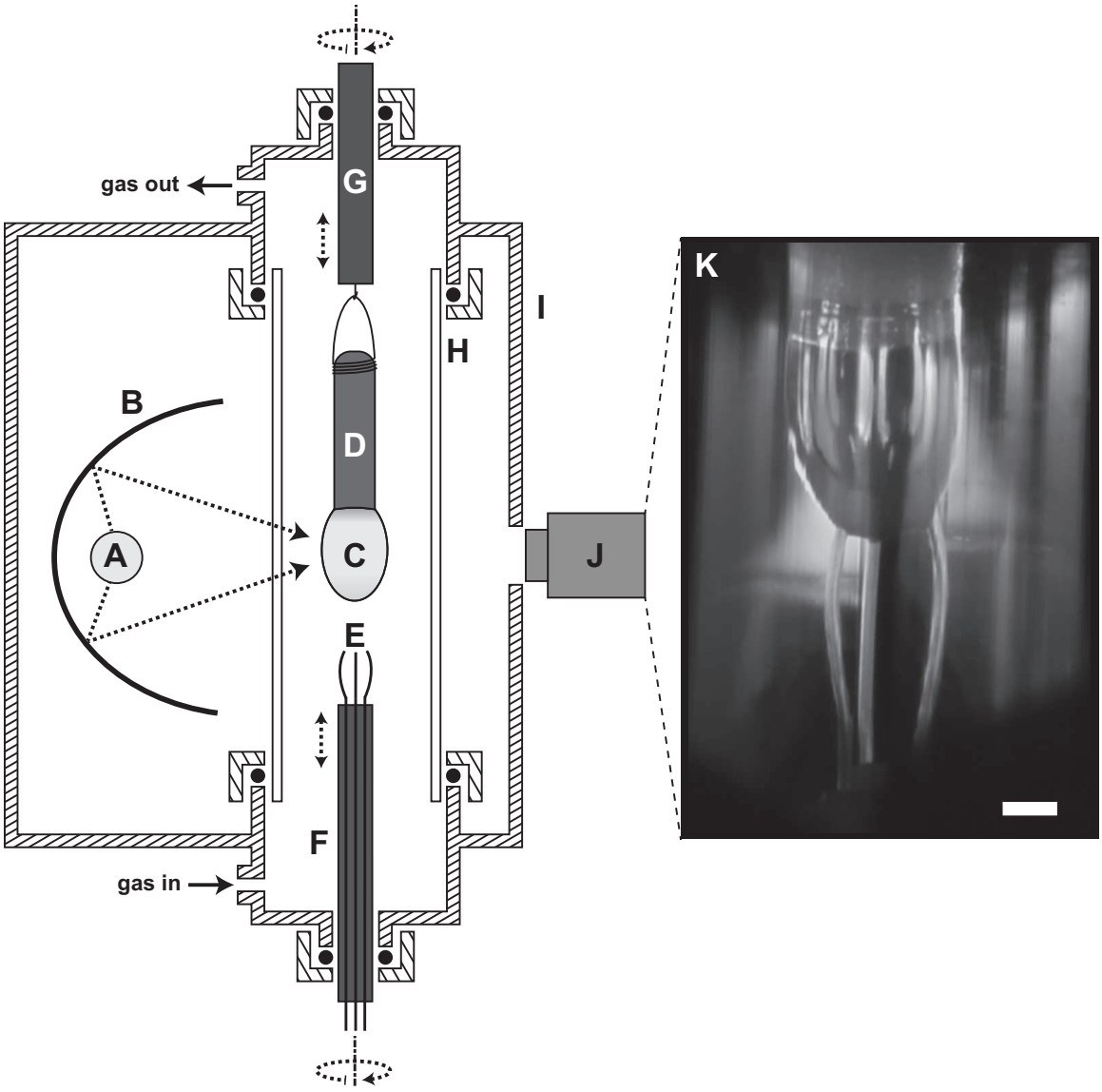

Figure 4-1: Schematic of the experimental setup (not to scale): (A) Xe lamp and (B) ellipsoidal mirror (one of four pairs shown), (C) molten pendant droplet (0.1 cm^3 volume, typically) in the hot zone, (D) solid sample rod suspended by wire loop, (E) electrodes, (F) electrode leads and lower shaft, (G) upper shaft, (H) quartz tube, (I) furnace shell, (J) camera, and (K) photograph of iridium (Ir) electrodes inserted into a molten Al_2O_3 droplet (scale bar 2 mm). Additional details are provided in Nakanishi et al. [1] available in Appendix C.

4.3 Apparatus performance

Typically, stable electrode insertion into a molten pendant droplet was achieved in five minutes or less after lamps were initially powered. Four Xe lamps produced a uniform

(< 10 K radial variation) and time-stable temperature distribution in the hot zone (approximately 1 cm^3 volume), permitting experimental duration for a single molten droplet and electrodes to exceed 1 h, if necessary. As mentioned in the preceding sections, the TIF was extensively developed for floating zone crystal growth, which oftentimes requires days of continuous, stable conditions for crystal growth.

Large temperature gradients on the order of 200 K/mm are present at steady state near the hot zone [21], [22]. This feature adds flexibility for sample rod and electrode probe design.

Furthermore, it is emphasized that a camera provides continuous visual access to the droplet and electrodes during the experiment. This feature represents a significant advantage over other approaches where visual access is extremely limited, e.g. resistance or induction furnaces.

Given the hot zone is formed by focused light transmission through a transparent quartz tube, the heating efficiency is dramatically reduced as vapor species condense on the cooler quartz tube when materials exhibiting high vapor pressure are used. Therefore, volatile materials are not compatible with this approach. However, high pressure operation may be used mitigate this issue.

As described in the preceding section, the stability of the pendant droplet and electrode contact is due to the balance in forces of surface tension of the melt and gravity. Therefore, melts exhibiting particularly low surface tension may prove challenging to investigate using the current approach.

4.4 Summary

A novel experimental approach was described for containerless, electrochemical measurements at temperatures above 2000 K. A thermal imaging furnace was modified enabling three or more electrodes to electrically contact a molten pendant droplet for electrochemical measurements, e.g. decomposition voltage measurements. The key features of the approach are:

1. long-duration, mechanically stable electrode-melt contact

2. thermally stable and uniform hot zone (approx. 1 cm^3 volume) for electrode-melt contact

3. continuous visual observation of electrodes and droplet

4. atmosphere flexibility (reducing, oxidizing, inert, vacuum)

References

[1] B. R. Nakanishi and A. Allanore, "Electrochemical study of a pendant molten alumina droplet and its application for thermodynamic property measurements of Al-Ir," *J. Electrochem. Soc.*, vol. 164, no. 13, E460, 2017.

[2] S. V. Ushakov and A. Navrotsky, "Experimental approaches to the thermodynamics of ceramics above 1500°C," *J. Am. Ceram. Soc.*, vol. 95, no. 5, pp. 1463–1482, 2012.

[3] R. Gallob, H. Jager, and G. Pottlacher, "A submicrosecond pulse heating system for the investigation of thermophysical properties of metals at high temperatures," *Int. J. Thermophys.*, vol. 7, no. 1, pp. 139–147, 1986.

[4] E. C. Okress, D. M. Wroughton, G. Comenetz, P. H. Brace, and J. C. R. Kelly, "Electromagnetic levitation of solid and molten metals," *J. Appl. Phys.*, vol. 23, no. 5, pp. 545–552, 1952.

[5] P. F. Paradis, T. Ishikawa, G. W. Lee, D. Holland-Moritz, J. Brillo, W. K. Rhim, and J. T. Okada, "Materials properties measurements and particle beam interactions studies using electrostatic levitation," *Mater. Sci. Eng. R*, vol. 76, no. 1, pp. 1–53, 2014.

[6] J. K. R. Weber, A. Tamalonis, C. J. Benmore, O. L. G. Alderman, S. Sendelbach, A. Hebden, and M. A. Williamson, "Aerodynamic levitator for in situ X-ray structure measurements on high temperature and molten nuclear fuel materials," *Rev. Sci. Instrum.*, vol. 87, no. 7, p. 073 902, 2016.

[7] D. Langstaff, M. Gunn, G. N. Greaves, A. Marsing, and F. Kargl, "Aerodynamic levitator furnace for measuring thermophysical properties of refractory liquids," *Rev. Sci. Instrum.*, vol. 84, no. 12, p. 124 901, 2013.

[8] E. G. Lierke, "Acoustic levitation–A comprehensive survey of principles and applications," *Acustica*, vol. 82, no. 2, pp. 220–237, 1996.

[9] Y. B. Petrov, A. V. Shul'kov, and I. V. Shurygina, "Induction melting of refractory oxide materials in cold crucibles," *Ukr. Sci. Inst. Refract.*, no. 10, pp. 536–41, 1981.

[10] Y. B. Petrov, Y. P. Udalov, J. Subrt, S. Bakardjieva, P. Sazavsky, M. Kiselova, P. Selucky, P. Bezdicka, C. Jorneau, and P. Piluso, "Behavior of melts in the UO_2-SiO_2 system in the liquid-liquid phase separation region," *Glas. Phys. Chem.*, vol. 35, no. 2, pp. 199–204, 2009.

[11] T. Katsumata, T. Shiina, M. Shibasaki, and T. Matsuo, "Electrical measurements on molten TiO_2 using a floating zone furnace," *J. Cryst. Growth*, vol. 239, pp. 1791–1796, 2002.

[12] M. R. Null and W. W. Lozier, "Carbon arc image furnaces," *Rev. Sci. Instrum.*, vol. 29, no. 2, pp. 163–170, 1958.

[13] R. E. De La Rue and F. A. Halden, "Arc-image furnace for growth of single crystals," *Rev. Sci. Instrum.*, vol. 31, no. 1, pp. 35–38, 1960.

[14] R. P. Poplawsky and J. E. Thomas, "Floating zone crystals using an arc image furnace," *Rev. Sci. Instrum.*, vol. 31, no. 12, pp. 1303–1308, 1960.

[15] W. G. Field and R. W. Wagner, "Thermal imaging for single crystal growth and its application to ruby," *J. Cryst. Growth*, vol. 4, pp. 799–803, 1968.

[16] J. J. Diamond and A. L. Dragoo, "Studies of molten alumina in the arc-image furnace," *Rev. Hautes Temp. Refract.*, vol. 3, no. 3, pp. 273–279, 1966.

[17] K. Eickhoff and K. Gürs, "Tiegelfreies zonenschmelzen von rubinkristallen durch aufheizen der schmelzzone mittels laser," *J. Cryst. Growth*, vol. 6, pp. 21–25, 1969.

[18] D. B. Gasson and B. Cockayne, "Oxide crystal growth using gas lasers," *J. Mater. Sci.*, vol. 5, no. 2, pp. 100–104, 1970.

[19] L. S. Nelson, S. R. Skaggs, and N. L. Richardson, "Spherodization of refractory oxides with a carbon dioxide laser," *J. Am. Ceram. Soc.*, vol. 11, no. February, pp. 1968–1969, 1970.

[20] S. Krishnan, J. K. R. Weber, R. A. Schiffman, P. C. Nordine, and R. A. Reed, "Refractive index of liquid aluminum oxide at 0.6328 μm," *J. Am. Ceram. Soc.*, vol. 74, no. 4, pp. 881–883, 1991.

[21] J. Haggerty and W. P. Menashi, "Production of oxide fibers by a floating zone fiber drawing technique," NASA Lewis Research Center, Cleveland, OH, Tech. Rep., 1972, p. 82.

[22] K. Kitazawa, K. Nagashima, T. Mizutani, K. Fueki, and T. Mukaibo, "A new thermal imaging system utilizing a Xe arc lamp and ellipsoidal mirror for crystallization of refractory oxides," *J. Cryst. Growth*, vol. 39, pp. 211–215, 1977.

Chapter 5

Decomposition voltage measurement approach

The proposed strategy for testing this work's hypothesis involves relating decomposition voltage measurements to tabulated thermodynamic quantities. In molten NaCl-KCl, a true RE was used, which provided a fixed, well-defined energy level for comparison of half-wave potentials obtained via ACV to tabulated thermodynamic quantities during study of the electrochemical reactions occurring on a WE. No such RE is available for refractory oxide melts. Thus, an alternative approach is needed.

A procedure for measuring decomposition voltage and relating measurements to well-defined thermodynamic quantities in refractory oxide melts at ultra-high temperature (UHT) is herein reported. The method for decomposition voltage measurements and conditions of validity for the proposed approach are discussed.

5.1 Problem description & considerations

Consider the overall cell reaction for oxide MO(l) decomposing to metal M alloyed with a liquid on the cathode $\underline{M}(l)$ and oxygen gas $O_2(g)$:

$$MO(l) \rightarrow \underline{M}(l) + \frac{1}{2}O_2(g) \tag{5.1}$$

The half-cell reaction occurring on an inert anode involves oxidation of oxide ions O^{2-} to $O_2(g)$

$$O^{2-} = \frac{1}{2}O_2(g) + 2e^- \tag{5.2}$$

and at the cathode involves reduction of metal cations M^{2+} to $\underline{M}(l)$:

$$M^{2+} + 2e^- = \underline{M}(l) \tag{5.3}$$

For the conditions hypothesized in §2, the chief problem lies with identifying the states of the species involved at the anode and cathode during measurement of the decomposition voltage (U) as Reaction 5.1 proceeds. The detection, electrode potential measurement, and features of the cathode and anode half-cell reactions are presented in the following sections.

5.1.1 Anode

It is posited here that ACV permits detection of Reaction 5.2 occurring on the anode in a method described as follows. During ACV measurements, the anode inner electric potential is controlled with respect to a pseudo-RE, an additional wire in contact with the melt. At the RE surface, the chemical potentials of the electrochemically active species controlling the RE inner electric potential[1] does not necessarily remain fixed during cell polarization. However, a pseudo-RE enables investigation of the reactions occurring on the anode during ACV measurements in a traceable manner, independent of the reactions occurring on the cathode, by harmonic analysis as demonstrated in a molten chloride electrolyte in §3 involving chlorine gas evolution on an inert anode. As applied to a molten oxide electrolyte, the evolution of oxygen gas via Reaction 5.2 on an inert anode is herein envisioned, and assumed to exhibit a characteristic peak-splitting in the ACV response. Under such conditions, the anode adopts the potential E_A^* relative to the pseudo-RE as identified by a peak-splitting

[1]The "inner electric potential" or "Galvani potential" (ϕ, SI unit V) is an unmeasurable quantity for a given material phase. However, the difference in inner electric potentials between two phases is measurable when those phases have similar compositions, e.g. two copper wires [1], [2].

feature in the ACV harmonics (e.g. see Figure 3-1 for chlorine evolution in molten NaCl-KCl or Figure 6-4 for oxygen evolution in molten Al_2O_3). The cell exhibits voltage $U(E_A^*)$ and total current $I(E_A^*)$. E_A^*, $U(E_A^*)$, and $I(E_A^*)$ represent respectively the minimum anode potential, minimum cell voltage and threshold current to drive reaction 5.2 on the anode.

During reaction 5.2, the anode inner electric potential ϕ_A is given by the Nernst equation:

$$\phi_A = \frac{1}{4F}\mu_{O_2}^A - \frac{1}{2F}\mu_{O^{2-}}^A \tag{5.4}$$

where $\mu_{O_2}^A$ and $\mu_{O^{2-}}^A$ are the chemical potentials of $O_2(g)$ and O^{2-} at the anode, resp. Variation of $\mu_{O^{2-}}$ as a function of O^{2-} activity $a_{O^{2-}}$ (standard state is O^{2-} at its equilibrium molar concentration in the electrolyte at temperature T in the presence of pure $O_2(g)$ at 101,325 Pa) is given by

$$\mu_{O^{2-}} = \mu_{O^{2-}}^o + RT\ln(a_{O^{2-}})$$

The standard state for O^{2-} (and $O_2(g)$) defined here is somewhat arbitrary in the present context. More pertinent to the present discussion is $\mu_{O^{2-}}$ (and μ_{O_2}) variation during polarization. While the possibility of $a_{O^{2-}}$ variation cannot be eliminated entirely, assuming negligible variation from $a_{O^{2-}} = 1$ for the relevant conditions is justified if:

1. The anode is inert, or oxidation of the anode negligibly influences $a_{O^{2-}}$.

2. The electrolyte is constrained by charge neutrality and molten MO exhibits a limited distribution of states for oxide ions[2].

[2]Melts involving silica and other network-forming oxides are well-known to involve a complex distribution of polyionic chains, where the distribution of bonding states for oxide ions, e.g. free, single-bonded and double-bounded in molten silicates [3], varies significantly in energy. In such melts, the average $a_{O^{2-}}$ can vary depending on the relative proportions of oxide ions occupying the various available states [4]–[6]. Furthermore it has been suggested by Gmitter et al. [7]–[9] that oxygen evolution occurs due to the discharge of free oxide ions in molten silicates. If valid, the activity of the free, relatively high-energy oxide ions at the electrode surface controls the electrode potential and, furthermore, varies during current flow due to mass transport limitations.

The analysis herein is valid for concentrated ionic oxide melts in which the distribution of states for oxide ions is limited (i.e. an availability of few states, e.g. only "free" oxide ions, or a narrow

For normal total pressures ($p \approx 101,325$ Pa), fugacity and partial pressure may be assumed equivalent for $O_2(g)$, i.e. O_2 is an ideal gas, and the variation of μ_{O_2} as a function of oxygen partial pressure p_{O_2} (standard state is chosen for convenience as pure $O_2(g)$ at $101,325$ Pa and temperature T) is given by

$$\mu_{O_2} = \mu^o_{O_2} + RT \ln(p_{O_2})$$

The variation of μ_{O_2} from $\mu^o_{O_2}$ during oxygen gas evolution may be neglected assuming:

1. The total internal pressure of gas bubbles at the anode surface are formed at $101,325$ Pa, which is valid considering mechanical equilibrium between the external pressure from the furnace gas and negligible surface tension effects.

2. The partial pressure of species other than $O_2(g)$ may be neglected.

For the situation herein considered, the inner electric potential ϕ_A relates $\mu^A_{O^{2-}}$ (equivalent to the bulk chemical potential of O^{2-}) to $\mu^o_{O_2}$. Furthermore, negligible variations of $\mu^A_{O_2}$ and $\mu^A_{O^{2-}}$ with anodic current during oxygen gas formation on the anode imply that ϕ_A remains fixed at $\phi_A = \phi^*_A$, permitting use of the anode potential as a reference energy level for decomposition voltage measurement. Therefore, an electrode under such conditions may be utilized as a "polarized dynamic" oxygen electrode[3] providing a fixed inner electric potential of reference.

5.1.2 Cathode

A similar situation to that described in the previous section for the anode is posited for investigation of reactions occurring on the cathode described as follows. First,

distribution of bonding energies). In more complicated systems, the analysis will require accounting for variation in $a_{O^{2-}}$ at the anode during polarization (i.e. concentration overpotential). For now, we tentatively neglect this feature as a simplifying assumption, which can be at least partially justified by structural considerations for the pure, non-networking-forming oxides employed in this study. For example, molten alumina has been shown to be composed primarily of highly connected AlO_4^{-5} and AlO_5^{-7} anions with $> 80\%$ of oxygen atoms linked to three or more polyhedra [10]. Contrasted with molten silicates [11], the assumption in molten alumina and similar melts appears justified.

[3]Compare with the "dynamic hydrogen reference electrode" [12]–[14]. Cho et al. [15] first distinguished the dynamic RE types as "polarized" vs. "unpolarized" (e.g. Afonichkin et al. [16]).

ACV is assumed to provide a means of uniquely and precisely detecting of the first formation of a new phase (liquid alloy in this case via Reaction 5.3) at the cathode by harmonic peak-splitting analysis similar to that described in §3 for liquid alloy formation occurring on a reactive cathode. In this case, E_C^*, $U(E_C^*)$, and $I(E_C^*)$ are defined to represent respectively the minimum cathode potential, minimum cell voltage and threshold current to drive reaction 5.3 on the cathode.

During reaction 5.3, the cathode inner electric potential ϕ_C is given by:

$$\phi_C = \frac{1}{2F}\left(\mu^C_{M^{2+}} - \mu^C_{\underline{M}}\right) \tag{5.5}$$

where $\mu^C_{\underline{M}}$ and $\mu^C_{M^{2+}}$ are the chemical potentials of $\underline{M}$ and M^{2+} at the cathode.

The variation in $\mu_{\underline{M}}$ as a function of $\underline{M}$ activity $a_{\underline{M}}$ (standard state pure liquid M at T, $p = 101,325$ Pa) is given by:

$$\mu_{\underline{M}} = \mu^o_M + RT\ln(a_{\underline{M}})$$

Given the preceding discussion, E_C^* corresponds to the the first formation of the new phase at the reactive cathode (liquid alloy) and $a_{\underline{M}}$ (and $\mu^C_{\underline{M}}$) is fixed by the equilibrium between the two phases present (i.e. alloy liquid and solid solution).

Variation of $\mu_{M^{2+}}$ as a function of M^{2+} activity $a_{M^{2+}}$ (standard state defined as M^{2+} at its equilibrium molar concentration in the electrolyte at temperature T, $p = 101,325$ Pa) is given by:

$$\mu_{M^{2+}} = \mu^o_{M^{2+}} + RT\ln(a_{M^{2+}})$$

The variation of $a_{M^{2+}}$ is anticipated to be negligible ($a_{M^{2+}} \approx 1$) assuming:

1. The concentration of $\underline{\text{M}}$ in product liquid alloy is much less than the relative to concentration of M^{2+} in oxide melt. This is considered more rigorously in Appendix A.

For the situation herein discussed, the inner electric potential ϕ_C relates the $\mu^C_{M^{2+}}$ (equivalent to the bulk chemical potential of M^{2+}) and $\mu^C_{\underline{M}}$ (chemical potential of

M at the two-phase equilibrium between liquid and solid solution alloys with the reactive cathode). Therefore, ϕ_C relates the difference in chemical potential between these states according to Eq. 5.5, provided ϕ_C is measured with respect to a fixed, well-defined reference energy level, i.e. a polarized dynamic oxygen electrode. A method permitting such measurement is discussed in the following two sections.

5.2 Approach

A measurement of ϕ_C corresponding with half-cell Reaction 5.3 with respect to ϕ_A corresponding to half-cell Reaction 5.2 represents a cell potential difference (U), and is related to the chemical potentials of the reacting species by:

$$U = \phi_A - \phi_C = \frac{1}{4F}\mu^o_{O_2} + \frac{1}{2F}\mu_{\underline{M}} - \frac{1}{2F}\left(\mu^C_{M^{2+}} + \mu^A_{O^{2-}}\right) \tag{5.6}$$

For the conditions envisioned, $\mu^C_{M^{2+}}$ and $\mu^A_{O^{2-}}$ exhibit negligible deviations from the bulk, and therefore may be related to the chemical potential of MO in the bulk (μ_{MO}) according to:

$$\mu_{MO} = \mu^C_{M^{2+}} + \mu^A_{O^{2-}}$$

Therefore, U is equivalent to the decomposition voltage for Reaction 5.1 (hereafter denoted as U^o) and Eq. 5.6 reduces to

$$U^o = \frac{1}{4F}\mu^o_{O_2} + \frac{1}{2F}\mu_{\underline{M}} - \frac{1}{2F}\mu_{MO} \tag{5.7}$$

Where $\mu^o_{O_2}$, $\mu_{\underline{M}}$ and μ_{MO} were defined previously. In the particular case that MO is a pure melt, then $\mu_{MO} = \mu^o_{MO}$, the standard chemical or molar Gibbs energy of pure liquid MO.

The approach for U^o measurement described here involves utilizing a polarized dynamic oxygen electrode as a fixed reference energy level. Practically, the anode is envisioned as a suitable polarized dynamic oxygen electrode given that ϕ_A is anticipated to remain fixed, as described in §5.1.1. Though utilizing an additional pair

of electrodes to create a polarized dynamic oxygen electrode is possible, the anode is preferred in this case to simplify cell design and reduce the number of failure modes, an advantage for high temperature experiments. Therefore, a criterion is needed which will ensure that the anode has achieved an inner electric potential of ϕ_A during $U(E_C^*)$ measurement. In such circumstances, $U(E_C^*)$ and U^o are equivalent.

5.2.1 A criterion for decomposition voltage measurement

The cell geometry, i.e. the cathode and anode electroactive areas (A_C and A_A, resp.) exposed to the electrolyte, are anticipated to influence the relative values of $U(E_A^*)$ and $U(E_C^*)$, assuming U is a monotonic function I. This phenomenon can be rationalized by electrochemical engineering principles. If the current densities $j(E_C^*)$ and $j(E_A^*)$ occurring at the cathode and anode, resp., are known, then a cell geometry satisfying the condition

$$\frac{A_C}{A_A} > \frac{j(E_C^*)}{j(E_A^*)} \tag{5.8}$$

is anticipated to yield $U(E_C^*) > U(E_A^*)$.

Figure 5-1 shows a schematic illustration of the corresponding electrochemical situation for $U > U(E_C^*) > U(E_A^*)$. Under such conditions and in light of the preceding discussion for Reaction 5.2, the minimum current density required to drive $O_2(g)$ evolution via Reaction 5.2 is achieved, and the anode inner electric potential attains the value ϕ_A. As described previously, during measurement of $U(E_C^*)$, the cathode attained inner electric potential ϕ_C coincides with Reaction 5.3. Therefore, for such situations $U(E_C^*) = U^o = \phi_A - \phi_C$, where U^o, as defined in the previous section, is the minimum decomposition potential difference to drive the overall cell Reaction 5.1

5.2.2 Procedure

In practice, the proposed approach for decomposition voltage measurement involves the following steps:

1. Determine the minimum cell voltage ($V(E_A^*)$) and current ($I(E_A^*)$) to drive oxygen evolution on the anode by means ACV harmonic analysis (verification

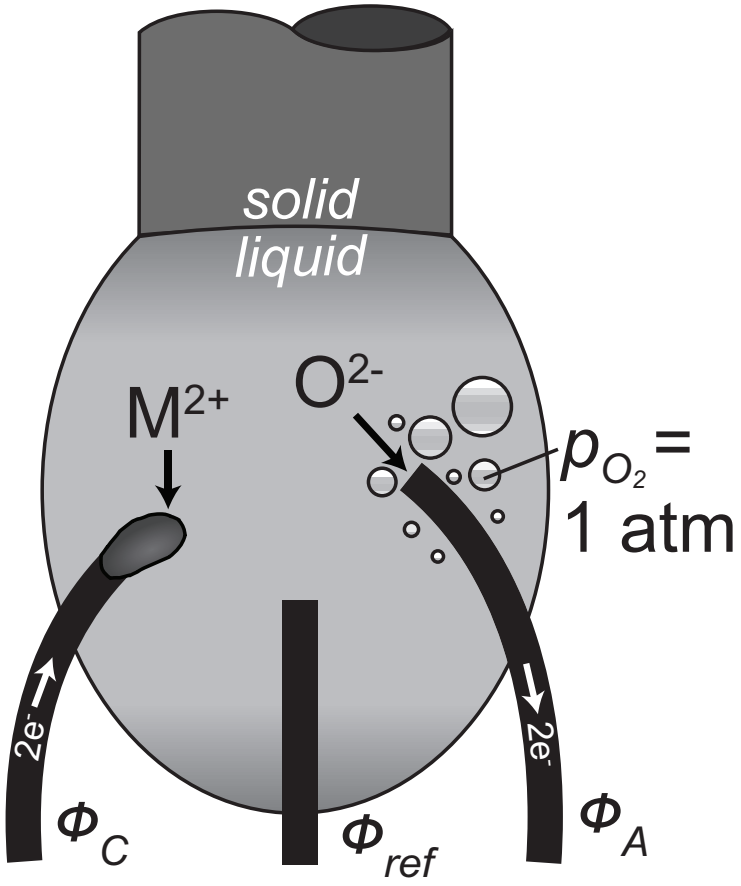

Figure 5-1: Envisioned condition of the molten droplet and electrodes during cell polarization $U > U_C^* > U_A^*$. ϕ_C, ϕ_{ref} and ϕ_A are the inner electric potentials of the cathode, RE and anode, resp.

of ACV signals and product state correlation is considered in more detail in the following section).

2. Measure the cell resistance ($R_{cell,A}^*$) during cell polarization to $V(E_A^*)$ employing potentiostatic EIS; applying ohmic compensation to determine decomposition voltage:

$$U(E_A^*) = V(E_A^*) - I(E_A^*)R_{cell,A}^*$$

3. Determine the minimum cell voltage ($V(E_C^*)$) and current ($I(E_C^*)$) to drive the target reaction occurring on the reactive cathode by means of ACV harmonic

analysis.

4. Measure the cell resistance ($R^*_{cell,C}$) during cell polarization to $V(E^*_C)$; applying ohmic compensation to determine decomposition voltage:

$$U(E^*_C) = V^*_C - I^*_C R^*_{cell,C}$$

5. If $U(E^*_C) > U(E^*_A)$, then $U(E^*_C)$ corresponds to the decomposition voltage (U^o) for Reaction 5.1.

6. If $U(E^*_C) < U(E^*_A)$, then the cell geometry is inappropriate for U^o measurement. One would then increase the electroactive area of the cathode (A_C) relative to the anode (A_A) in accordance with Eq. 5.8, which is expected to increase the magnitude of $U(E^*_C)$ relative to $U(E^*_A)$. The preceding steps are repeated sequentially until U^o is obtained.

5.2.3 Verification of signal interpretation

The correlation between the ACV response, electrode potentials and states of the products of the electrode reactions may be verified by means of experimental observations, electrochemical modeling or, ideally, a combination of both. Electrochemical modeling of the reactions was not pursued in the present work given the lack of relevant experimental investigations. However, perhaps, the results presented herein may serve as a basis for future development in this area. Experimentally, the correlation between E^*_A and Reaction 5.2 may be confirmed by:

1. Visual observation of gas evolution in the vicinity of the anode during experiments attendant with anode polarization greater than or equal to E^*_A,

2. Measurement of an attendant increase in oxygen concentration in the furnace exhaust gas following anode polarization greater than or equal to E^*_A, and

3. Post-experimental observations indicating negligible corrosion of the anode during polarization.

If any of these conditions are not observed, then Reaction 5.2 does not likely correspond to the identified ACV feature coinciding with E_A^*. Therefore, a reformulation of the analysis or different experimental conditions are required.

The correlation between E_C^* and Reaction 5.3 may be confirmed by systematic investigation of the variation of the resultant cathode deposit's morphology, structure and composition obtained via potentiostatic electrolysis with the cell voltage relative to $V(E_C^*)$.

5.3 Perspectives

Decomposition voltage measurements for UHT oxide melts are challenged by:

1. The cell design (electrodes, membrane, container, etc.) is hindered by material compatibility challenges.

2. A true RE for these systems is unknown or does not exist.

3. Conventional electrochemical methods exhibit limited reliability for relating the states of products of half-cell reactions and measured electrode potentials during cell polarization.

4. Dissolution of product metal in electrolyte contributes to electronic depolarization.

Therefore, the present method described up to now was formulated to:

1. Minimize the cell material requirements using three, stationary electrodes (anode, cathode and RE) without need for a membrane or container;

2. Utilize a "polarized dynamic" oxygen electrode as a reference energy level, while employing a pseudo-RE for separate investigation of the electrochemical reactions occurring on the cathode and anode;

3. Correlate precisely the states of products of half-cell reactions and measured electrode potentials during electrolytic decomposition by utilizing ACV;

4. Minimize electronic depolarization effects by minimizing depositing metal activity (reactive cathode) and duration of metal exposure to electrolyte (dynamic ACV measurements).

The present analysis was limited to the specific, idealized case involving oxygen gas evolution on an inert anode and liquid alloy formation on a reactive cathode using a molten oxide electrolyte. However, extension of this approach may be possible for other high temperature electrolytes (sulfides, fluorides etc.) and electrode reactions of a different nature, such as gas evolution on a reactive anode (e.g. carbon dioxide evolution on graphite) or intermetallic compound formation on a reactive cathode.

5.4 Materials selection for electrodes

For investigations in molten Al_2O_3, Y_2O_3 and La_2O_3, Ir was selected as a material satisfying the requirements for all electrodes.

As an anode and pseudo-RE, Ir has been observed to exhibit inert behavior molten silicates [17]. The melting point of Ir was determined to be $T_{fus} = 2719$ K [18], [19], which is greater than the reported melting points for pure Al_2O_3, Y_2O_3 and La_2O_3. Therefore, Ir is identified as a possible candidate for an inert anode in these refractory oxide melts.

Ir is known to strongly interact with Al, La, Y at high temperature [20], [21]. In particular, solid Ir has a high solubility of Al (approx. 12 mol%) at the melting point of Al_2O_3 [22]. The phase diagrams for these systems [22]–[24] suggest that Al, La and Y deposition on Ir likely involves a transition from an Ir-rich solid solution phase to liquid alloy formation at UHT. However, this behavior requires further verification.

5.5 Summary

A decomposition voltage measurement method for testing the validity of the hypothesis of this work was described. The method involves utilizing the anode as a polarized dynamic oxygen electrode, providing a fixed, reference energy level with which to me-

asure the electrode potential coinciding with liquid alloy formation on a reactive cathode.

The approach was formulated to mitigate the anticipated challenges for decomposition voltage measurements in UHT oxide melts. Given the results presented in §3, ACV is anticipated to allow the precise correlation between the states of electroactive species and electrode potentials of faradaic reactions, and strategies were described for verifying this correlation. The assumptions and limits of the proposed approach were examined, and the possible extension of the approach to other electrochemical systems was noted.

Finally, iridium, given its UHT melting point and previously observed inert behavior in molten silicates, was selected as a suitable material for the cathode, anode and pseudo-RE for investigation of the oxide systems considered in this work.

In the following two chapters, the hypothesis will be tested utilizing the method described herein with the pseudo-unary system Al_2O_3 and the pseudo-binary system La_2O_3-Y_2O_3.

References

[1] E. R. Cohen, B. Holmstrom, I. Mills, J. Stohner, T. Cvitas, K. Kuchitsu, F. Paese, H. L. Strauss, A. J. Thor, J. . Frey, R. Marquardt, M. Quack, and M. Takami, "Quantities, units and symbols in physical chemistry," in *IUPAC Green Book*, 3rd ed., Cambridge: IUPAC & RSC Publishing, 2007, p. 251.

[2] D. J. Ives and G. J. Janz, *Reference Electrodes: Theory and Practice*. New York: Academic Press Inc., 1961, p. 651.

[3] T. Yokokawa, K. Kawamura, H. Maekawa, and N. Sawaguchi, "Equilibrium of $O_{2\text{-}}+O_0=2O_{\text{-}}$ in oxide melts–Examinations of its reality by three approaches," *J. Mol. Liq.*, vol. 83, pp. 311–321, 1999.

[4] J. A. Duffy and M. D. Ingram, "Establishment of an optical scale for lewis basicity in inorganic oxyacids, molten salts, and glasses," *J. Am. Chem. Soc.*, vol. 93, no. 24, pp. 6448–6454, 1971.

[5] J. A. Duffy, "Optical basicity: a practical acid-base theory for oxides and oxyanions," *J. Chem. Educ.*, vol. 73, no. 12, p. 1138, 1996.

[6] ——, "The electronic polarisability of oxygen in glass and the effect of composition," *J. Non. Cryst. Solids*, vol. 297, no. 2-3, pp. 275–284, 2002.

[7] A. J. Gmitter, "The influence of inert anode material and electrolyte composition on the electrochemical production of oxygen from molten oxides," Masters Thesis, Massachusetts Institute of Technology, 2008, p. 116.

[8] A. Caldwell, E. Lai, A. Gmitter, and A. Allanore, "Influence of mass transfer and electrolyte composition on anodic oxygen evolution in molten oxides," *Electrochim. Acta*, vol. 219, pp. 178–186, 2016.

[9] A. Allanore, "Electrochemical engineering of anodic oxygen evolution in molten oxides," *Electrochim. Acta*, vol. 110, pp. 587–592, 2013.

[10] L. B. Skinner, A. C. Barnes, P. S. Salmon, L. Hennet, H. E. Fischer, C. J. Benmore, S. Kohara, J. K. R. Weber, A. Bytchkov, M. C. Wilding, J. B. Parise, T. O. Farmer, I. Pozdnyakova, S. K. Tumber, and K. Ohara, "Joint diffraction and modeling approach to the structure of liquid alumina," *Phys. Rev. B*, vol. 87, no. 2, p. 024 201, 2013.

[11] B. O. Mysen and P. Richet, *Silicate Glasses and Melts Properties and Structure*, 1st ed. Boston: Elsevier, 2005, p. 560.

[12] J. Giner, "A practical reference electrode," *J. Electrocehmical Soc.*, vol. 111, no. 3, pp. 376–377, 1964.

[13] A. Küver, I. Vogel, and W. Vielstich, "Distinct performance evaluation of a direct methanol SPE fuel cell. A new method using a dynamic hydrogen reference electrode," *J. Power Sources*, vol. 52, no. 1, pp. 77–80, 1994.

[14] T. Nann and G. A. Urban, "New dynamic hydrogen reference electrode for applications in thin-film sensor systems," *Sensors Actuators, B Chem.*, vol. 70, no. 1-3, pp. 188–195, 2000.

[15] S. K. Cho, S.-K. Lee, E.-Y. Choi, and J.-M. Hur, "The evaluation of polarized dynamic reference electrode (p-Dyn RE) for LiCl-1 wt% Li_2O molten salt at 650°C: Li+/Li p-Dyn RE versus O_2/O^{2-} p-Dyn RE," *J. Electrochem. Soc.*, vol. 163, no. 10, E308–E312, 2016.

[16] V. K. Afonichkin, A. L. Bovet, V. V. Ignatiev, A. V. Panov, V. G. Subbotin, A. I. Surenkov, A. D. Toropov, and A. L. Zherebtsov, "Dynamic reference electrode for investigation of fluoride melts containing beryllium difluoride," *J. Fluor. Chem.*, vol. 130, pp. 83–88, 2009.

[17] H. Kim, J. Paramore, A. Allanore, and D. R. Sadoway, "Stability of iridium anode in molten oxide electrolysis for ironmaking: influence of slag basicity," *ECS Trans.*, vol. 33, no. 7, pp. 219–230, 2010.

[18] R. E. Bedford, G. Bonnier, H. Maas, and F. Pavese, "Recommended values of temperature on the International Temperature Scale of 1990 for a selected set of secondary reference points," *Metrologia*, vol. 33, pp. 133–154, 1996.

[19] F. Henning and H. T. Wensel, "The freezing point of iridium," *Bur. Stand. J. Res.*, vol. 10, no. 6, pp. 809–821, 1933.

[20] L. Brewer and P. R. Wengert, "Transition metal alloys of extraordinary stability; An example of generalized Lewis-acid-base interactions in metallic systems," *Metall. Trans.*, vol. 4, no. 1, pp. 83–104, 1973.

[21] F. R. de Boer, R. Boom, W. C. M. Mattens, A. R. Miedema, and A. K. Niessen, *Cohesion in Metals: Transition Metal Alloys*, F. R. de Boer and D. G. Pettifor, Eds. New York: North-Holland, 1988, p. 758.

[22] T. Abe, C. Kocer, M. Ode, H. Murakami, Y. Yamabe-Mitarai, K. Hashimoto, and H. Onodera, "Thermodynamic re-assessment of the Al-Ir system," *Calphad*, vol. 32, no. 4, pp. 686–692, 2008.

[23] H. Okamoto, "The Ir-La (iridium-lanthanum) system," *J. Phase Equilibria*, vol. 12, no. 5, pp. 565–567, 1991.

[24] ——, "The Ir-Y (iridium-yttrium) system," *Phase Diagr. Eval.*, vol. 13, no. 6, pp. 651–653, 1992.

Chapter 6

Electrochemical study of molten Al_2O_3

The method for UHT decomposition voltage measurement presented in §5 were applied to the pseudo-unary component electrolyte, molten Al_2O_3. A systematic investigation of the electrochemical behavior of Ir electrodes in molten Al_2O_3 was pursued to verify ACV signal interpretation for this system. Measurements of decomposition voltage were utilized to determine the chemical potential and entropy of Al in an Ir-rich alloy liquid. The results are compared with previous predictions. For more details, the reader is referred to Nakanishi et al. [1], also available in Appendix C.

6.1 Background

Al_2O_3 was identified as an exemplary pseudo-unary candidate for testing the hypothesis of the present contribution for its thermal stability and likely ionic nature. Furthermore, Al_2O_3 is, perhaps, the most thoroughly investigated refractory oxides in the molten state [2]–[25]. Although hypothesized previously [26], the electrolytic nature of molten Al_2O_3 has yet to be confirmed.

6.2 Experimental

Details regarding sample and electrode preparation, electrochemical measurements, temperature measurement, operations, post-experiment analysis during experiment are described in Appendix C. The description below is limited to that required for interpreting the results reported in the present chapter.

Two thermal imaging furnaces (TIF's) were employed (models FZ-T-12000-X-IV-VP and TX-12000-I-MIT-VPO-PC, Crystal Systems Corp.), which will hereafter be designated TIF-I and TIF-II, resp. Unless noted otherwise, the following results were obtained with TIF-II.

The inside of a quartz tube enclosing the sample and electrode assembly was evacuated and refilled three times with one of three gases designated hereafter as "Gas A", "Gas B" and "Gas C", for which compositions are presented in Table 6.1.

Table 6.1: Details of gas compositions employed

Gas	**Description**	p_{O_2} / **Pa**
A	Airgas UHP Ar I	0.8
B	Airgas UHP Ar II	10
C	Airgas 990 ppm calibration gas, balance Ar	990

A three-electrode configuration was employed using Ir wires for the WE, CE and pseudo-RE electrodes. The RE consisted of an Ir wire immersed in the molten droplet. All measured potentials are referred to this RE, unless stated otherwise. Three electrode geometries were employed in this study to vary the immersed electrode surface area:

1. a single Ir wire, geometric surface area $A_G = 0.07$ cm^2;

2. a single Ir wire that was approximately 2 mm longer, $A_G = 0.13$ cm^2; or

3. two Ir wires previously tungsten inert gas-welded together at their tips forming a spherical junction, $A_G = 0.25$ cm^2.

The RE was constructed using the first geometry. The WE and CE were constructed using one of the three geometries for each experiment.

For ACV measurements, the behavior of the WE at negative and positive potentials were studied in separate experiments. Additionally, during a subset of measurements, the cell voltage was simultaneously recorded. For this subset of measurements, the behavior of the WE at negative and positive potentials versus OCP was studied on separate electrodes (designated as "cathode" and "anode," resp.) within the same experiment.

Direct current (dc) WE and cell voltages were corrected for ohmic drop using the product of the dc-component of the total current response ($I_{0\omega}$) with a resistance determined by EIS at relevant polarized conditions. Variation in the open circuit impedance with TIF lamp power was used to evaluate temperature.

The phase compositions within the post-quenched, sectioned and polished droplets and electrodes were determined using energy dispersive X-ray spectroscopy (EDS). Further details regarding measurements and post-experiment sample preparation are described in Nakanishi et al. [1], available in Appendix C.

6.3 Results & discussion

6.3.1 Evidence for the electrolytic nature of molten Al_2O_3

Electrolysis was performed on Al_2O_3 droplets at constant lamp power (temperature) using three Ir electrodes to ascertain its electrolytic behavior. As shown in Figure 6-1a, gas bubbling was observed always in the vicinity of the anode. The evolving gas was confirmed to be composed of oxygen gas by an oxygen sensor analyzing the gas exhaust from the furnace. Typical variation of the cell voltage U, cathode and anode potentials (E_C and E_A, resp.) and current I during electrolysis of Al_2O_3 are shown in Figure 6-1b. The droplet and electrodes, quenched after electrolysis by shutting off the TIF lamps, showed the electrodes prior were visually unchanged, while a deposited layer originating from a solidified liquid Al-Ir alloy was observed at the cathode-

electrolyte interface, as shown in Figure 6-2. Four distinct regions were observed on the cathode (I-IV in Figure 6-2b). In the regions closest to the electrolyte interface (III and IV) two phases were observed with respective mole fractions Al $X_{Al} = 0.4$ and $X_{Al} = 0.14$. Comparison of these phase compositions with the phase diagram optimized by Abe et al. [27] shown in Figure 6-3 supports that an Al-Ir liquid alloy had formed on the Ir cathode.

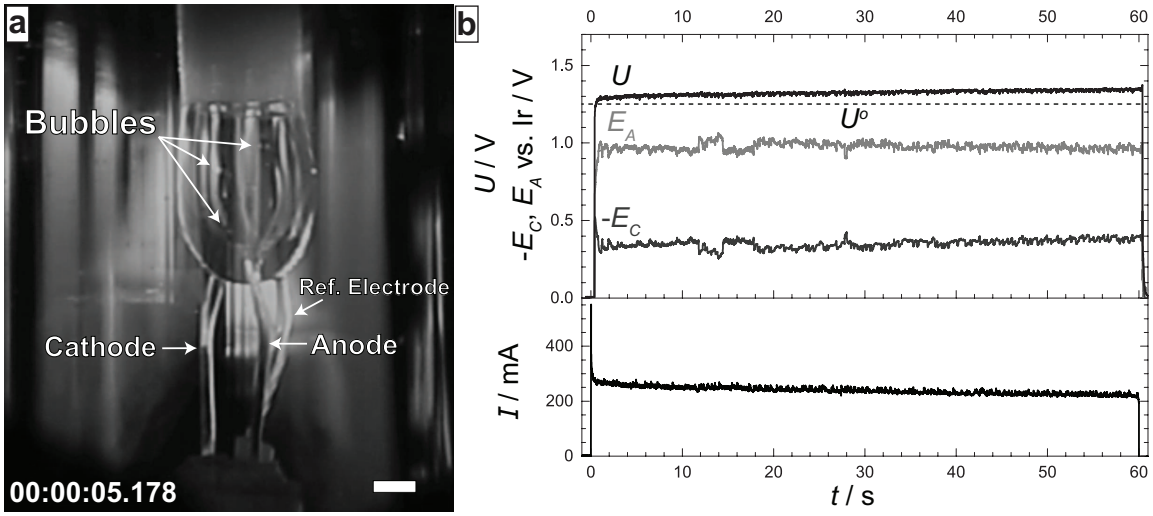

Figure 6-1: a. Image of Al_2O_3 droplet during electrolysis, scale bar 2 mm; b. Electrochemical signals for cell voltage (U), anode (E_A) and cathode (E_C) potentials, and current (I) during potentiostatic electrolysis at 1.6 V; At $t = 60$ s, the lamps were shut off ($Q = 14.32$ C, $A_{G,C} = 0.07$ cm^2, $A_{G,A} = 0.25$ cm^2, $T = 2465$ K, Gas C).

These results show that molten Al_2O_3 decomposes under an applied electric field, confirming the ionic nature of this material. Subsequently, the reactions occurring at the anode, cathode and RE were investigated further.

6.3.2 Electrochemical behavior of the anode, cathode & reference electrode

A typical ACV voltammogram for the first, second and third harmonics of the current response versus dc potential are shown in Figure 6-4. For positive potentials, the electrode labeled "anode" served as the WE. A faradaic event corresponding with the half-cell reaction between oxide ions O^{2-} in the melt and oxygen gas $O_2(g)$ at

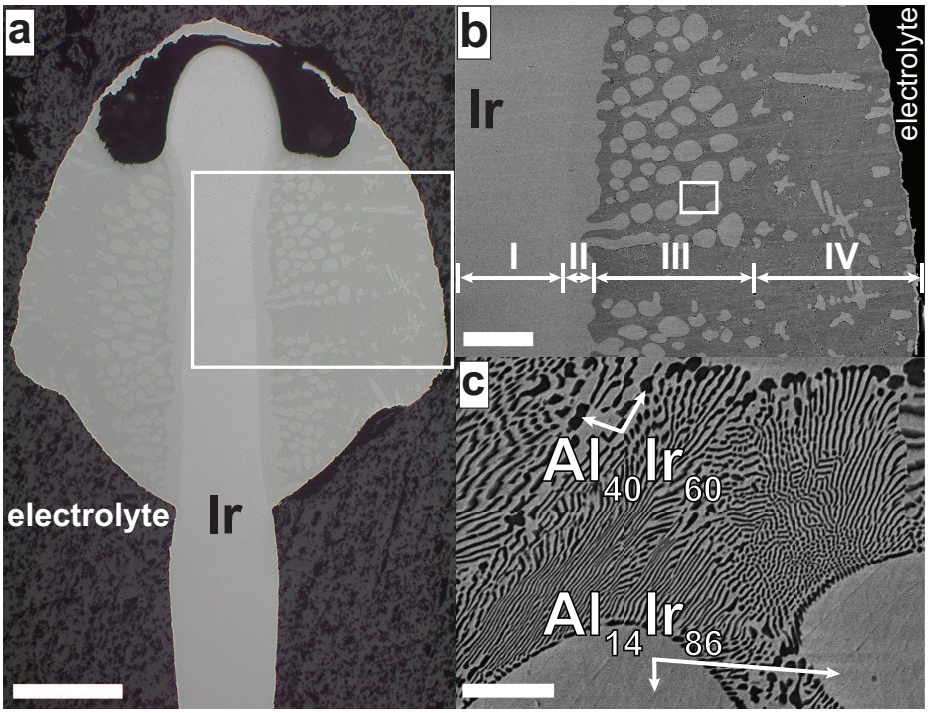

Figure 6-2: a. Optical micrograph of cathode cross-section after experiment shown in Figure 6-1b (scale bar 300 μm); b. back-scattered electron (BSE) image of boxed area in a. (scale bar 100 μm); c. High-magnification BSE image of boxed area in b. (scale bar 10 μm, quantitative analysis from EDS).

101,325 Pa given by

$$O^{2-}(melt) = 2e^- + \frac{1}{2}O_2(g) \tag{6.1}$$

was observed at a half-wave potential E_A^* with a characteristic peak-splitting feature across the second and higher harmonics.

The correspondence between E_A^* and Reaction 6.1 was confirmed by visual observation of the anode and droplet during polarization and a systematic investigation of the behavior of E_A^*. During positive-going scans, gas bubbles were observed at the surface of the droplet immediately after $E = E_A^*$ was attained. Conversely, bubbling subsided immediately after the anode potential was scanned below E_A^* during negative-going scans. Additionally, gas composition was found to influence the value of E_A^*, as shown in Figure 6-5. In fact, for the conditions investigated, its behavior

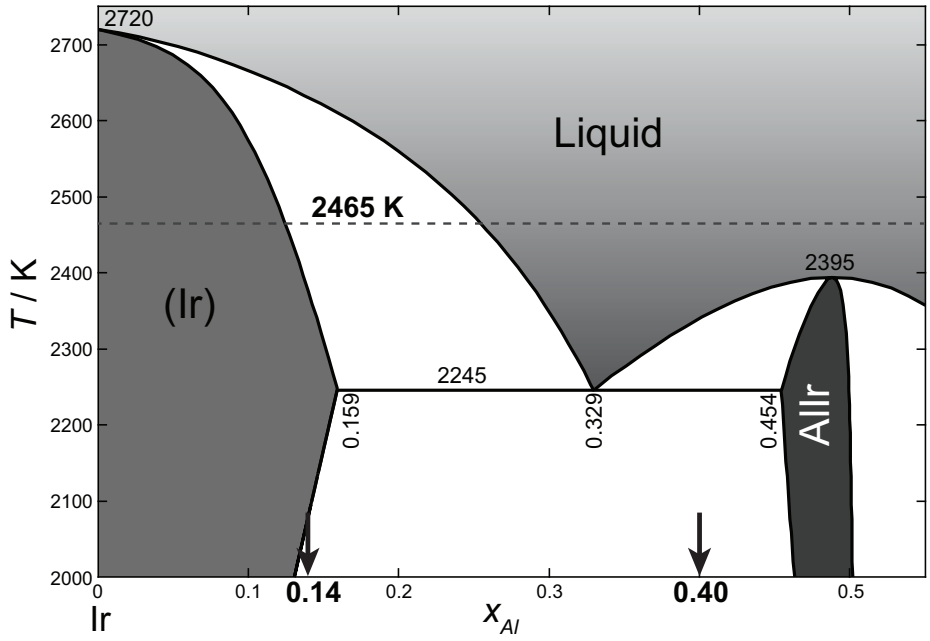

Figure 6-3: Ir-rich portion of the Ir-Al phase diagram calculated using FactSage [28] using the optimized parameters of Abe et al [27]. The approximate temperature during electrolysis is shown by the dashed line; arrows mark the alloy phase compositions observed upon solidification of the cathode after potentiostatic electrolysis, cf. Figure 6-2c

was observed to be approximately described by

$$E_A^* = \phi_A^* - \phi_{ref,A}^* \approx -\frac{RT}{4F} \ln(p_{O_2,furnace}) \tag{6.2}$$

where $p_{O_2,furnace}$ is the partial pressure of oxygen in the furnace atmosphere, ϕ_A^* and $\phi_{ref,A}^*$ are the inner potentials of the anode and RE during E_A^* measurement, and R, T and F have their usual meanings. Such situation is possible when:

1. the reaction occuring on the anode at E_A^* was indeed Reaction 6.1
2. the Ir pseudo-RE behaves as an oxygen electrode, sensitive to $p_{O_2,furnace}$
3. negligible activation overpotentials were present

For negative potentials, a faradaic event is observed at E_C^* with its own peak splitting feature, as shown in Figure 6-4 for a distinct electrode labeled "cathode." The corresponding half-cell reaction describing the reduction of aluminum ions Al^{3+}

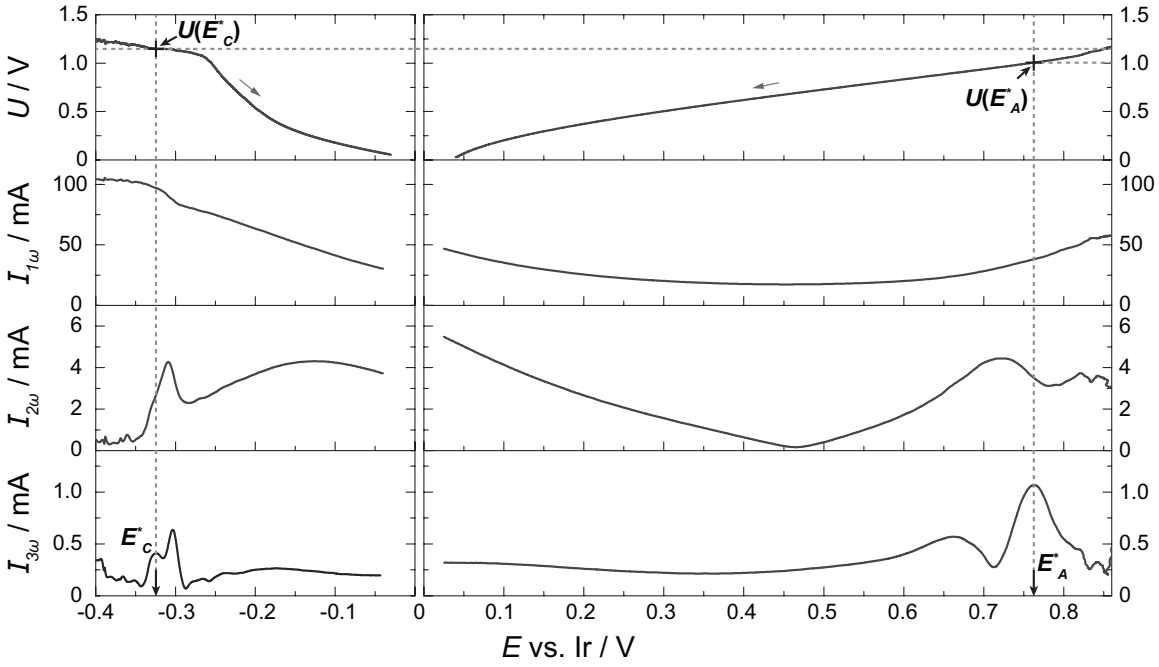

Figure 6-4: From top to bottom panel, dc component of cell voltage and first, second and third harmonic current responses obtained during ACV measurements. $E < 0$ corresponds to cathode polarization study (cathode geometric surface area $A_{G,C} = 0.07$ cm^2, applied dc potential scan limits -0.55 to 0 V vs. Ir); while $E > 0$ is an anodic polarization study (anode $A_{G,A} = 0.13$ cm^2, $+0.95$ to 0 V vs. Ir). For both, $E_{ac} = 120$ mV, $f = 23$ Hz, $\nu = 20$ mV s^{-1}, $T = 2377$ K and Gas A. The quantities E^*_A, E^*_C, $U(E^*_A)$ and $U(E^*_C)$ are defined in the text.

to Al alloyed with Ir is given by:

$$Al^{3+}(melt) + 3e^- = \underline{Al}(l) \tag{6.3}$$

and the value of E^*_C is related to the inner potentials of the cathode and RE by

$$E^*_C = \phi^*_C - \phi^*_{ref,C}$$

The correspondence between Reaction 6.3 and E^*_C is inferred from the following:

1. The typical cathodic product for electrolysis at $E < E^*_C$, described in the preceding section confirms formation a liquid Al-Ir alloy.

2. Electrolysis at $E > E^*_C$ (less negative), shows no indication of liquid Al-Ir alloy

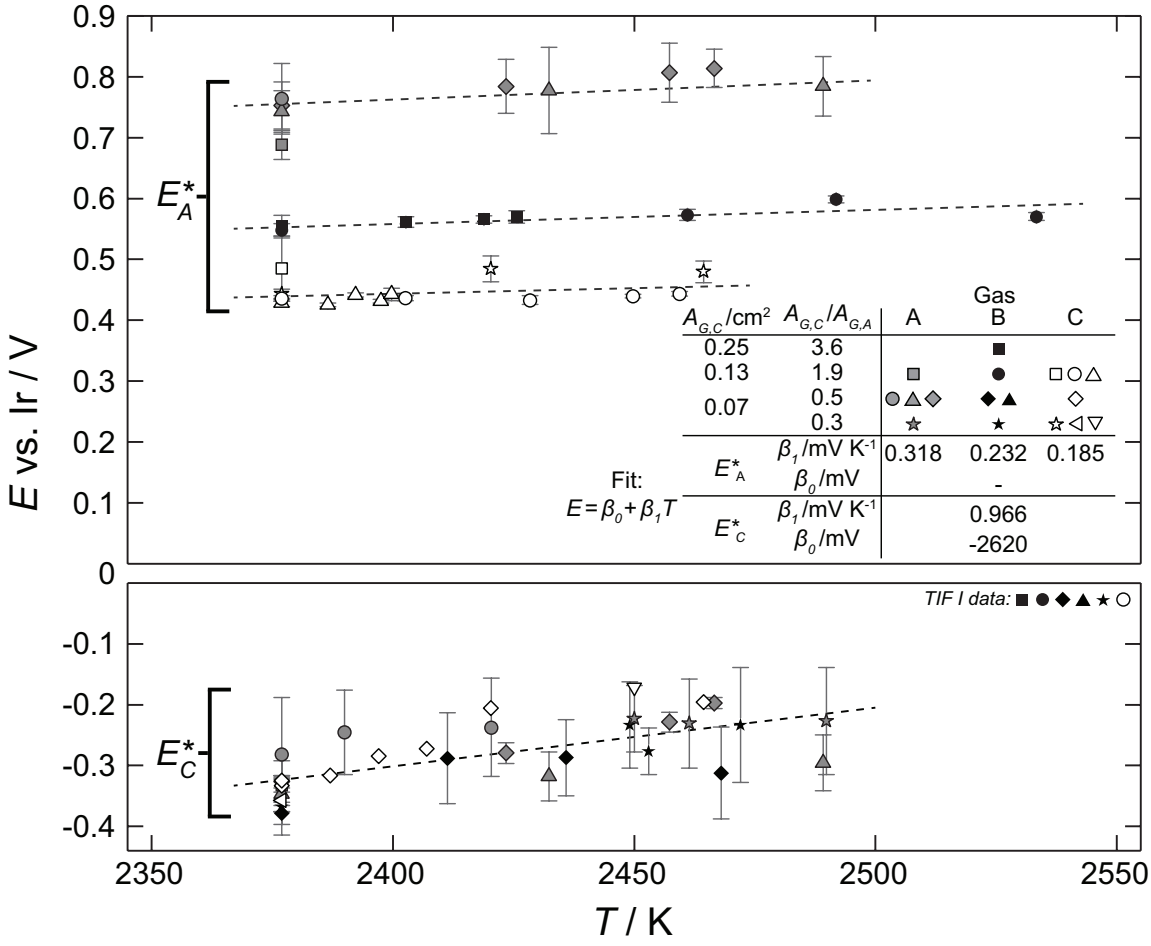

Figure 6-5: Variation of E_A^* (top) and E_C^* (bottom) with temperature for various electrode configurations and gas atmospheres (error bars represent 1σ uncertainty from multiple scans in both cathodic and anodic directions and lines show fitting according to $E = \beta_0 + \beta_1 T$). Note, E_A^* was fitted with a single, first-order parameter (β_1), and E_C^* was fitted with zeroth (β_0) and first-order (β_1) parameters. [1]

formation, with a content of Al in the Ir cathode below the detection limit of EDS.

3. Formation of aluminum suboxide gaseous species, e.g. AlO(g) or Al_2O(g), are thermodynamically unfavorable for the relevant conditions and therefore are unlikely to form by electrolytic reduction.

4. Finally, larger dc current density magnitudes were observed for the reaction coinciding with E_C^* ($j \approx 6000$ mA cm^{-2}) versus that for E_A^* ($j \approx 1200$ mA

cm^{-2}), which agrees the relative nature of the reactions: liquid-liquid at the cathode versus liquid-gas at the anode.

The relative invariance of E_C^* with respect to $p_{O_2,furnace}$ shown in Figure 6-5 is an interesting feature. This result suggests that the potential of the RE is sensitive to the reactions occurring at the nearby cathode. Given the preceding discussion for the RE behavior during E_A^* measurement, this phenomenon likely occurs due to a depression of the oxygen potential at the RE, perhaps, by rapid transport (in comparison to that of oxygen from the droplet surface) of $Al(l, Ir)$ from the cathode surface to the RE.

Nevertheless, the results presented confirm that Reactions 6.1 and 6.3 coincide with signals observed during E_A^* and E_C^* measurement, resp. The potentials of these reactions were measured precisely thanks to ACV. Furthermore, an Ir RE in an Al_2O_3 droplet behaves like an oxygen electrode, sensitive to $p_{O_2,furnace}$ in certain conditions. However, a well-defined reference energy level is needed to permit comparison of decomposition voltage measurements with tabulated thermodynamic data, which is the subject of the following section.

6.3.3 Decomposition voltage measurements

The method of decomposition voltage measurement described in §5 was applied to molten Al_2O_3 using Ir electrodes. In the present case, μ_{O_2} was concluded to differ from $\mu_{O_2}^o$ by at most 1% for all practical conditions during oxygen gas evolution. This conclusion was justified considering:

1. surface tension effects for the observed bubble radii formed during polarization measurements

2. the relatively low vapor pressure of Al_2O_3(l) ($p^o(T_{fus}) \approx 0.2$ Pa) [28]

The cell voltages (U) measured at E_A^* and E_C^* are also shown in Figure 6-4, hereafter designated $U(E_A^*)$ and $U(E_C^*)$. In practice, $U(E_C^*)$ was observed to be greater than $U(E_A^*)$, satisfying the criterion for decomposition voltage measurement described in

§5.2.1, when the cathode to anode area ratio ($A_{G,C}/A_{G,A}$) was greater than 0.5 and 0.3 for Gases A and C, resp.

Here, U^o ($= \phi_A^* - \phi_C^*$) was identified as the thermodynamic minimum decomposition potential difference to drive the overall cell reaction:

$$Al_2O_3(l) \rightarrow 2\underline{Al}(l) + \frac{3}{2}O_2(g) \tag{6.4}$$

Measurements of U^o as a function of temperature for Gases A and C are presented in Figure 6-6. A linear unweighted fitting for all data using an equation of the form $U^o = \beta_0 + \beta_1 T$ yields $\beta_0 = 2380 \pm 570$ mV and $\beta_1 = -0.50 \pm 0.24$ mV K^{-1}. The corresponding Gibbs energy change for Reaction 6.4 may be computed via

$$\Delta_r G = 6FU^o = 2\mu_{\underline{Al}(l)} + \frac{3}{2}\mu^o_{O_2} - \mu^o_{Al_2O_3} \tag{6.5}$$

where $\mu^o_{O_2}$ and $\mu^o_{Al_2O_3}$ are the standard chemical potentials of $O_2(g)$ and Al_2O_3(l) (standard state pure liquid, at T and $p = 101,325$ Pa), resp., and $\mu_{\underline{Al}(l)}$, or simply $\mu_{\underline{Al}}$, is the chemical potential of Al in the two-phase region corresponding to the Ir solid solution and Ir-rich liquid equilibrium shown in Figure 6-3).

6.3.4 Comparison with available thermodynamic data

Using tabulated data for $\mu^o_{O_2}$ [29] and $\mu^o_{Al_2O_3}$ [17] and our experimental data for U^o from Figure 6-6, $\mu_{\underline{Al}}$ was determined from Eq. 6.5

$$\mu_{\underline{Al}} = 3FU^o - \frac{3}{4}\mu^o_{O_2} + \frac{1}{2}\mu^o_{Al_2O_3}$$

The corresponding $\mu_{\underline{Al}}$ variation with temperature is presented in Figure 6-7. The average partial molar entropy $S_{\underline{Al},avg}$ for the measured temperature range ($T = 2377$ to 2489 K) was 114.4 J mol^{-1} K^{-1} ($\pm$60% error). The accuracy of entropy measurements is related to the measurement errors of U^o and T variation (since entropy is proportional to the first derivative of U^o with respect to temperature). The instrument precision for U^o measurements was around $\pm$1 mV and were repeatable within

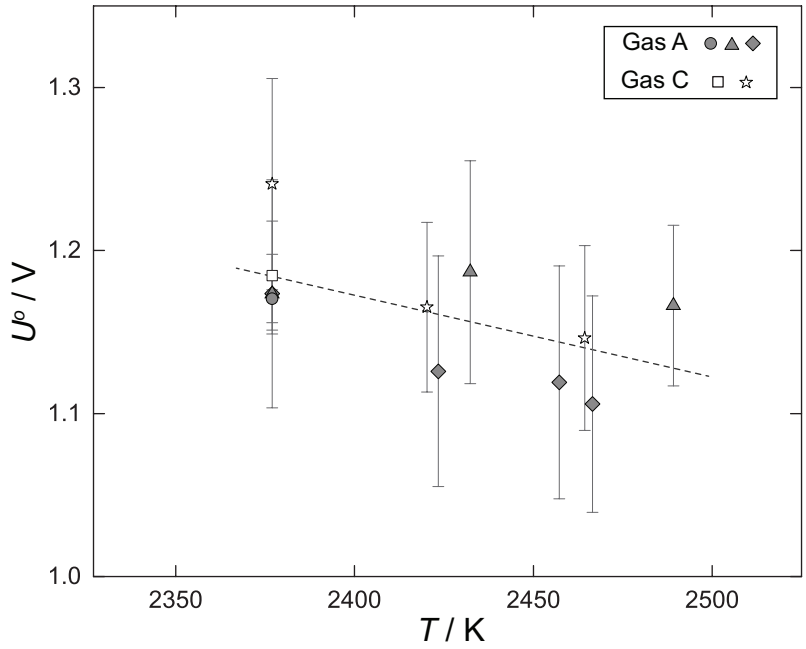

Figure 6-6: Variation of U^o with temperature for gases A and C.

5% on average. Although the error for determining relative temperature variation was < 10 K using the impedance-based method, the absolute temperature, used to anchor an experimental dataset, could be determined only within an estimated accuracy of ± 50 K. Therefore, the latter uncertainty contributed most significantly to the relatively large error on $S_{\underline{Al},avg}$.

For comparison, the chemical potential of Al for the liquid and fcc solid-solution phase equilibrium in the Ir-rich portion of the binary Al-Ir system was also calculated using FactSage [28]. Model parameters for this binary equilibrium are from the most recent Al-Ir thermodynamic assessment [27]. The fit of our experimental data for $\mu_{\underline{Al}}$, averaging -285.4 kJ mol^{-1} for the measured temperature range, is less than 7% greater than $\mu_{\underline{Al}}$ calculated using FactSage. $S_{\underline{Al},avg}$ was 36% lower than the calculated value (180 J mol^{-1} K^{-1}). As pointed out by Abe et al. [27], no experimental data for the liquid phase was available, and the Gibbs energy model for the liquid phase was fit to available data for the eutectic phase boundary ($T = 2245$ K) while maintaining ideal entropy of mixing. Given these circumstances, the agreement is remarkable and further supports the validity of the postulated descriptions for Reaction 6.1, E_A^* and $U(E_A^*)$ as well as Reaction 6.3, E_C^* and $U(E_C^*)$.

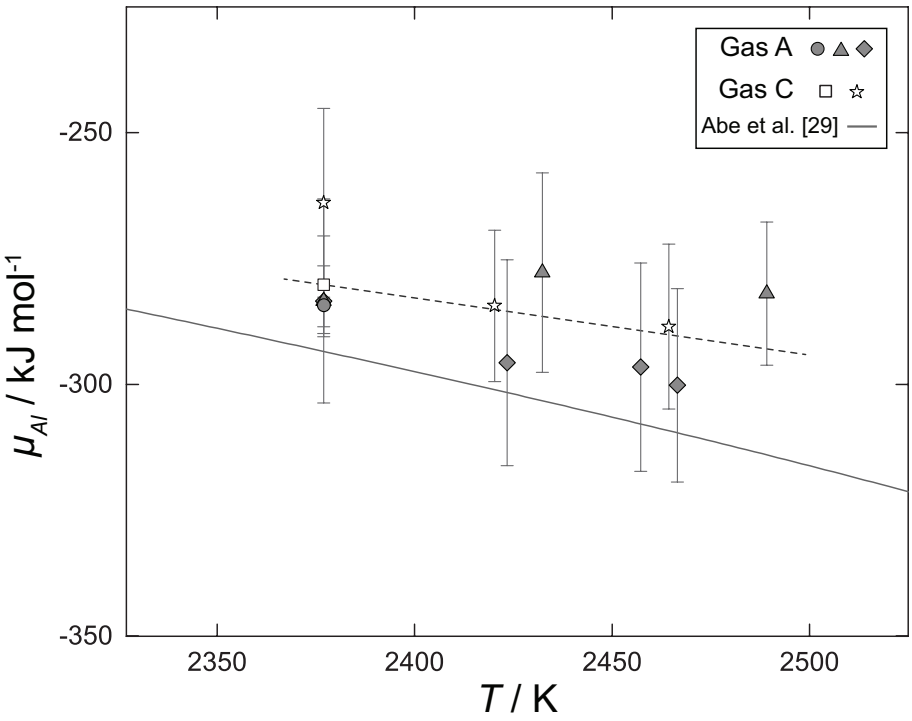

Figure 6-7: Variation of measured Al chemical potential ($\mu_{\underline{Al}}$) versus temperature at the Ir-rich, solid-liquid phase boundary of the Al-Ir phase diagram; linear fit (dashed line). Results from the recent thermodynamic assessment [27] for the Al-Ir system are shown for comparison as a plain line.

6.4 Summary

For the first time, the direct electrolytic decomposition of molten Al_2O_3 to O_2 gas and Al metal (alloyed with Ir) was observed, confirming the ionic nature of molten Al_2O_3. Oxygen gas evolution and Al deposition from the pseudo-unary component electrolyte, Al_2O_3, were observed on the Ir anode and cathode, resp.

Using ACV, the reactions coinciding with oxygen gas evolution on the anode and formation of Al-Ir alloy liquid on the cathode were detected and their electrode potentials were measured. These faradaic reactions exhibited unique peak splitting features among the second and higher current harmonics, permitting reaction potential measurements with relatively high accuracy and precision.

A systematic investigation of oxygen evolution on an Ir anode demonstrates that the Ir pseudo-RE behaves like an oxygen electrode exhibiting sensitivity to the partial pressure of oxygen in the furnace atmosphere. Furthermore, for the conditions

investigated, Ir is inert as an anode, exhibiting remarkable stability during formation of O_2 gas. However, the Ir RE's sensitivity to furnace atmosphere was lost during the investigation of the formation of liquid Al-Ir alloy on the cathode as exemplified by the lack of variation in E_C^* with $P_{O_2,furnace}$. These results likely indicate that such a RE's potential is sensitive to reactions occurring on the cathode and anode at close proximity in a pendant droplet.

The electrolytic cell method proposed in §5 was validated by comparing decomposition voltage measurements in the molten Al_2O_3 with available tabulated data. The decomposition voltage of molten Al_2O_3 was measured with high precision using ACV and demonstrated remarkable sensitivity to temperature. The chemical potential and partial molar entropy of Al in the Al-Ir alloy liquid at the Ir-rich solid-liquid phase boundary were determined and found to be in remarkably close agreement with previous predictions [27]. A significant error for entropy ($\pm 60\%$) persisted due to error in determining absolute temperature. Nevertheless, these results provide evidence for the validity of the hypothesis. Indeed with appropriate ohmic compensation, contributions due to polarization are found to be negligible, permitting measurement of the chemical potential and partial molar entropy of Al in the liquid Al-Ir alloy from $T = 2377$ to 2485 K by the electrolytic cell method.

References

[1] B. R. Nakanishi and A. Allanore, "Electrochemical study of a pendant molten alumina droplet and its application for thermodynamic property measurements of Al-Ir," *J. Electrochem. Soc.*, vol. 164, no. 13, E460, 2017.

[2] H. Moissan, "Action d'une haute temperature sur les oxydes metalliques," *C. R. Hebd. Seances Acad. Sci.*, vol. 115, pp. 1034–1036, 1892.

[3] R. J. Ackermann and R. J. Thorn, "Gaseous oxides of aluminum, tungsten and tantalum," *Communications*, vol. 81, no. 1934, pp. 4744–4745, 1956.

[4] A. E. van Arkel, E. A. Flood, and N. F. H. Bright, "The electrical conductivity of molten oxides," *Can. J. Chem.*, vol. 31, no. 11, p. 1009, 1953.

[5] P. B. Kantor, L. S. Lazareva, V. V. Kandyba, and E. N. Fomichev, "Experimental measurements of enthalpy, temperature and heat of melting of α-Al_2O_3 at 1200-2500 K," *Ukr. Fiz. Zhurnal*, vol. 7, pp. 205–211, 1962.

[6] H. Fay, "The electrical conductivity of liquid Al_2O_3 (molten corundum and ruby)," *J. Phys. Chem.*, vol. 70, no. 3, pp. 890–893, 1966.

[7] J. J. Diamond and A. L. Dragoo, "Studies of molten alumina in the arc-image furnace," *Rev. Hautes Temp. Refract.*, vol. 3, no. 3, pp. 273–279, 1966.

[8] W. G. Field and R. W. Wagner, "Thermal imaging for single crystal growth and its application to ruby," *J. Cryst. Growth*, vol. 4, pp. 799–803, 1968.

[9] W. Gorski and A. Dietzel, "Melting point of alumina in air," *Rev. Hautes Temp. Refract.*, vol. 6, pp. 105–110, 1969.

[10] S. J. Schneider, "Cooperative determination of the melting point of alumina," *Pure Appl. Chem.*, vol. 21, p. 115, 1970.

[11] V. P. Elyutin, B. S. Mitin, and Y. A. Nagibin, "Electrical conductivity of molten aluminum oxide," *Izv. Akad. Nauk SSSR, Neorg. Mater.*, vol. 7, no. 5, pp. 880–881, 1971.

[12] V. I. Aleksandrov, V. V. Osiko, and V. M. Tatarintsev, "Electrical conductivity of aluminum oxide in the molten state," *Izv. Akad. Nauk SSSR, Neorg. Mater.*, vol. 8, no. 5, pp. 956–957, 1972.

[13] E. E. Shpil'rain, D. N. Kagan, and L. S. Barkhatov, "Thermodynamic properties of the condensed phase of alumina near the melting point," *High Temp.-High Press.*, vol. 4, no. 6, pp. 605–609, 1972.

[14] L. S. Barkhatov, D. N. Kagan, A. F. Tystsarkin, E. E. Shpil'rain, and A. K. Yakimovich, "Thermodynamic properties of molten aluminum oxide," *Teplofiz. Vys. Temp.*, vol. 11, no. 6, pp. 1188–91, 1973.

[15] E. N. Fornichev, V. P. Bondarenko, and V. V. Kandyba, "Enthalpy, heat of fusion, and melting point of corundum," *High Temp.-High Press.*, vol. 5, no. 1, 1973.

[16] L. S. Nelson, N. L. Richardson, K. Keil, and S. R. Skaggs, "Effects of oxygen and argon atmospheres on pendant drops of aluminum-oxide melted with carbon-dioxide laser radiation," *High Temp. Sci.*, vol. 5, no. 2, pp. 138–154, 1973.

[17] M. W. Chase, J. L. Curnutt, A. T. Hu, H. Prophet, A. N. Syverud, and L. C. Walker, "JANAF Thermochemical Tables, 1974 supplement," *J. Phys. Chem. Ref. Data*, vol. 3, no. 2, pp. 311–480, 1974.

[18] E. E. Shpil'rain, D. N. Kagan, L. S. Barkhatov, and L. I. Zhmakin, "Experimental study of specific electrical conductivity of molten aluminum oxide at temperature up to 3000 K," *Teplofiz. Vys. Temp.*, vol. 14, no. 5, pp. 948–952, 1976.

[19] R. D. Srivastava and M. Farber, "Thermodynamic properties of group 3 oxides," *Chem. Rev.*, vol. 78, no. 6, pp. 627–638, 1978.

[20] T. Yamada, M. Mizuno, M. Machida, A. Taguchi, and T. Noguchi, "Measurement of solidification points for ZrO_2, Y_2O_3 and Al_2O_3 by centrifugal method with a solar furnace," *Yogyo-Kyokai-Shi*, vol. 92, no. 1, pp. 50–52, 1984.

[21] N. Ikemiya, J. Umemoto, S. Hara, and K. Ogino, "Surface tensions and densities of molten Al_2O_3, Ti_2O_3, V_2O_5 and Nb_2O_5," *ISIJ Int.*, vol. 33, no. 1, pp. 156–165, 1993.

[22] S. Ansell, S. Krishnan, J. K. R. Weber, J. Felten, P. Nordine, M. Beno, D. Price, and M.-L. Saboungi, "Structure of liquid aluminum oxide," *Phys. Rev. Lett.*, vol. 78, no. 3, pp. 464–466, 1997.

[23] J. E. Enderby, S. Ansell, S. Krishnan, and D. L. Price, "The electrical conductivity of levitated liquids," *Appl. Phys. Lett.*, vol. 71, no. 1, pp. 116–119, 1997.

[24] B. Glorieux, F. Millot, and J. C. Rifflet, "Surface tension of liquid alumina from contactless," *Int. J. Thermop*, vol. 23, no. 5, pp. 1249–1257, 2002.

[25] M. L. Saboungi, J. Enderby, B. Glorieux, H. Schnyders, Z. Sungaila, S. Krishnan, and D. L. Price, "What is new on the levitation front?" *J. Non. Cryst. Solids*, vol. 312-314, pp. 294–298, 2002.

[26] J. D. Mackenzie, "Oxide melts," in *Advances in Inorganic Chemistry and Radiochemistry, Vol. 4*, H. J. Emeleus and A. G. Sharpe, Eds., New York: Academic Press Inc., 1962, pp. 293–318.

[27] T. Abe, C. Kocer, M. Ode, H. Murakami, Y. Yamabe-Mitarai, K. Hashimoto, and H. Onodera, "Thermodynamic re-assessment of the Al-Ir system," *Calphad*, vol. 32, no. 4, pp. 686–692, 2008.

[28] C. W. Bale, E. Bélisle, P. Chartrand, S. A. Decterov, G. Eriksson, A. Gheribi, K. Hack, I. H. Jung, Y. B. Kang, J. Melançon, A. D. Pelton, S. Petersen, C.

Robelin., J. Sangster, and M.-A. V. Ende, "FactSage thermochemical software and databases, 2015-2016," *Calphad*, vol. 54, pp. 35–53, 2016.

[29] D. R. Stull and H. Prophet, "JANAF Thermochemical Tables," *J. Phys. Chem. Ref. Data*, 1985.

Chapter 7

Electrochemical study of molten La_2O_3-Y_2O_3

The decomposition voltage method described in §5 was validated in the pseudo-unary component electrolyte Al_2O_3. Herein, the method is extended to the pseudo-binary melt La_2O_3-Y_2O_3. The electrochemical behavior of Ir electrodes in molten La_2O_3-Y_2O_3 was investigated as a function of composition ($X_{La_2O_3}$) using Ir electrodes to measure Gibbs energies for the pure end-member oxides and excess Gibbs energies at intermediate compositions. The results are compared with previous predictions.

7.1 Background

The system La_2O_3-Y_2O_3 was identified as a suitable candidate for testing the hypotheses of this work, likely to exhibit ionic behavior. Selected properties for these compounds in the molten state are shown in Table 7.1. Lanthanum (La), the lanthanide of lowest atomic number, and yttrium (Y), one of the most electropositive transition metals, are both members of a group consisting of 17 elements commonly labeled as the rare earth elements (REE's). The REE's containing the 3f valence lanthanides plus scandium (Sc) and Y are often found together in nature due to the similarities of their chemistry and atomic size in the 3+ valence state.

On the basis of the chemical similarity of REE's and lack of available data, the

Table 7.1: Selected properties for pure, molten La_2O_3 & Y_2O_3 near T_{fus}

	T_{fus} K	$\Delta_{fus}S^o$ J mol^{-1} K^{-1}	V_m cm^3 mol^{-1}	p_i^o Pa	σ Ω^{-1} cm^{-1}	$E_g(T=0\ \mathbf{K})$ eV
La_2O_3	2574 [1]	30.3 [1]	63.9 [2]	12.4 [3]		3.83 [4]
Y_2O_3	2712 [5], [6]	30.9 [6], [7]	51.1 [2]	1.2 [3]	18 [8]	4.45 [4]

CALPHAD community has predicted [6], [9] that the rare earth oxides (REO's) exhibit ideal mixing behavior in the liquid state. As described in §1.1.3, CALPHAD modeling of molten systems using ideal mixing entropy where thermodynamic data is limited is a common assumption. If the REO's were ideal, then the variation in chemical potential ($\mu_{R_2O_3}$) of component R_2O_3 (R=rare earth element) in a molten REO mixture would be given by

$$\mu_{R_2O_3} = \mu^o_{R_2O_3} + RT\ln(X_{R_2O_3})$$

where $\mu^o_{R_2O_3}$ is the standard chemical potential (standard state pure liquid R_2O_3 at temperature T, $p = 101,325$ Pa), and $X_{R_2O_3}$ is the mole fraction of R_2O_3 in the melt.

Therefore, for conditions where $X_{R_2O_3}$ and T are experimentally well-defined, determining $\mu_{R_2O_3}$ requires only an accurate description for $\mu^o_{R_2O_3}$. Fortunately, thermodynamic assessments for the binary subsystems La-O [6], [9], [10] and Y-O [6], [9], [11] and thermodynamic data for pure La_2O_3(l) and Y_2O_3(l) are available [1], [6], [7], [9]–[11], in part, due to interest from the solid oxide fuel cell and laser communities.

The high temperature, pseudo-binary cross-section for La_2O_3-Y_2O_3 optimized recently by Chen et al. [9] is shown in Figure 7-1. A close agreement was observed between the predicted [9] and measured liquidus phase boundaries of Lopato et al. [12] and Coutures et al. [13]. The La_2O_3-Y_2O_3 melt exhibits a depressed "lens"-like phase boundary with the solid H (Y_2O_3-rich) and X (La_2O_3-rich) phases, with no known miscibility gaps or congruently melting compounds. The liquidus temperature is reported to vary from T = 2480 to 2712 K, which compares favorably with the melting point of Ir (2719 K) [14].

Therefore, if the system La_2O_3-Y_2O_3 is proven to be ionic and the mixing behavior

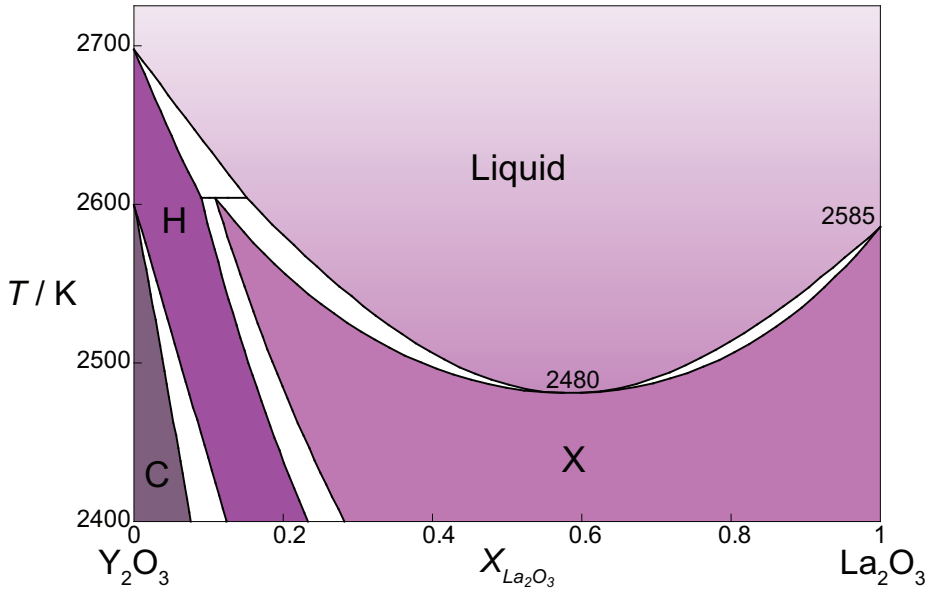

Figure 7-1: High-temperature region of the pseudo-binary La_2O_3-Y_2O_3 phase diagram, calculated via the recent thermodynamic assessment by Chen et al. [9] using FactSage [3]. Phases shown include the liquid and the high temperature solid solution phases (hexagonal H-phase and cubic X- and C-phases).

is indeed ideal, then the La_2O_3-Y_2O_3 system represents a model case for testing the method validated with Al_2O_3 as extended to a multicomponent solutions and further testing the hypothesis of this work.

7.2 Experimental

The experimental methods are very similar to those employed for the obtaining the results described in the previous chapter (§6) and Nakanishi et al. [15] (also available in Appendix C). Here, only relevant deviations in the experimental procedure are described.

Powders of La_2O_3 and Y_2O_3 (both $> 99.9\%$ purity, diameter $\varnothing < 10\mu$m, Alfa Aesar) were mixed to the compositions shown in Table 7.2 and formed into rods using the method described by Nakanishi et al. [15]. Ir wires were employed as electrodes with configurations described in the previous chapter §6. One composition of argon gas (UHP Ar, 99.999% Ar, $p_{O_2} = 1$ Pa, Airgas Inc.) was used for this study.

Electrochemical measurements were performed at a single TIF lamp power (tem-

Table 7.2: Electrolyte compositions & approximate temperatures investigated

$X_{La_2O_3}$	T_{liq}/ K	T / K
0	2712 [5], [6]	2737
0.2	2594 [12], [13]	2619
0.4	2523 [12], [13]	2548
0.6	2491 [12], [13]	2516
0.8	2507 [12], [13]	2532
1	2574 [1]	2599

perature), defined by the minimum power required for electrode insertion and maintaining a fully molten droplet, which was confirmed by EIS and OCP measurements. This temperature, presented in the third column of Table 7.2, was determined by adding an estimated 25 K superheat to either

1. T_{fus} from Table 7.1 for $X_{La_2O_3} = 0$ or 1, or

2. the average liquidus temperature (T_{liq}) at $X_{La_2O_3}$ using the experimental results of Lopato et al. [12] and Coutures et al. [13], rejecting those of Mizuno et al. [16].

The post-quenched, sectioned and polished droplets and electrodes were analyzed for composition using wavelength-dispersive X-ray spectroscopy (WDS). Here, WDS was preferred over EDS, the technique utilized in §6, due to overlap in the X-ray emission spectrum between Y (Lα = 1.924 keV) and Ir (Mα = 1.980 keV).

7.3 Results & discussion

7.3.1 Evidence for the electrolytic nature of molten La_2O_3-Y_2O_3

Electrolysis was performed on La_2O_3-Y_2O_3 droplets using three Ir electrodes. For all compositions investigated, bubbling was observed in the vicinity of the anode, which was confirmed to be due to oxygen gas by an oxygen sensor monitoring the furnace

exhaust. The droplet and electrodes were quenched after electrolysis by shutting off the TIF lamps for further analysis.

Post experimental analyses of polished cross-sections of the droplet and electrodes showed that the conditions of the RE and anode following electrolysis and for all electrodes prior to electrolysis were visually unchanged. However, small particles ($\varnothing < 1\ \mu$m) were observed in the electrolyte bulk. Exact compositions for the particles were difficult to determine by WDS given their small size. A similar observation for Ir particles in silicate melts at $T = 1823$ K has been made by Kim et al. [17]. For galvanostatic electrolyses performed at very large currents ($I = 3$ A, $j \approx 10$ A cm^{-2}) for short duration (60 s), the droplet surface in the vicinity of the anode was more vigorously perturbed by gas bubbles. Additionally, the post-quenched electrolyte was observed to be colored red-orange in the vicinity of the anode, but the Ir content was below the WDS detection limit and the shape of the Ir anode remained visually unchanged. These observations are likely explained by the anodic dissolution of Ir into the La_2O_3-Y_2O_3 melt at high current densities (≈ 30 A cm^{-2}). Furthermore, thermodynamic considerations for the formation of IrO_x gaseous species under such conditions suggest that their total partial pressure is quite low ($p_{IrO_x} < 100Pa$) [3]. Therefore, considering oxygen and IrO_x vapor species only, the fraction of faradaic current driving oxygen gas evolution is approximately $10^4 - 10^5$ times greater than that for Ir oxidation. Therefore, the concentrations of Ir in both the gas phase and melt at the anode were negligibly small.

Typical polished cross-sections for the cathode following potentiostatic electrolysis at cell potential difference $U > U^o$ (U^o defined previously in §5) are shown in Figure 7-2 versus melt composition ($X_{La_2O_3}$). For $X_{La_2O_3} = [0.2, 0.4, 0.6, 0.8]$, La and Y were observed to co-deposit. The cathodic deposit contained at least two metallic alloy phases compositionally characterized as follows:

1. One alloy phase was Ir-rich with contents of La and Y below the WDS detection limit (< 200 ppm);

2. A second alloy phase containing La-Y-Ir, with total REE content greater than

20 mol%.

The composition of the REE-containing alloy phase was further characterized according to the chemical formula $(La_zY_{1-z})_1Ir_x$. Parameter z quantifies the relative fraction of La to Y in the Ir alloy phase based on an average of at least five WDS point analyses; parameter x represents the minimum detected number of Ir atoms per REE atom. The variation of z and x versus $X_{La_2O_3}$ is shown in Figure 7-3. Selective deposition of La is observed for $X_{La_2O_3} > 0.2$.

Observations at macroscale (Figure 7-2a to 7-2f) and microscale (Figure 7-2g to 7-2l) reveal notable trends for the deposits summarized as follows:

1. The cathode was severely deformed for $X_{La_2O_3} = 0$, presumably deformed upon melting by Raleigh instability effects; for $X_{La_2O_3} \neq 0$, the cathode mostly retained its original geometry (i.e. cylindrical Ir wire, $\varnothing = 0.5$ mm).

2. For $X_{La_2O_3} \neq 1$, large cavities ($\varnothing \approx 100$ μm) were observed.

3. At the electrode-electrolyte interface, oxide inclusions ($\varnothing < 10$ μm) formed within the metallic deposit.

4. For $X_{La_2O_3} = 1$, La was not detected at the electrode center. For $X_{La_2O_3} \neq 1$, the internal bulk of the electrode contained the two alloy phases previously described. The La-Y-Ir phase with needle-like morphology was detected. The Ir-rich phase was characterized by fine ($\varnothing < 1$ μm), interconnected particles forming a web-like structure; the former REE phase appears to occur in between the Ir-rich web of particles.

These results confirm molten La_2O_3-Y_2O_3 decompose under an applied electric field. Oxygen gas bubbling was observed at the Ir anode for all $X_{La_2O_3}$ investigated. An Ir-rich alloy phase containing greater than 20 mol% REE was observed at the cathode. Furthermore, La and Y co-deposition was observed for $X_{La_2O_3} = [0.2, 0.4, 0.6, 0.8]$. Subsequently, the reactions occurring at the anode, cathode and RE were investigated further by ACV.

7.3.2 Electrochemical behavior of the anode, cathode & reference electrode

A typical ACV voltammogram for $X_{La_2O_3} = 0.8$ showing the cell voltage, first, second and third harmonics of the current response versus dc potential is presented in Figure 7-4. For positive potentials, the electrode labeled "anode" served as the WE. A faradaic event was observed at $E = E_A^*$ and corresponding with the half-cell reaction between oxide ions O^{2-} in the melt and oxygen gas $O_2(g)$ at $101,325$ Pa given by

$$O^{2-}(melt) = 2e^- + \frac{1}{2}O_2(g) \tag{7.1}$$

The following observations confirmed the correspondence between E_A^* and Reaction 7.1:

1. Oxygen bubbling in the vicinity of the anode was always observed and detected by an oxygen sensor on the furnace exhaust line concomitant with the anode attaining electrode potential $E > E_A^*$.

2. The similarity of peak-splitting features across 2nd and higher current harmonics obtained to that observed for an Ir anode in molten Al_2O_3 (compare $I_{2\omega}$ and $I_{3\omega}$ from Figure 7-4 with Figure 6-4).

3. the small concentrations of Ir observed in the post-quenched oxide melt and likely negligible presence in the gas phase at the anode

The features for the ACV voltammogram for an Ir anode were found to be consistent for all $X_{La_2O_3}$ investigated, permitting detection and measurement of the electrochemical reaction potential E_A^* coinciding with Reaction 7.1. Although not examined during this investigation, the variation of E_A^* with temperature and oxygen partial pressure in the furnace atmosphere is anticipated to be described, at least approximately, by Eq. 6.2.

For negative potentials, a faradaic event is observed at E_C^* with its own peak-splitting feature, as shown in Figure 7-4 for a distinct electrode labeled "cathode."

The corresponding half-cell reaction describing the co-reduction of rare earth ions R^{3+} to $\underline{R}$(l) (for R=La,Y) alloyed with Ir is given by:

$$R^{3+}(melt) + 3e^{-} = \underline{R}(l) \tag{7.2}$$

Here, the state of $\underline{R}$(l) is considered to be that of first formation of liquid Ir-La-Y alloy on the Ir cathode, i.e. the liquidus composition. The following evidence supports this assertion:

1. The similarity of obtained 2nd and higher current harmonic peak-splitting features to that observed for an Ir anode in molten Al_2O_3 (compare $I_{2\omega}$ and $I_{3\omega}$ shown in Figure 7-4 with those shown in Figure 6-4).

2. The typical cathodic products following electrolysis at $E < E_C^*$, shows formation of a complex deposit containing multiphase La-Y-Ir alloy with oxide inclusions.

3. Electrolysis at $E > E_C^*$ (less negative), shows no indication of REE-Ir alloy formation, with a content of REE in the Ir cathode below the detection limit of WDS.

4. With the limited thermodynamic data available [3], formation of rare earth suboxide gaseous species, are thermodynamically unfavorable to form by reduction at the cathode.

The features for the ACV voltammogram for an Ir cathode were found to be qualitatively consistent in shape for all $X_{La_2O_3}$ investigated, permitting detection and measurement of the electrochemical reaction potential E_C^* coinciding with Reaction 7.2. The variation of $I_{3\omega}$ is shown in Figure 7-5. Two peaks were consistently observed and the more negative of these two peaks was identified as E_C^*. The intensity normalized by geometric surface area was greatest for $X_{La_2O_3} = 0.2$ and decreased as $X_{La_2O_3} \to 1$.

Nevertheless, the results presented herein suggest that Reactions 7.1 and 7.2 coincide with signals observed during E_A^* and E_C^* measurement, resp.

7.3.3 Decomposition voltage measurements

Decomposition voltage measurements of U^o were pursued using an identical method to that described in §6.3.3 and detailed in §5. The results for U^o variation with $X_{La_2O_3}$ are presented in Figure 7-6. In practice, $U(E_C^*)$ was found to be greater than $U(E_A^*)$, when the cathode to anode area ratio ($A_{G,C}/A_{G,A}$) was greater than 1.5 for all $X_{La_2O_3}$ under the conditions investigated.

7.3.4 Thermodynamic analysis

The potential of the oxygen evolving anode (dynamic oxygen RE) in La_2O_3-Y_2O_3 was fixed during measurements of U^o assuming:

1. O_2(g) chemical potential (μ_{O_2}) variation is negligible due to mechanical equilibrium constraints (including surface tension effects) and low vapor pressure of the oxide melt, cf. 7.1, and other possible species (e.g. IrO_x).

2. O^{2-} chemical potential ($\mu_{O^{2-}}$) variation is negligible due to charge neutrality constraints and the negligibly small concentrations of Ir observed.

Oxide inclusions were observed in the cathode deposit following electrolysis near the electrode-electrolyte interface, as shown in Figure 7-2. This situation is possible in two foreseeable scenarios:

1. The alloy liquid exhibits high solubility for molecular O, which was transported to the cathode from the furnace atmosphere via the melt and/or via the triple-phase boundary (Ir cathode-molten droplet-furnace gas), and reacted with REE present in the alloy liquid to form the oxide inclusions during solidification upon quenching

2. During deposition, the electrolyte became entrapped in a "mushy" (both solid and liquid alloy phases present) cathode deposit

If the latter scenario was operating, then the ternary alloy liquid Ir-La-Y remains the relevant system for further thermodynamic analysis. However, if the former occurred, then the Ir-La-Y-O quaternary system becomes relevant and the interactions

between La-Y-O in the Ir solvent require further consideration in the thermodynamic analysis. Data for Ir-La-Y-O system, especially, the Ir-rich, high temperature equilibrium involving these species are not available at present [18]–[22]. However, in the limit of infinite dilution, the analysis for both scenarios reduce to the same thermodynamic formalism. Given that La, Y and O concentrations are expected to be small at the liquidus phase boundary, the behavior of these species are expected to be well-described by infinite dilution in an Ir liquid solvent.

For the pseudo-unary electrolytes (i.e. $X_{La_2O_3} = 0$ and 1), the thermodynamic analysis proceeds in a similar fashion to that described in §6.3.4. That is, U^o is the decomposition voltage for the overall reaction

$$R_2O_3(l) \rightarrow 2\underline{R}(l) + \frac{3}{2}O_2(g) \tag{7.3}$$

The corresponding Gibbs energy change for Reaction 7.3 may be computed via

$$\Delta_r G = 6FU^o = 2\mu_{\underline{R}(l)} + \frac{3}{2}\mu^o_{O_2} - \mu^o_{R_2O_3} \tag{7.4}$$

where $\mu^o_{O_2}$ and $\mu^o_{R_2O_3}$ are the standard chemical potentials of $O_2(g)$ (standard state $O_2(g)$ at 101,325 Pa and temperature T) and R_2O_3(l) (standard state pure liquid, at T and $p = 101,325$ Pa), resp., and $\mu_{\underline{R}(l)}$, or simply $\mu_{\underline{R}}$, is the chemical potential of R (=La,Y) at the liquidus composition of the R-Ir binary alloy.

For the electrolytes at intermediate compositions (i.e. $X_{La_2O_3} = 0.2, 0.4, 0.6, 0.8$), the analysis proceeds with the simplifying assumptions:

1. Given the relatively low concentrations of REE deposited in Ir and high concentrations of La and Y in the oxide phase, the variation in $\mu_{R_2O_3}$ is negligible (this topic is given more consideration in Appendix A)

2. The relative proportions of La and Y in the liquid Ir-La-Y alloy are hypothesized to be precisely that of parameter z shown in Figure 7-3, i.e. z observed in the quenched droplet following electrolysis at $U > U^o$ is equivalent to the relative proportions of La and Y near the cathode-electrolyte interface at $U^o = U(E^*_C)$

The reaction thermodynamics for the co-depositing species are herein treated separately. Similarly, U^o is the decomposition voltage for Reaction 7.3, and the corresponding Gibbs energy change may be computed via a similar relation to Eq. 7.4

$$\Delta_r G = 6FU^o = 2\mu_{\underline{R}} + \frac{3}{2}\mu^o_{O_2} - \mu_{R_2O_3} \tag{7.5}$$

where $\mu_{R_2O_3}$ is equivalent, under the given assumptions, to the equilibrium chemical potential of R_2O_3(l) in the bulk La_2O_3-Y_2O_3 melt. The variation of $\mu_{R_2O_3}$ with $X_{R_2O_3}$ is given by

$$\mu_{R_2O_3} = \mu^o_{R_2O_3} + RT\ln\gamma_{R_2O_3} + RT\ln X_{R_2O_3} \tag{7.6}$$

where $\gamma_{R_2O_3}$ is the activity coefficient for R_2O_3(l). Rearranging Eq. 7.5 and combining with Eq. 7.6 yields an expression for the partial molar excess Gibbs energy of R_2O_3(l)

$$G^E_{R_2O_3} \equiv RT\ln\gamma_{R_2O_3} = 2\mu_{\underline{R}} + \frac{3}{2}\mu^o_{O_2} - 6FU^o - \mu^o_{R_2O_3} - RT\ln X_{R_2O_3} \tag{7.7}$$

where U^o is provided in Figure 7-6 and $\mu^o_{O_2}$ is tabulated [23].

A number of optimized descriptions are available for $\mu^o_{La_2O_3}$ and $\mu^o_{Y_2O_3}$ [1], [6], [9]–[11], [24]. Chen et al. [9] incorporated the previous optimizations of La-O [10] and Y-O [11]. The description by Chen et al. [9] for $\mu^o_{Y_2O_3}$ was updated with the more recent measurements by Ushakov et al. [1] (data shown in Table 7.1).

Thermodynamic data for the Ir-La-Y system, especially in the Ir-rich high temperature portion of state variable space, is severely lacking [18]–[22]. Therefore, a thermodynamic model for $\mu_{\underline{R}}$ was developed using the following assumptions:

1. The standard states for all species in the liquid alloy phase are of their own pure liquids at T, $p = 101,325$ Pa

2. La and Y behave as infinitely dilute solutes in an Ir liquid solvent. La and Y chemical interactions with themselves in the liquid are negligible in comparison to interactions with the Ir solvent.

3. The solubility of La and Y in Ir(s) is negligibly small. This assumption is sup-

ported by experimental observations of Y solubility in Ir (< 0.1 at%, detection limit of field emission electron probe micro-analysis equipment employed) following annealing at 1973 K for 100 h. No similar studies on La-Ir have been reported to the author's knowledge.

4. The composition of the liquidus for the R-Ir pseudo-binary (X_{Ir}^{l}) is described by the expression [25]

$$\ln(X_{Ir}^{l}) = -\frac{\Delta_{fus}H_{Ir}^{o}}{R}\left(\frac{1}{T} - \frac{1}{T_{fus,Ir}}\right) \tag{7.8}$$

where $\Delta_{fus}H_{Ir}^{o}$ ($= 41.14$ kJ mol^{-1} [26]) and $T_{fus,Ir}$ (discussed below) are the melting enthalpy and temperature, resp., for pure Ir.

5. The partial molar excess Gibbs energy of La and Y in Ir obeys the expression

$$G_i^E = RT\ln\gamma_i^{\infty} = \Delta H_i^{\infty} - T\Delta S_i^{E,\infty} \tag{7.9}$$

where γ_i^{∞}, ΔH_i^{∞} and $\Delta S_i^{E,\infty}$ are the Henrian coefficient and partial molar excess enthalpy and entropy for species i at infinite dilution in Ir liquid, resp.

6. The semi-empirical Miedema model [27] accurately describes ΔH_i^{∞} for $i = (La, Y)$ in liquid Ir(l) ($\Delta H_{La}^{\infty} = -230$ kJ mol^{-1} and $\Delta H_{Y}^{\infty} = -242$ kJ mol^{-1})

7. $\Delta S_i^{E,\infty} = 0$

The preceding assumptions permit determination of $\mu_{\underline{R}}$ for a given T according to

$$\mu_{\underline{R}} = \mu_R^{o} + RT\ln X_R + RT\ln\gamma_R^{\infty} \tag{7.10}$$

Where $RT\ln\gamma_R^{\infty}$ is given by Eq. 7.9; $X_{La} = z(1 - X_{Ir}^{l})$ and $X_Y = (1 - z)(1 - X_{Ir}^{l})$ where X_{Ir}^{l} is given by Eq. 7.8.

As described previously, the temperatures for each composition are based upon a 25 K superheat above an average of the experimentally determined La_2O_3-Y_2O_3 liquidus temperatures [12], [13] (shown in Table 7.2). The accepted value for $T_{fus,Ir} =$

2719K [14], [28] was found to conflict with the expected operating temperature for pure Y_2O_3 ($T = T_{fus,Y_2O_3} + 25$ K $= 2737$ K), as no melting was observed during contact between Ir electrodes (except for the polarized cathode during electrolysis) and the pure, molten Y_2O_3 droplet. Henning et al. [28] reported the most recent measurement of $T_{fus,Ir}$ in 1933. T_{fus,Y_2O_3} was determined by an international collaboration involving ten laboratories and was found to be invariant with atmosphere [5]. Given the accuracy of the recently reported measurements for La_2O_3 [1], the assessed data for $\mu^o_{La_2O_3}$ combined the present results was used to determine $T_{fus,Ir}$. An agreement between tabulated and measured $\mu^o_{La_2O_3}$ was found for $T_{fus,Ir} = 2769$ K, which is 50 K above the value reported by Henning et al. [28]. Perhaps, low purity specimens employed by [28] contributed to the discrepancy.

The results for $RT \ln \gamma_{R_2O_3}$ variation with $X_{La_2O_3}$ using Eqs. 7.10 and 7.7 are presented in Figure 7-7. For $X_{La_2O_3} = 0$ and 1, Figure 7-7 shows the difference between measured and assessed molar Gibbs energies for the pure components ($\mu^o_{i,meas.} - \mu^o_{i,tab.}$). The measured $\mu^o_{Y_2O_3}$ was approximately 50 kJ mol^{-1} higher than the assessed value by Chen et al [9]. The result for $\mu^o_{Y_2O_3}$ was very sensitive to $T_{fus,Ir}$, given the close proximity of the operating temperature and form of Eq. 7.8. A more accurate determination of $T_{fus,Ir}$ and development of a method for in situ measurement of absolute temperature, would improve interpretation of the results for $\mu^o_{La_2O_3}$ and $\mu^o_{Y_2O_3}$.

Despite the large errors for some data points and difficulty repeating measurements at $X_{La_2O_3} = 0.4$, the trend for all $X_{La_2O_3}$ clearly indicates that molten La_2O_3-Y_2O_3 is not ideal, with negative deviation from ideal mixing under the previous assumptions. For comparison, dashed lines show G^E_i for a regular solution with model parameter $\omega_{La_2O_3,Y_2O_3} = -50$ kJ mol^{-1}. This result contradicts previous predictions from the CALPHAD community for molten REO ideality [6], [9], [29]. Chen et al. [9] and Zinkevich [6] assumed ideal mixing without further justification and were able to reproduce the liquidus phase boundary within the limits of experimental error. An empirical correlation for common-cation ionic melts, which accounts for the effects of cation charge, radius and polarizability on the excess enthalpy and entropy of mixing in a four-parameter Redlich-Kister expansion, was proposed van der Kemp et al. [29],

[30]. Adapting their proposed expression (data for La^{3+} and Y^{3+} polarizabilities and radii taken from [31]) predicts that molten La_2O_3-Y_2O_3 exhibits only slight negative deviation from ideal mixing (e.g. at $X_{La_2O_3} = 0.2$, $G^E_{La_2O_3} = -0.253$ kJ mol^{-1}).

Before drawing further conclusions about REO mixing behavior, the following observations and assumptions are worth further discussion:

- postulated thermodynamic model for liquid (La-Y-Ir) metal alloy
- presence of oxide inclusions in cathode deposit
- Ir anode stability
- electronic conductivity

La and Y were assumed to behave as infinitely dilute solutes. At the minimum temperature investigated ($T \approx 2516$ K), the liquidus composition approaches $X_R \approx 0.16$ (assuming Eq. 7.8 is valid) which brings into question the assumption of Henrian behavior of La-Y as solutes for the lower melting intermediate composition. As the concentration for La and Y are increased, the activity coefficient (γ_R) is expected to increase towards unity. Therefore, a comparison with Eqs. 7.10 and 7.7 reveals that $G^E_{R_2O_3}$ is expected to increase (become more positive) at the intermediate concentrations as $RT \ln \frac{\gamma_R}{\gamma_R^\infty}$.

Additionally, the excess entropy at infinite dilution ($\Delta S_i^{E,\infty}$) was assumed to be negligibly small for the La-Ir-Y liquid alloy. At UHT, even minor entropic effects contribute significantly to the Gibbs energy, possibly invalidating this assumption. The central atom model and its modifications [32]–[34] predict $\Delta S_i^{E,\infty} = \frac{\Delta H_i^\infty}{\tau}$, where τ is an empirical constant with a value of 2500 ± 1000 K for binary substitutional alloys [32]. Generally, $\Delta S_i^{E,\infty}$ and ΔH_i^∞ are usually observed to share sign. Therefore, for the strong REE-Ir interactions present ($\Delta H_i^\infty \ll 0$), a non-negligible $-T\Delta S_i^{E,\infty}$ contribution to $\mu_{\underline{R}}$ would effectively increase $G^E_{R_2O_3}$ at all compositions and most significantly near the end-member compositions where operating temperature is greatest. However, previous semi-empirical correlations [32]–[34] do not appear to include data for interactions between platinum group metals (Ir, Pt, etc.) and Group III metals

(Sc, Y, La, etc.), which tend to form very stable intermetallic compounds with relatively small formation entropies [35]. Therefore, the present assumption $\Delta S_i^{E,\infty} = 0$ appears justified given the present data available.

Nevertheless, an improved description of the La-Y-Ir system (i.e. $T_{fus,Ir}$, description for the ternary liquidus phase boundary, activity coefficients for La and Y in Ir-rich liquid alloy) would significantly benefit interpretation of the present results.

The presence of dissolved molecular oxygen in the alloy liquid was neglected in the preceding thermodynamic analysis. The presence of oxide inclusions in the deposit near the electrolyte indicates that $\underline{O}$ was likely present at non-negligible concentrations in liquid alloy. The results for parameter z were obtained at the center of the electrode far away from the electrolyte and oxide inclusions in an effort to minimize the influence of the preferential back reaction between $\underline{Y}$ and $\underline{O}$ (versus $\underline{La}$ and $\underline{O}$) to form Y_2O_3 on the observed z. If this were the case, it would increase parameter z, which would in turn increase (make more positive) $\mu_{\underline{La}}$ and $G^E_{La_2O_3}$ and decrease $\mu_{\underline{Y}}$ and $G^E_{Y_2O_3}$ at a given composition. Therefore, interactions of Y and La with oxygen could account for the relative spacing between $G^E_{La_2O_3}$ and $G^E_{Y_2O_3}$ values, which interestingly is more predominant at low $X_{La_2O_3}$ (higher Y content in the deposit). Nevertheless, this feature could be accounted for with a suitable model accounting for the influence of back reaction on measurements of z or employing methods that limit the back reaction with $\underline{O}$ (e.g. faster quench rate or reduce $\underline{O}$ concentration in cathode by redoing measurements in more reducing atmosphere, i.e. lower oxygen partial pressure).

Anodic dissolution of Ir was observed. The presence of Ir ions in the melt may have influenced the activity of oxide ions in the melt at the surface of the anode, thus altering the inner potential of the anode during measurement of U^o. Though given the small concentration of Ir in the electrolyte, this was assumed to have negligible influence on the results. Given the remarkably close agreement between measured and tabulated data for $\mu^o_{La_2O_3}$ and $\mu^o_{Y_2O_3}$ at high temperature and low concentrations observed for Ir in the electrolyte this feature is not anticipated to have significant influence on the results. Nevertheless, Ir solubility is expected to decrease with decre-

asing temperature, for which $\mu_{O^{2-}}$ increases, ϕ_A^* decreases via an analogous expression to Eq. 5.4 for Reaction 7.1, and U^o decreases. Therefore, under these circumstances, $G^E_{R_2O_3}$ would become less negative. Therefore, the observed deviation from ideality for the REO melt becomes *less* negative if Ir oxidation does indeed influence the potential of the anode during oxygen evolution, contrary to the present observations. Nevertheless, further investigation of Ir as an inert anode (i.e. studies in different temperatures and oxygen partial pressures) may yield further insight for the significance of this effect. Nevertheless, it is considered to be negligible and would not explain the contradiction for REO ideality.

Though not studied directly during this investigation, the presence of electronic conductivity may have influenced the results for U^o due to electronic depolarization. An increase in electronic conductivity is expected to decrease U^o, which would make $G^E_{R_2O_3}$ more positive. The results for $I_{3\omega}$ presented in Figure 7-5 show the intensity of signals increase to a maximum at $X_{La_2O_3} = 0.2$ dropping off to similar intensities for $X_{La_2O_3} = 0, 0.4$ and steadily decreasing for increasing $X_{La_2O_3} = 0.6, 0.8, 1$. If electronic depolarization follows a similar behavior for U^o depolarization, than $G^E_{R_2O_3}$ will accordingly increase with electronic depolarization. An investigation into electronic conductivity in La_2O_3-Y_2O_3 coupled with a model for accounting for electronic conductivity in the decomposition voltage measurement would inform the significance of electronic conductivity. Given that electrolytic decomposition was observed and the apparent electronic conductivity observed contradicts the agreement with tabulated data for $\mu^o_{La_2O_3}$ and $\mu^o_{Y_2O_3}$, this feature is not expected to contribute significantly.

7.4 Summary

For the first time, La_2O_3-Y_2O_3 were electrolytically decomposed using Ir wires, confirming the electrolytic nature for these melts. Oxygen gas evolution was observed at the anode and La and Y were observed to co-deposit for the La_2O_3-Y_2O_3 mixtures investigated. The selective extraction of La was observed for $X_{La_2O_3} > 0.2$. Post-experiment observations indicate a liquid alloy phase forms at the cathode surface for

$U > U(E_C^*)$.

The method for decomposition voltage measurement described in §5 was extended to the pseudo-binary system La_2O_3-Y_2O_3. The results indicate that molten La_2O_3-Y_2O_3 is not an ideal mixture, contradicting previous predictions from the CALPHAD community. Further considerations suggest that the present thermodynamic analysis would benefit from:

- an improved thermodynamic model for the metallic alloy La-Y-Ir, taking into account the non-dilute mixing behavior of La and Y
- a means of eliminating or accounting for the back reaction between Y and La and dissolved oxygen in the cathode to improve reliability of parameter z
- an investigation of electronic conductivity versus La_2O_3-Y_2O_3

An improved thermodynamic model and removal of the influence of dissolved oxygen could explain the discrepancies between the measured data and those predicted by CALPHAD for La_2O_3-Y_2O_3. However, given the observed selective extraction La from La_2O_3-Y_2O_3, ideal mixing for molten La_2O_3-Y_2O_3 appears to be inaccurate. Electronic conductivity is not expected to contribute significantly given the close agreement observed for $\mu^o_{La_2O_3}$ and $\mu^o_{Y_2O_3}$ with tabulated data. However, addressing all three of these contributions is expected to significantly improve the accuracy and reliability of decomposition voltage measurement analysis for La_2O_3-Y_2O_3.

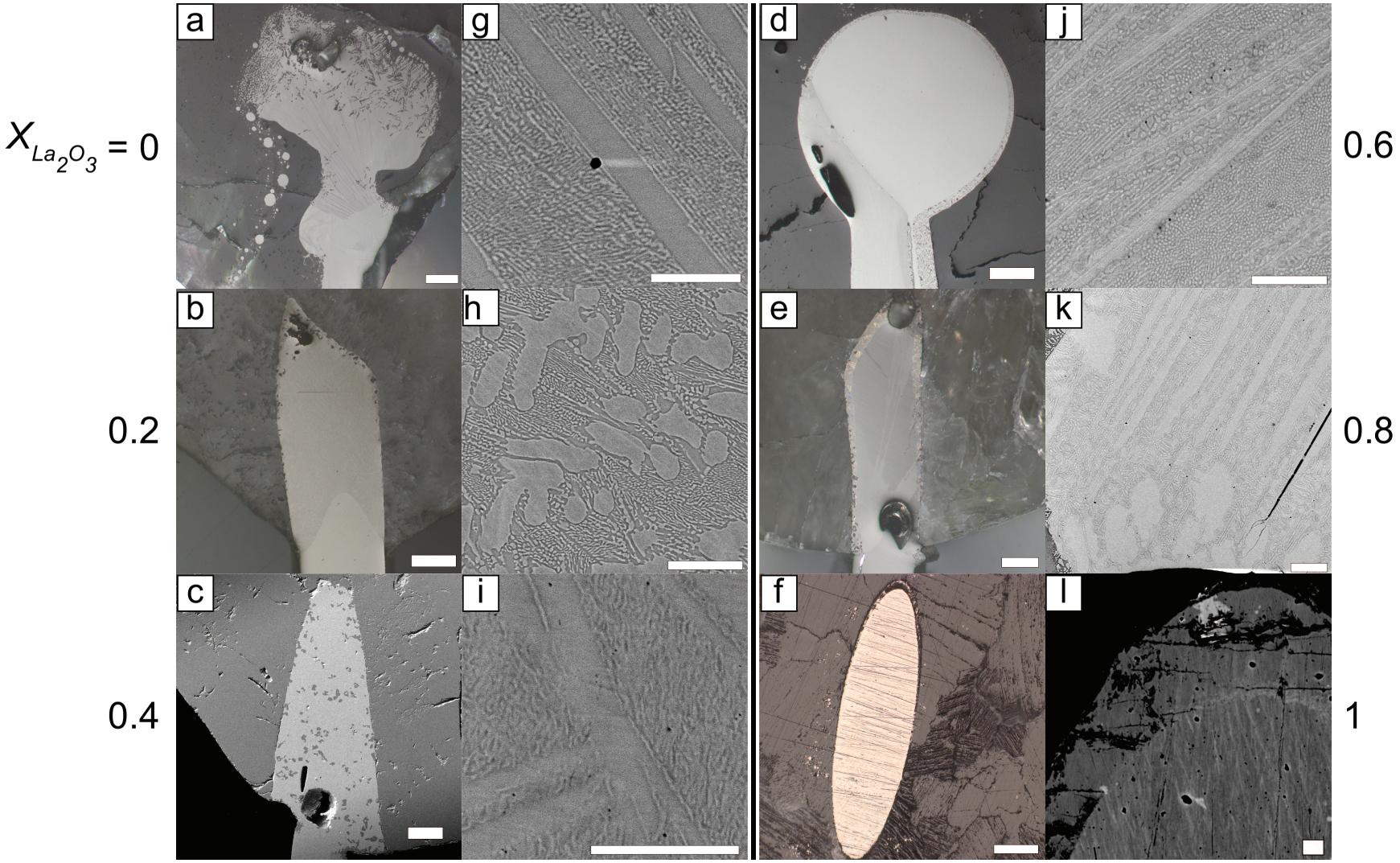

Figure 7-2: Micrographs of quenched cathode and droplet following potentiostatic electrolysis at cell potential $U > U^o$ (U^o defined previously in §5) versus melt composition. Droplet quenched after 60 s duration of current flow. (a)-(b), (d)-(f) optical micrographs and (c) secondary electron image of cathode in electrolyte, (a)-(f) scale bar 200 μm; (g)-(l) BSE images of cathode deposit at higher magnification, (g)-(l) scale bar 10 μm.

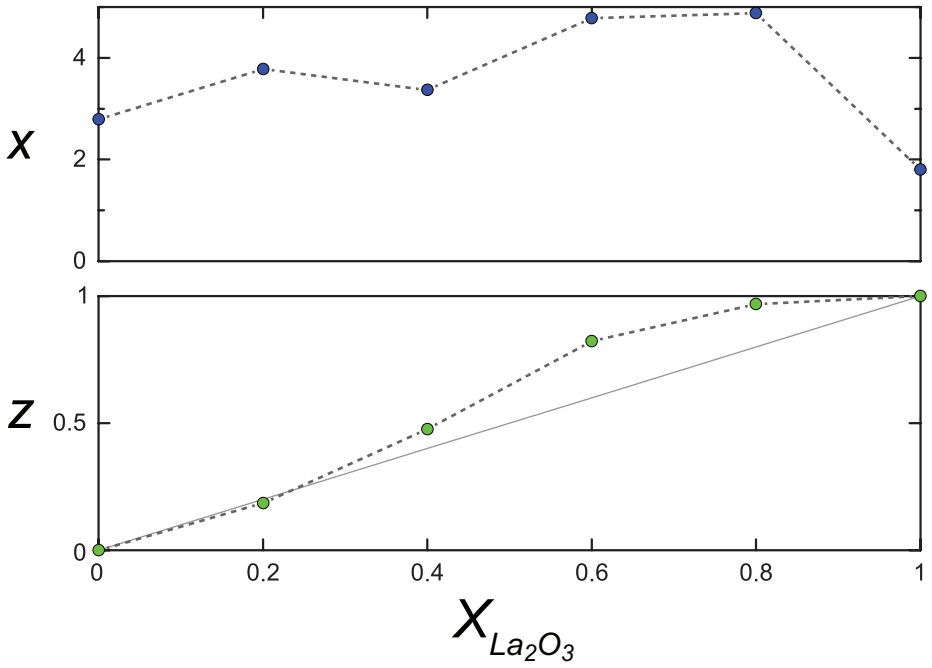

Figure 7-3: Variation of cathode deposit composition versus $X_{La_2O_3}$. The composition parameters x and z are defined according to the chemical formula $(La_zY_{1-z})Ir_x$. x is the minimum and z is an average (uncertainty $1\sigma < 0.01$) of five WDS point analyses.

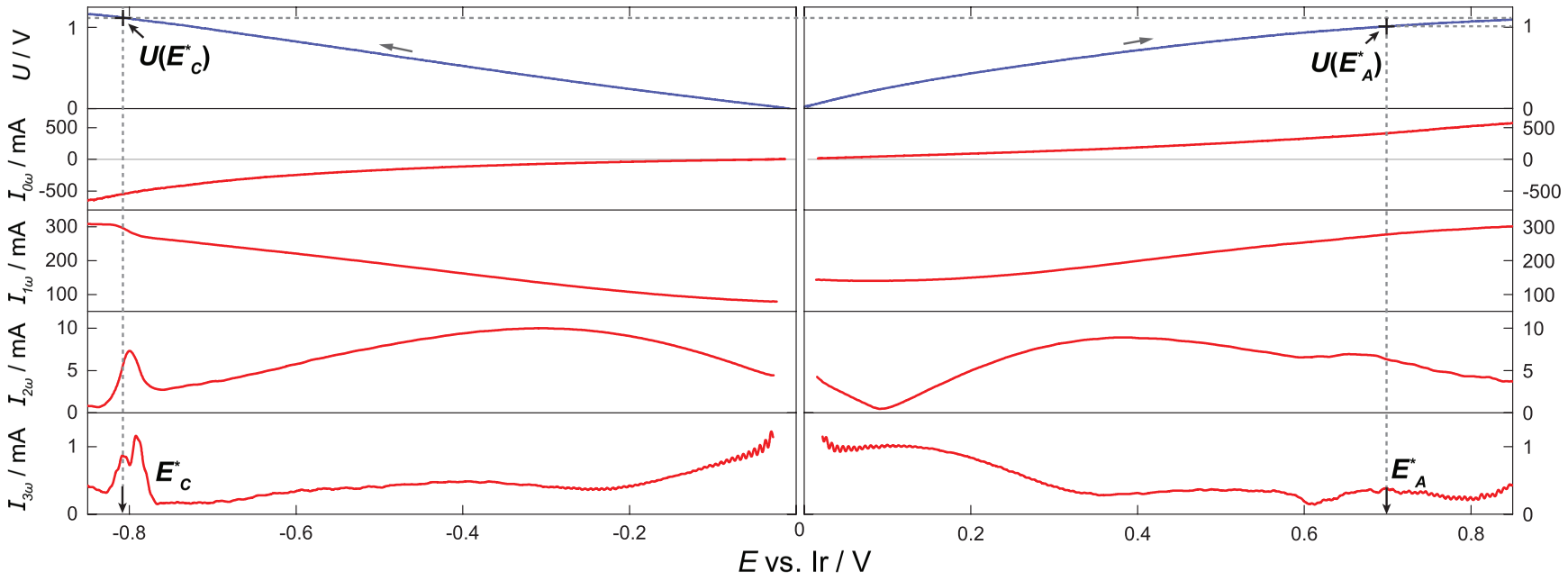

Figure 7-4: From top to bottom panel, dc component of cell voltage and dc, first, second and third harmonic current responses obtained during ACV measurements on an Ir WE in $X_{La_2O_3} = 0.8$. $E < 0$ corresponds to cathode polarization study (cathode geometric surface area $A_{G,C} = 0.024$ cm^2, applied dc potential scan limits -0.001 to -0.9 V vs. Ir); while $E > 0$ is an anodic polarization study (anode $A_{G,A} = 0.063$ cm^2, $+0.001$ to $+0.9$ V vs. Ir). For both, $E_{ac} = 150$ mV, $f = 23$ Hz, $\nu = 20$ mV s^{-1}. U was corrected for ohmic drop; E was not corrected for ohmic drop here to clarify interpretation; $R_u(E = E_C^*) = 0.50\ \Omega$ and $R_u(E = E_A^*) = 0.47\ \Omega$. The quantities E_A^*, E_C^*, $U(E_A^*)$ and $U(E_C^*)$ are described in the text.

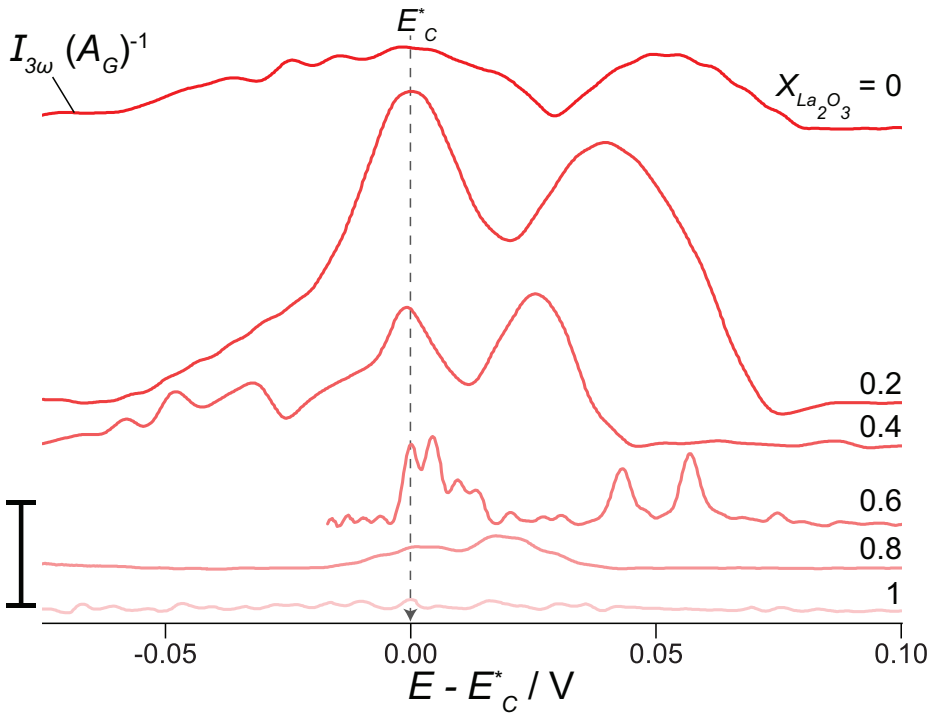

Figure 7-5: Variation of third harmonic of current for the ACV measurements on the Ir in La_2O_3-Y_2O_3 cathode normalized by cathode geometric surface area versus $E-E^*_C$ (y-axis scale bar 50 mA cm^{-2}); signals for each $X_{La_2O_3}$ are offset arbitrarily along y-axis for clarity. For all: $E_{ac} = 150$ mV, $f = 23$ Hz and $\nu = 20$ mV s^{-1}, negative-going scan. Again, E was not corrected for ohmic drop here to clarify interpretation.

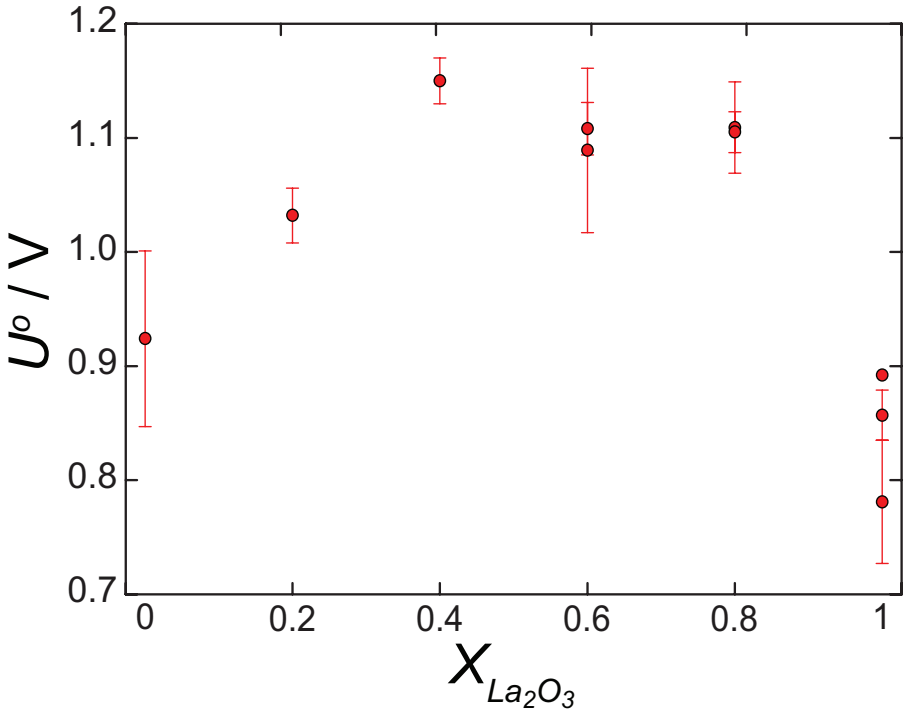

Figure 7-6: Variation of U^o versus $X_{La_2O_3}$.

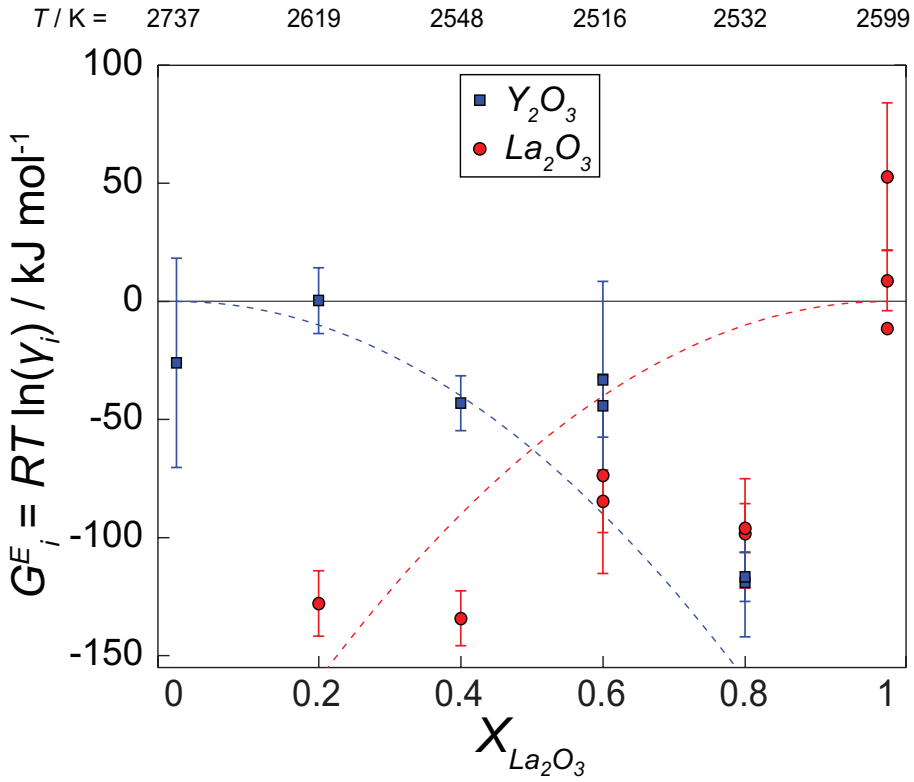

Figure 7-7: Variation of the partial molar excess Gibbs energy (G_i^E) for $i = \mathrm{La_2O_3}$ (red circles), $\mathrm{Y_2O_3}$ (blue squares) versus $X_{La_2O_3}$ for the pseudo-binary $\mathrm{La_2O_3}$-$\mathrm{Y_2O_3}$ liquid phase (standard state pure liquid $\mathrm{La_2O_3}$ or $\mathrm{Y_2O_3}$ at temperature T). Dashed lines correspond to G_i^E for a hypothetical regular solution with model parameter $\omega_{ij} = -50$ kJ mol^{-1}. For $X_{La_2O_3} = 0$ and 1, G_i^E represents the difference between measured and assessed molar Gibbs energies for the pure components ($\mu^o_{i,meas.} - \mu^o_{i,tab.}$).

References

[1] S. V. Ushakov and A. Navrotsky, "Direct measurements of fusion and phase transition enthalpies in lanthanum oxide," *J. Mater. Res.*, vol. 26, no. 7, pp. 845–847, 2011.

[2] B. Granier and S. Heurtault, "Density of liquid rare-earth sesquioxides," *J. Am. Ceram. Soc.*, vol. 71, no. 11, pp. 466–468, 1988.

[3] C. W. Bale, E. Bélisle, P. Chartrand, S. A. Decterov, G. Eriksson, A. Gheribi, K. Hack, I. H. Jung, Y. B. Kang, J. Melançon, A. D. Pelton, S. Petersen, C. Robelin., J. Sangster, and M.-A. V. Ende, "FactSage thermochemical software and databases, 2015-2016," *Calphad*, vol. 54, pp. 35–53, 2016.

[4] A. Jain, S. P. Ong, G. Hautier, W. Chen, S. Richards, William Davidson Dacek, S. Cholia, D. Gunter, D. Skinner, G. Ceder, and K. A. Persson, "The Materials Project: A materials genome approach to accelerating materials innovation," *APL Mater.*, vol. 1, no. 1, p. 011 002, 2013.

[5] J. Hlavac, "Melting temperatures of refractory oxides: Part I," *Pure Appl. Chem.*, vol. 54, no. 3, pp. 681–688, 1982.

[6] M. Zinkevich, "Thermodynamics of rare earth sesquioxides," *Prog. Mater. Sci.*, vol. 52, no. 4, pp. 597–647, 2007.

[7] E. E. Shpil'rain, D. N. Kagan, L. S. Barkhatov, and V. V. Koroleve, "Measurement of the enthalpy of solid and liquid phases of yttria," *High Temp. - High Press.*, vol. 8, pp. 183–186, 1976.

[8] E. E. Shpil'rain, D. N. Kagan, L. S. Barkhatov, and L. I. Zhmakin, "Electrical conductivity of yttrium and scandium oxides," *Rev. Int. Hautes Temper. Refract.*, vol. 16, no. 3, pp. 233–236, 1979.

[9] M. Chen, B. Hallstedt, and L. J. Gauckler, "CALPHAD modeling of the La_2O_3-Y_2O_3 system," *Calphad*, vol. 29, no. 2, pp. 103–113, 2005.

[10] A. N. Grundy, B. Hallstedt, and L. J. Gauckler, "Thermodynamic assessment of the lanthanum-oxygen system," *J. Phase Equilibria*, vol. 22, no. 2, pp. 105–113, 2001.

[11] V. Swamy, H. J. Seifert, and F. Aldinger, "Thermodynamic properties of Y_2O_3 phases and the yttrium-oxygen phase diagram," *J. Alloys Compd.*, vol. 269, no. 1-2, pp. 201–207, 1998.

[12] L. Lopato, B. S. Nigmanov, A. V. Schevchenko, and Z. A. Zaitseva, "Interaction between lanthanum oxide and yttrium oxide (translation)," *Neorg. Mater.*, vol. 22, no. 5, pp. 771–774, 1984.

[13] J. Coutures, A. Rouanet, R. Verges, and M. Foex, "Etude a haute temperature des systemes formes par le sesquioxyde de lanthane et les sesquioxydes de lanthanides. I. Diagrammes de phases ($1400^oC < T < T_{Liquide}$)," *J. Solid State Chem.*, vol. 17, pp. 171–182, 1976.

[14] R. E. Bedford, G. Bonnier, H. Maas, and F. Pavese, "Recommended values of temperature on the International Temperature Scale of 1990 for a selected set of secondary reference points," *Metrologia*, vol. 33, pp. 133–154, 1996.

[15] B. R. Nakanishi and A. Allanore, "Electrochemical study of a pendant molten alumina droplet and its application for thermodynamic property measurements of Al-Ir," *J. Electrochem. Soc.*, vol. 164, no. 13, E460, 2017.

[16] M. Mizuno, A. Rouanet, T. Yamada, and T. Noguchi, "Phase diagram of the system La_2O_3-Y_2O_3 at high temperatures," *Yogyo-Kyokai-Shi*, vol. 84, no. 7, pp. 342–348, 1976.

[17] H. Kim, J. Paramore, A. Allanore, and D. R. Sadoway, "Stability of iridium anode in molten oxide electrolysis for ironmaking: influence of slag basicity," *ECS Trans.*, vol. 33, no. 7, pp. 219–230, 2010.

[18] H. Okamoto, "The Ir-La (iridium-lanthanum) system," *J. Phase Equilibria*, vol. 12, no. 5, pp. 565–567, 1991.

[19] ——, "The Ir-Y (iridium-yttrium) system," *Phase Diagr. Eval.*, vol. 13, no. 6, pp. 651–653, 1992.

[20] K. T. Jacob, T. H. Okabe, T. Uda, and Y. Waseda, "Solid-state cells with buffer electrodes for accurate thermodynamic measurements: System Nd-Ir-O," *Electrochim. Acta*, vol. 45, no. 12, pp. 1963–1971, 2000.

[21] N. Sekido, H. Murakami, and Y. Yamabe-Mitarai, "Phase equilibria and oxidation behavior of Ir-rich Ir-Y binary alloys," *J. Alloys Compd.*, vol. 476, no. 1-2, pp. 107–112, 2009.

[22] H. Okamoto, "Supplemental literature review of binary phase diagrams: Ag-Nd, Ag-Zr, Al-Nb, B-Re, B-Si, In-Pt, Ir-Y, Na-Si, Na-Zn, Nb-P, Nd-Pt, and Th-Zr," *J. Phase Equilibria Diffus.*, vol. 35, no. 5, pp. 636–648, 2014.

[23] D. R. Stull and H. Prophet, "JANAF Thermochemical Tables," *J. Phys. Chem. Ref. Data*, 1985.

[24] P. Wu and A. D. Pelton, "Coupled thermodynamic phase diagram assessment of the rare earth oxide aluminum oxide binary systems," *J. Alloys Compd.*, vol. 179, pp. 259–287, 1992.

[25] C. H. P. Lupis, *Chemical Thermodynamics of Materials*. New York: North-Holland, 1983, p. 581.

[26] A. T. Dinsdale, "SGTE data for pure elements," *Calphad*, vol. 15, no. 4, pp. 317–425, 1991.

[27] F. R. de Boer, R. Boom, W. C. M. Mattens, A. R. Miedema, and A. K. Niessen, *Cohesion in Metals: Transition Metal Alloys*, F. R. de Boer and D. G. Pettifor, Eds. New York: North-Holland, 1988, p. 758.

[28] F. Henning and H. T. Wensel, "The freezing point of iridium," *Bur. Stand. J. Res.*, vol. 10, no. 6, pp. 809–821, 1933.

[29] W. J. M. van der Kemp, J. G. Blok, P. van der Linde, H. A. J. Oonk, A. Schuijff, and M. L. Verdonk, "Binary alkaline earth oxide mixtures: Estimation of the excess thermodynamic properties and calculation of the phase diagrams," *Calphad*, vol. 18, no. 3, pp. 255–267, 1994.

[30] W. J. M. van der Kemp, P. R. van der Linde, J. G. Blok, and H. A. J. Oonk, "The melting properties of the earth alkaline oxides; thermodynamic analysis of the binary system (1-X)MgO + XCaO," *Calphad*, vol. 17, no. 1, pp. 57–65, 1993.

[31] R. D. Shannon and R. X. Fischer, "Empirical electronic polarizabilities in oxides, hydroxides, oxyfluorides, and oxychlorides," *Phys. Rev. B - Condens. Matter Mater. Phys.*, vol. 73, pp. 1–28, 2006.

[32] C. H. P. Lupis and J. F. Elliott, "Prediction of enthalpy and entropy interaction coefficients by the 'central atoms' theory," *Acta Met.*, vol. 15, no. 2, p. 265, 1967.

[33] T. Tanaka, N. A. Gokcen, and Z. Morita, "Relationship between enthalpy of mixing and excess entropy in liquid binary alloys," *Zeitschrift fuer Met.*, vol. 81, no. 1, pp. 49–54, 1990.

[34] T. Tanaka, N. A. Gokcen, and Z.-i. Morita, "Relationship between partial enthalpy of mixing and partial excess entropy of solute elements in infinitely dilute solutions of liquid binary alloys," *Zeitschrift für Met.*, vol. 81, no. 5, pp. 349–353, 1990.

[35] L. Brewer and P. R. Wengert, "Transition metal alloys of extraordinary stability; An example of generalized Lewis-acid-base interactions in metallic systems," *Metall. Trans.*, vol. 4, no. 1, pp. 83–104, 1973.

Chapter 8

Discussion

The electrolytic cell method and its application for Gibbs energy measurement in high temperature, concentrated ionic melts was investigated. Previous challenges related primarily to signal interpretation during decomposition voltage measurement have hindered determination of Gibbs energy. An electrolytic cell method was proposed in §5 utilizing the sensitivity of ACV for precise correlation of electrode potentials and states of the electroactive species. This capability was verified by investigating the faradaic reactions on various substrates in NaCl-KCl in §3.

A novel, containerless approach for electrochemical study of high temperature, reactive electrolytes in a molten pendant droplet was described in §4. Using said approach, the pseudo-unary melts of pure Al_2O_3, Y_2O_3 and La_2O_3 and mixtures of La_2O_3-Y_2O_3 were electrolytically decomposed for the first time using Ir electrodes. In situ, visual observation and detection of oxygen gas evolution during electrolysis and post-experimental observations of liquid metal alloy formation at the cathode confirm the electrolytic nature of these oxide melts.

Validation of the electrolytic cell method in molten Al_2O_3 was described in §6. Systematic investigation of the half-cell reactions corresponding to oxygen evolution and aluminum deposition revealed their electrochemical nature. Measurements of the chemical potential and partial molar entropy of aluminum in an iridium-rich, binary alloy liquid were obtained in close agreement with previous predictions. A significant error for entropy measurements persisted originating from difficulties for determining

absolute temperature. Nevertheless, these results provided evidence for the validity of the hypothesis.

Extension of the method to the pseudo-binary system molten La_2O_3-Y_2O_3. The results revealed selective extraction of La and the non-ideal mixing behavior of molten La_2O_3-Y_2O_3, contradicting previous predictions. However, data interpretation in multicomponent electrolyte compositions were challenged primarily by a lack of thermodynamic data for the attendant alloy system and influence of dissolved oxygen on the observed alloy composition.

Herein, results from the present work are discussed further in the context of the hypothesis. Particular attention is given to those situations where the proposed method fails under the current hypothesis.

8.1 Stability of Ir in Al_2O_3, Y_2O_3 & La_2O_3

Ir exhibited remarkable stability in the UHT melts of Al_2O_3, Y_2O_3 and La_2O_3. The anodic dissolution of Ir was not observed for the conditions employed with Al_2O_3. In La_2O_3-Y_2O_3, Ir dissolution was observed only at very high current densities ($j \approx 10$ A cm^{-2}) by the change in apparent color of the electrolyte in the anode compartment. Nevertheless, Ir concentration in the La_2O_3-Y_2O_3 melt was below the WDS detection limit and the geometric shape of the electrode remained visually unchanged during polarization. This stability was exploited for decomposition voltage measurements utilizing oxygen evolution on Ir as a polarized dynamic reference electrode in these UHT melts. As applied to other melts and conditions, the stability of the anode and its role in the success of the present method are emphasized.

8.2 On the relationship between ACV signals & nature of the faradaic reactions observed

Qualitative connections, transcending temperature and materials system, were observed for the harmonic current responses obtained by ACV measurements in NaCl-KCl,

Al_2O_3, and La_2O_3-Y_2O_3. Chlorine gas evolution on graphite (from NaCl-KCl) and oxygen gas evolution on Ir (from Al_2O_3, Y_2O_3 and La_2O_3) exhibited remarkably similar features in the second and higher harmonics at the potential labeled E_A^*, as presented in Figure 8-1. A similar qualitative connection was observed for those reactions involving liquid alloy formation on a reactive cathode in the vicinity of potential labeled E_C^*: Na-K co-deposition on Au in NaCl-KCl and Al, Y and La deposition on Ir from their respective oxide melts, as presented in Figure 8-2.

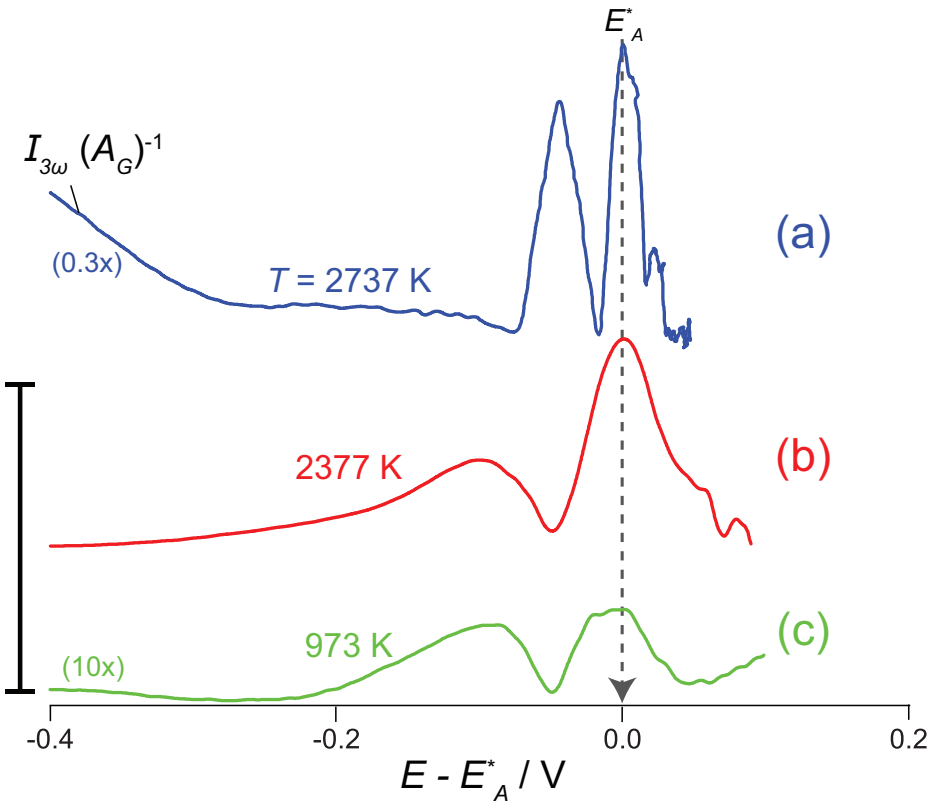

Figure 8-1: Comparison of $I_{3\omega}$ for gas evolution occurring on an *anode* composed of: Ir (oxygen evolution) in Y_2O_3 (a), Ir (oxygen evolution) in Al_2O_3 (b) and graphite (chlorine evolution) in NaCl-KCl (c); y-axis scale bar 10 mA cm^{-2}. The parameters employed for electrochemical measurements are described in the corresponding chapters for these electrolytes.

Furthermore, the features of the ACV responses exhibited qualitative differences for the electrolytes investigated with respect to the transition in product species' chemical state (solid, liquid, gas), as seen comparing Figures 8-2, 8-1 and 3-3. As the dc potential is swept past E_A^* or E_C^*, a change in the product state takes place giving rise

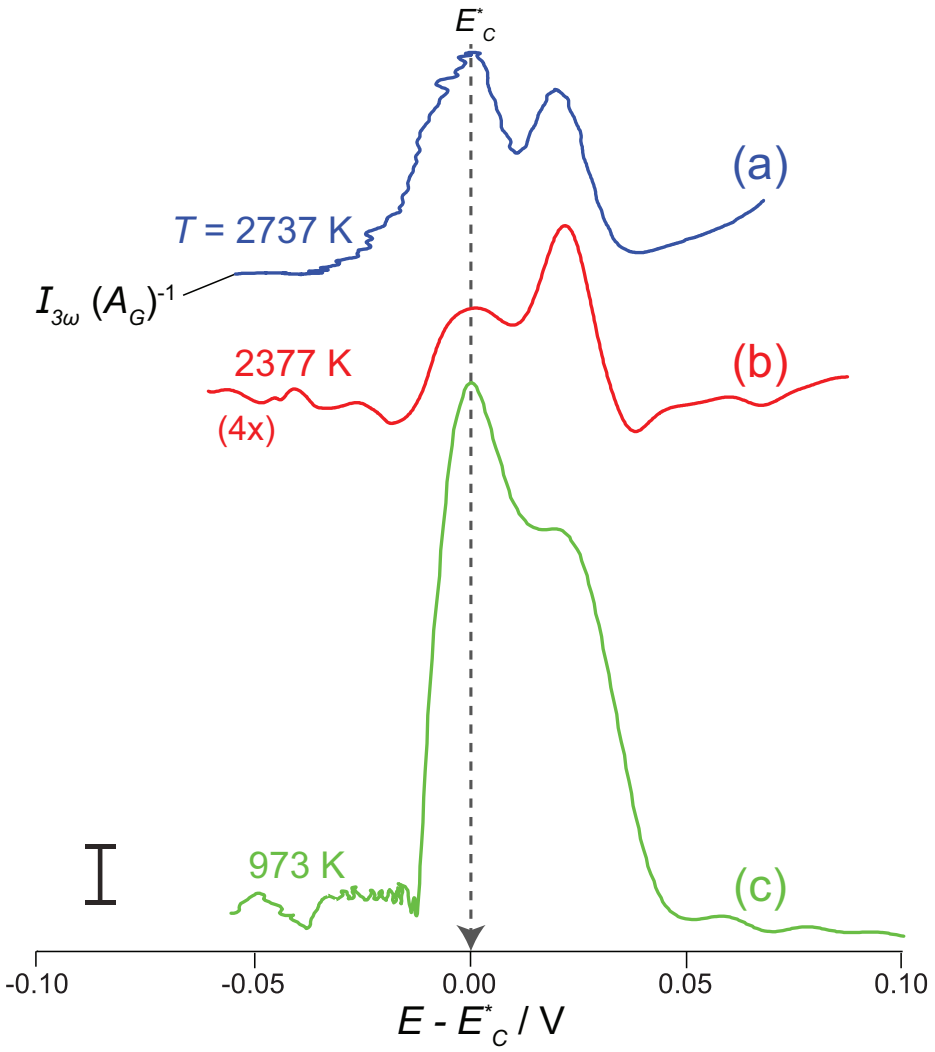

Figure 8-2: Comparison of $I_{3\omega}$ involving metal deposition on a *cathode* composed of: Ir (Y-Ir liquid alloy formation) in Y_2O_3 (a), Ir (Al-Ir liquid alloy formation) in Al_2O_3 (b) and gold (Na-K-Au liquid alloy formation) in NaCl-KCl (c); y-axis scale bar 10 mA cm^{-2}. The parameters employed for electrochemical measurements are described in the corresponding chapters for these electrolytes.

to a characteristic ACV harmonic response. This relationship supports the validity of the hypothesis, i.e. connection between equilibrium properties of reactants and electrochemical signals, and was essential for defining the equilibrium relation using the proposed electrolytic cell method. Combined with *in situ* visual observation of the electrodes and droplet provided by the TIF technique, the connections between ACV signals and electrode reactions were exploited for decomposition voltage measurement. These features of the present method will be valuable for potentially

increasing the experimental throughput during investigation in other electrolytes and conditions.

8.3 Connections between decomposition voltage measurements and thermodynamic properties

In NaCl-KCl, the electrode potential corresponding to chlorine gas evolution obtained using the current-interrupt method was compared with the results of ACV peak-splitting analysis. Discrepancies for values obtained by ACV and current-interrupt methods were observed, which was attributed to the irreversibility (activation overpotential) accompanying chlorine gas evolution for the conditions investigated. Nevertheless, the close correspondence verifies the relationship between ACV signals, electrode potential and the state of chlorine gas on an inert anode. For the cathode, measured electrode potentials for reactions involving metal deposition and alloy formation accompanying the decomposition of NaCl-KCl on Mo and Au cathode compared favorably with thermodynamic calculations.

In Al_2O_3, a systematic investigation of oxygen evolution on an Ir anode revealed the oxygen electrode-like behavior for the Ir anode and RE. Under certain conditions, the electrode potential E_A^* was found to obey the Nernst equation, which confirmed the correlation between ACV signals, measured electrode potentials and equilibrium states of the electroactive species. Additionally, the measured and previously predicted chemical potential and partial molar entropy for Al were in close agreement, which validates the electrolytic cell method proposed in §5 utilizing the anode as a polarized dynamic oxygen electrode exhibiting negligible activation overpotential.

In molten La_2O_3-Y_2O_3, the results for the mixing properties of the electrolyte were found to contradict previous predictions. Nevertheless, given the observed selective extraction La from La_2O_3-Y_2O_3, the previous predictions of ideal mixing for molten La_2O_3-Y_2O_3 appear to be inaccurate. Improvements to the accuracy and reliability of decomposition voltage measurement analysis (discussed in §7 and §5) and the

availability of data obtained by supplementary means (e.g. computational methods) for molten La_2O_3-Y_2O_3 may resolve this discrepancy.

Together, these results indicate that, indeed as hypothesized, electrode potentials, likely thanks to facile kinetics at UHT, are governed by equilibrium properties of the reacting species during decomposition voltage measurements. Therefore, the thermodynamic properties of electrolyte or products in such conditions may be determined with careful decomposition voltage measurements utilizing ACV and appropriate correction for ohmic drop.

Chapter 9

Perspectives & future work

An electrolytic cell method was proposed and validated providing direct measurements of Gibbs energy in refractory oxide melts at UHT. The potential scientific and technological consequences of the present findings are discussed. Additionally, substantial efforts beyond the scope of the current work for improving and extending the proposed approach (described in §4 and §5) are recommended.

9.1 Perspectives

9.1.1 Containerless method for the electrochemical study of high temperature, reactive melts

A pioneering effort was pursued enabling electrochemical operation in molten refractory oxides at temperatures above 2000 K for the first time. The rules of electrochemistry have been demonstrated to apply to systems at temperatures well above 2500 K, and the experimental approach presented herein enables precise electrochemical measurements within these material systems. The method of containerless operation in a pendant droplet may find potential utility in other high temperature, reactive melts where the container represents a significant materials challenge (e.g. fluorides, sulfides, other refractory oxides)

9.1.2 Containerless method for direct measurement of Gibbs energy

A method for containerless, direct measurement of Gibbs energy was validated in molten Al_2O_3 and extended to La_2O_3-Y_2O_3, materials and conditions otherwise experimentally challenging to study. For similar situations in which an inert anode is available, decomposition voltage measurements are related to the difference in chemical potential between the reduced species in the oxide and alloy phases. If a reliable thermodynamic description of one of these phases is available, such method provides a means of informing the thermodynamic for the other phase. Utilizing such an approach in comparison with other methods (reviewed in §1.2) for Gibbs energy measurement offers potential for accelerated pace of thermodynamic property measurements at UHT.

9.1.3 UHT reference electrode for molten oxides

A polarized dynamic reference electrode was demonstrated in molten Al_2O_3, Y_2O_3 and La_2O_3. Such a reference electrode enabled the decomposition voltage measurement described and validated in this work and could be beneficial to extension of additional electroanalytical methods, e.g. titration, for similar systems and conditions.

9.1.4 An inert electrode for oxygen evolution in UHT oxide melts

The results of Al_2O_3 and La_2O_3-Y_2O_3, demonstrate that Ir behaves as an inert electrode, capable of supporting oxygen evolution. Perhaps, Ir exhibits inert behavior in other UHT melts. To the benefit of extraterrestrial applications requiring oxygen for life support or fuel, herein the feasibility of oxygen generation in Al_2O_3-rich electrolytes has been demonstrated and Ir represents a promising inert anode material.

9.1.5 New electrolytes for reactive metals extraction & materials synthesis

The results presented herein confirm the electrolytic nature of molten Al_2O_3, Y_2O_3 and La_2O_3. Perhaps, other refractory oxides may be shown to exhibit ionic behavior using the pendant droplet approach described herein. Nevertheless, the melts investigated could be employed for coating refractory materials (e.g. Ir) or the extraction of metals (e.g. the selective extraction of REE's).

9.2 Future Work

9.2.1 Improvements & advancements to the present test facility

Opportunities remain for improving the test facility developed herein for UHT operation, most pertinently including developing a means for absolute temperature measurement and pursuing thermal modeling of the pendant droplet and electrodes for optimization and control of temperature gradients, heating efficiency and cell design. Further, electrochemistry represents one avenue for thermophysical property generation. The addition or coupling of other instrumentation (e.g. synchrotron X-ray diffraction or high-speed/high-resolution imaging) utilizing the containerless features of a pendant droplet method (namely, wide-angle access) will yield new opportunities for measuring thermophysical property measurements and studying material interactions in high temperature, reactive melts. This effort is certain to benefit our ability to experimentally support the development of structure-property relationships for liquids otherwise experimentally very challenging to investigate.

9.2.2 Modeling ACV signals

A qualitative connection was observed for the reactions involving a concentrated electrolyte on a reactive cathode and gas evolution on an inert anode as described in

§8. An electrochemical theory which predicts these relations does not exist at present. Development of a theoretical treatment for such reactions would significantly enhance the fidelity of signal interpretation as related to decomposition voltage measurement (i.e. improve accuracy for half-wave potential measurement), while providing access to kinetic parameters (e.g. rate constants, diffusivities, etc.).

9.2.3 Extension of decomposition method to other systems

Herein, a small subset of the refractory oxide melts was investigated. Certainly, ready opportunities exist for extension of the present method to multicomponent mixtures of the oxides investigated. Perhaps, this approach or a variation thereof may be readily extended to other refractory oxide melts and ionic systems (e.g. fluorides, sulfides, etc.).

9.2.4 Influence of dissolved oxygen on interpretation of decomposition voltage measurements involving co-deposition

The thermodynamic analysis for Y_2O_3-La_2O_3 was likely challenged by back reaction of Y-La during quenching with dissolved oxygen. Triple phase boundary (Droplet-electrode-gas) interface source of oxygen. Removal of this triple phase boundary or reduction in oxygen concentration in the atmosphere could remove dissolved oxygen contribution for studies involving reactive, co-depositing species, e.g. REE's.

9.2.5 Electronic conductivity

For melts exhibiting partial electronic conductivity, a method is needed for accounting for dealing with the contributions of the electronic depolarization. This would greatly enhance the accuracy and applicability of the electrolytic cell method developed herein to a significantly broader group of materials systems exhibiting mixed electronic-ionic conduction.

9.2.6 Facility for studying the behavior of materials at UHT

Ir was selected as an electrode for investigation in the molten refractory oxides. However, other materials nitrides, borides, carbides, intermetallic compounds may prove suitable electrodes for various electrolytes (fluorides, sulfides, oxides, etc.) at high temperature. The pendant droplet technique combined with the TIF provides an ability for rapidly investigating material interactions, or compatibility, and behavior at temperatures approaching 3000 K in a variety of atmospheres (vacuum, inert, reducing and oxidizing). Perhaps, the pendant droplet technique coupled with the electrochemical methods developed herein and the future along with the coupling of additional analytical techniques will enable discovery of new materials for high temperature processing.

Appendix A

Concentration polarization

The effects of concentration polarization in concentrated electrolytes is discussed and anticipated to contribute negligibly. This feature of highly concentrated electrolytes has been described previously with varying degrees of rigor [1]–[3].

A.1 Pseudo unary component electrolytes

For pseudo unary component electrolytes, a *supporting* electrolyte is not present. Fluxes due to migration, in addition to diffusion, are anticipated to dominate the behavior of such electrolytes. Generally, the electrolyte may be composed of complexed species, nevertheless only the deviation in concentration of the reacting species at the electrode interface needs consideration. Under the constraints of charge neutrality, the concentration of ions will be fixed under typical gradients of electric fields. Therefore, concentration polarization is not expected to contribute polarization as suggested by [1].

A.2 Pseudo binary & higher order electrolytes with a single depositing species

Kawamura et al. [2], [3] investigated of Pb^{2+}/Pb^{0} on Pt electrodes from $Na_2O-SiO2$, Na_2O-B_2O3 and $Na_2O-Al_2O_3-SiO2$ melts. After extensive characterization, Kawamura et al. determined that an "abrupt current rise" during cyclic voltammetry measurements was due to liquid Pb-Pt alloy formation on the cathode. Computer simulations showed that the concentration of Pb^{2+} at the surface of the cathode deviated little from bulk concentration during liquid Pb-Pt alloy formation, which justified the assumption of negligible concentration polarization by Kawamura et al.

To explain this result in a general way, an approximate, but general relation for verifying conditions that $\Delta\mu_O \approx 0$ can be derived. First, consider the deposition of M^{z+} ions (O) on a reactive electrode composed of N atoms to form a binary alloy N-M. The binary N-M phase diagram is like that described by [2], [3]. The solidus composition is C_M^{sol} at a temperature T ($P = 0.1\ MPa$). At the electrode-electrolyte interface the flux J of reduced and oxidized species must balance due to conservation of mass:

$$J_{M^+} = J_M \tag{A.1}$$

The flux of species i through a semi-infinite plane is given by Fick's first law in 1-D:

$$J_i = -D_i \frac{dC}{dx} \approx -D_i \frac{\Delta C}{\Delta x}$$

Note we are considering the evolution of the diffusion boundary at the melt-metal interface while the electrode potential is linearly swept with respect to time. To a first approximation assume the diffusion boundary length Δx is given by $\sqrt{4Dt}$. Considering the situation at time t_o when the liquid alloy first forms. The flux of M atoms in the solid metal is given by:

$$J_M = D_M \frac{C_M^{sol} - 0}{\sqrt{4D_M t_o}} = D_M^{1/2} \frac{C_M^{sol}}{\sqrt{4t_o}} \tag{A.2}$$

and for the melt with bulk concentration $C^*_{M^+}$ and surface concentration C_{M^+}:

$$J_{M^+} = D_{M^+}\frac{C^*_{M^+} - C_{M^+}}{\sqrt{4D_{M^+}t_o}} = (D_{M^+})^{1/2}\,\frac{\Delta C_{M^+}}{\sqrt{4t_o}} \tag{A.3}$$

Subbing A.2 and A.3 into A.1, rearranging, and solving for the change in C^+_M relative to the bulk concentration $C^*_{M^+}$:

$$\frac{\Delta C_{M^+}}{C^*_{M^+}} = \left(\frac{D_M}{D^+_M}\right)^{1/2}\frac{C^{sol}_M}{C^*_{M^+}}$$

Assuming constant activity coefficient for the concentration range considered (i.e. ΔC_{M^+} is small), the change in chemical potential of M^+ from bulk to electrode interface may be taken as

$$\frac{\Delta\mu_{M^+}}{RT} = \ln\left(\frac{C_{M^+}}{C^*_{M^+}}\right) = \ln\left(1 - \frac{\Delta C_{M^+}}{C^*_{M^+}}\right) = \ln\left[1 - \left(\frac{D_M}{D^+_M}\right)^{1/2}\frac{C^{sol}_M}{C^*_{M^+}}\right]$$

Assuming $D_M \approx 10^{-9}\ cm^2\ s^{-1}$, $D^+_M \approx 10^{-5}\ cm^2\ s^{-1}$, and

$$C^{sol}_M \approx \frac{X^{sol}_{M(N)}}{V_m(N)} = \left[X^{sol}_{M(N)} \approx 0.1\ and\ V_m(N = Pt) = 9.09\times10^{-3}\ L\ mol^{-1}\right] \approx 10\ M$$

yields

$$\frac{\Delta\mu_{M^+}}{RT} \approx \ln\left[1 - \frac{(0.1\ M)}{C^*_{M^+}}\right]$$

For $C^*_{M^+} >> 0.1\ M$, $\frac{\Delta\mu_{M^+}}{RT} \to 0$. Therefore, for highly concentrated melts involving the formation of a liquid alloy, the change in chemical potential of the cations is negligible. For example, in pure molten Al_2O_3 the concentration of Al^{3+} ions is approximately 57 M.

A.3 Co-deposition from a concentrated pseudo-binary electrolyte

For co-depositing species, the justification follows a very similar set of logic to that described in the previous section. However, the presence of migration effects is envisioned to make the analysis more complex. For now, we simply conclude that the behavior in such systems falls somewhere between the extremes presented in the previous two sections.

References

[1] Y. K. Delimarskii and B. F. Markov, *Electrochemistry of Fused Salts (Translated)*, R. E. Wood, Ed. Washington D.C.: The Sigma Press, Publishers, 1961, p. 338.

[2] K. Kawamura and T. Yokokawa, "Linear sweep voltammetry of Pb^{2+}/Pb in oxide melts," *J. Electrochem. Soc.*, vol. 135, no. 6, pp. 1447–1451, 1988.

[3] A. Sasahira, K. Kawamura, M. Shimizu, N. Takada, M. Hongo, and T. Yokokawa, "Pb^{2+}/Pb redox equilibria in sodium borate, silicate, and aluminosilicate melts," *J. Electrochem. Soc.*, vol. 136, no. 7, pp. 1861–1864, 1989.

Appendix B

Selected properties of some oxide compounds

In §2.6, the zero Kelvin electronic band gap (E_g) [1] and electronegativity difference ($\Delta\chi = \chi_X - \chi_M$) [2] of binary metal compounds (i.e. MX_z) of the halogens, oxides, sulphides and nitrides (i.e. X = F, Cl, Br, I, O, S, N) were considered during selection of a suitable of electrolyte for the present work. A table of these quantities along with predicted zero Kelvin enthalpy of formation ($\Delta_f H_{0K}$), predicted zero Kelvin density (ρ_{0K}), space group and Materials Project ID (MP-ID) [1] for oxide compounds considered in the present work are presented in Table B.1 below in order of increasing atomic number (Z_M). Note the oxide compounds (MO_z) appearing in Table B.1 were filtered according to the following criteria:

- Availability via the Materials Project on September 28, 2017
- $E_g > 1$ eV
- $\Delta\chi > 1.4$
- Employs typically observed stoichiometry at $T = 298$ K
- Possesses most stable structure computed by density functional theory at $T = 0$ K

Additional properties for other compounds are available at The Materials Project's database via the web (`https://www.materialsproject.org`) [1].

Table B.1: Selected properties of some binary oxide compounds (MO_z).

Z_M	M	z	$\Delta\chi$	E_g/eV	$\Delta_f H_{0K}$/eV	ρ_{0K}/g cm^{-3}	space group	MP-ID
3	Li	0.5	2.46	4.899	-2.071	1.963	Fm3m	mp-1960
4	Be	1	1.87	7.46	-3.122	2.966	P63mc	mp-2542
5	B	1.5	1.4	6.302	-2.813	2.344	P3121	mp-306
11	Na	0.5	2.51	1.874	-1.454	2.35	Fm3m	mp-2352
12	Mg	1	2.13	4.445	-3.071	3.471	Fm3m	mp-1265
13	Al	1.5	1.83	5.854	-3.442	3.873	R3c	mp-1143
14	Si	2	1.54	5.703	-3.285	2.107	I42d	mp-546794
19	K	0.5	2.62	1.707	-1.265	2.291	Fm3m	mp-971
20	Ca	1	2.44	3.634	-3.323	3.287	Fm3m	mp-2605
21	Sc	1.5	2.08	3.824	-3.986	3.761	Ia3	mp-216
22	Ti	2	1.9	2.677	-3.518	3.616	C2/m	mp-554278
23	V	2.5	1.81	2.156	-2.305	3.054	Pmmn	mp-25620
24	Cr	1.5	1.78	2.437	-2.349	4.893	R3c	mp-19399
25	Mn	1	1.89	1.682	-2	5.191	Fm3m	mp-714882
25	Mn	2	1.89	1.865	-1.798	3.087	R3m	mp-34134
26	Fe	1	1.61	1.538	-1.687	5.436	P1	mp-705424
26	Fe	1.5	1.61	2.019	-1.886	4.937	C2	mp-715572
28	Ni	1	1.53	2.317	-0.934	6.676	Fm3m	mp-715434
31	Ga	1.5	1.63	2.008	-2.283	5.68	C2/m	mp-886
32	Ge	2	1.43	3.249	-2.094	4.044	P3221	mp-223
37	Rb	0.5	2.62	1.645	-1.12	4.072	Pnma	mp-755738
38	Sr	1	2.49	3.275	-3.094	4.878	Fm3m	mp-2472
39	Y	1.5	2.22	4.053	-3.986	4.892	Ia3	mp-2652
40	Zr	2	2.11	3.474	-3.833	5.564	P21/c	mp-2858
41	Nb	2.5	1.84	1.614	-3.052	4.261	P1	mp-680944
50	Sn	2	1.48	2.087	-2.056	5.363	I4/m	mvc-15363
55	Cs	0.5	2.65	1.651	-1.133	4.827	Pnma	mp-755573
56	Ba	1	2.55	2.091	-2.834	5.753	Fm3m	mp-1342
57	La	1.5	2.34	3.532	-3.895	5.84	Ia3	mp-2292
58	Ce	2	2.32	1.865	-3.945	6.995	Fm3m	mp-20194
59	Pr	1.5	2.31	3.659	-3.753	6.09	Ia3	mp-16705
60	Nd	1.5	2.3	3.708	-3.799	6.396	Ia3	mp-1045
62	Sm	1.5	2.27	3.782	-3.879	6.962	Ia3	mp-218
64	Gd	1.5	2.24	3.037	-3.906	7.515	Ia3	mp-504886
66	Dy	1.5	2.22	3.997	-3.986	8.833	C2/m	mp-555574
67	Ho	1.5	2.21	4.239	-3.983	9.253	P3m1	mp-13065
68	Er	1.5	2.2	4.192	-3.998	9.518	P3m1	mp-13066
72	Hf	2	2.14	4.668	-3.985	10.362	P42/nmc	mp-1018721
73	Ta	2.5	1.94	2.727	-3.356	7.371	Pmnm	mvc-4415
75	Re	3.5	1.54	2.675	-2.048	5.838	P212121	mp-1016092
83	Bi	1.5	1.42	2.187	-1.66	9.06	P21/c	mp-23262
89	Ac	1.5	2.34	3.523	-3.76	8.975	P3m1	mp-11107
92	U	3	2.06	1.635	-3.63	6.575	Pm3m	mp-375

References

[1] A. Jain, S. P. Ong, G. Hautier, W. Chen, S. Richards, William Davidson Dacek, S. Cholia, D. Gunter, D. Skinner, G. Ceder, and K. A. Persson, "The Materials Project: A materials genome approach to accelerating materials innovation," *APL Mater.*, vol. 1, no. 1, p. 011 002, 2013.

[2] J. E. Huheey, E. A. Keiter, and R. L. Keiter, *Inorganic Chemistry: Principles of Strucutre and Reactivity*, 4th ed. New York: Harper Collins, 1993.

Appendix C

Electrochemical study of a pendant molten molten alumina droplet and its application for thermodynamic property measurements of Al-Ir

Included below is the final version of the article entitled "Electrochemical study of a pendant molten molten alumina droplet and its application for thermodynamic property measurements of Al-Ir" submitted and published by the Journal of the Electrochemical Society. The full citation is:

B. R. Nakanishi and A. Allanore. "Electrochemical study of a pendant molten molten alumina droplet and its application for thermodynamic property measurements of Al-Ir." In: *J. Electrochem. Soc.* 164.13 (2017), E460. DOI: 10.1149/2.1091713jes

Electrochemical study of a pendant molten alumina droplet and its application for thermodynamic property measurements of Al-Ir

Bradley R. Nakanishi and Antoine Allanore

Affiliation: Department of Materials Science and Engineering, Massachusetts Institute of Technology, Cambridge, MA, USA

Keywords: AC voltammetry, molten alumina, aluminum oxide, oxygen evolution, iridium, iridium-aluminum alloys, Gibbs energy, entropy, metal deposition, liquid metals, molten oxide electrolysis

Abstract

Limited knowledge of the thermodynamic and transport properties of refractory materials in the liquid state remains a key challenge limiting their application. Using alternating current (AC) and direct current (DC) techniques, the electrochemical kinetics of oxygen evolution and metal deposition was investigated in a pendant droplet of molten alumina (Al_2O_3) with three iridium (Ir) electrodes in a thermal imaging furnace. For the first time, the direct electrolytic decomposition of molten Al_2O_3 to oxygen gas and aluminum (Al) metal (alloyed with Ir) was observed, confirming the ionic nature of molten Al_2O_3. The decomposition potential of molten Al_2O_3 was measured with high precision using AC voltammetry, and the results demonstrated remarkable sensitivity to variation in temperature enabling measurement of chemical potential and entropy of Al at the Ir-rich solid-liquid phase boundary for the first time. The results were in remarkably close agreement with the most recent thermodynamic assessment of the Al-Ir system.

Introduction

Structural materials developed for lasers, nuclear, aerospace or materials processing are required to sustain high temperature, and therefore often rely on solid refractory materials, e.g. iridium-based superalloys exhibiting exceptional corrosion and creep resistance [1]. The ultimate temperature of stability for those solid phases is captured in the phase diagram by their equilibrium with the liquid phase, usually found at ultra-high temperature (UHT, $T > 2000$ K). For the refractory oxides, where herein the adjective “refractory” relates to a metal oxide more stable than SiO_2 (e.g. Al_2O_3), the chemical bonding responsible for their stability in the solid-state also contributes to their UHT melting points. Unfortunately, information for materials at UHT in both condensed states remains extremely limited [2]–

[5]. In particular, property prediction for melts by *ab initio* techniques remains time consuming and limited to specific compositions and temperatures, and their validation requires reliable experimental data [6].

Limited information for refractory melts is derived from the difficulty of UHT experiments. For example, containment selection remains a critical step and a key challenge. Interestingly, the difficulty for containment selection also stems from a lack of thermodynamic and reaction kinetic information for refractory materials. Reviews of existing techniques for thermodynamic property measurement of refractory melts are found elsewhere [5], [7]. The state of the art relies primarily on equilibration [5], calorimetry [8], [9], and diffraction measurements [10], [11]. These methods can provide phase-transition temperatures, enthalpies of formation or heat capacities, but only vapor pressure or electromotive force (EMF) measurements provide direct access to chemical potentials (Gibbs energy), the quintessential thermodynamic quantity for phase diagram boundaries prediction [7]. Unfortunately, vapor pressure measurements are rarely feasible for refractory melts, exhibiting particularly low vapor pressures ordinarily, and EMF methods typically require an ion-selective membrane [12], an additional materials challenge at UHT.

However, given the nature of their bonding, refractory oxide melts can be postulated to exhibit ionic behavior upon fusion, enabling property measurements at UHT by electrochemical methods. Using these materials as electrolytes could enable determination of chemical potential and entropy, along with transport properties, such as diffusivity or electrical conductivity as demonstrated extensively in silicate melts [3], [13]–[18]. To date, however, no electrochemical techniques have been demonstrated in molten oxides above 2000 K.

Given the likelihood of contamination of the refractory melts at UHT, containerless approaches are preferred, such as electrostatic [19], aerodynamic [20]–[22] or acoustic [23], [24] levitation techniques. While these methods are currently preferred for measuring structure [10], [11], [25], [26], total conductivity [21], density, viscosity and surface tension [24], [27] or even integral thermodynamic properties [28], the sample size is necessarily small (1-4 mm) and each method is limited to their respective subset of compatible atmospheres (e.g. vacuum only for electrostatic levitation). Furthermore, all of these methods preclude electrochemical investigation as contacting electrodes to a droplet interfere with its levitation. As a matter of fact, no studies utilizing levitation have reported partial thermodynamic properties to date.

An alternative containerless approach handling a larger amount of material is the pendant droplet technique. This technique originated with the rise of the thermal imaging (or arc imaging) furnace (TIF) [29], which was extensively developed for and is nearly exclusively associated with the floating zone crystal growth method [30]–[33]. Historically, TIFs provided for the first time “essentially unlimited”

temperature ranges for melting essentially any material in "practically any atmosphere" [32]. Despite their focus on improving crystal growth at the time, Field and Wagner [32] suggested that "the technique can be utilized for other high temperature experiments of importance to material research ...". Diamond and Dragoo were among the first to take advantage of these opportunities to directly observe the solubility of gases (Ar, O_2, H_2, H_2O, N_2, and He) and their effects on vaporization behavior of molten pendant droplets of Al_2O_3 [34]. Soon after the advent of lasers, they were utilized as a heat source in TIFs for their superior heating efficiency [35], [36]. For example, Nelson et al. revisited the solubility of gaseous species in molten Al_2O_3 and their effects on solidification [37]. Later, Krishnan et al. measured the refractive index of molten Al_2O_3 in a laser-heated pendant droplet [38]. Only recently Katsumata et al. initiated electrical measurements in a TIF to measure the thermopower of molten TiO_2 using two iridium (Ir) electrodes [39]. No investigations combining electrical and chemical measurements using the pendant droplet technique have been reported.

Herein, a novel setup that combines the unique features of a pendant droplet in a TIF with three electrode measurements for studying the electrochemistry of refractory oxide melts is described. Furthermore, results from an extensive investigation of molten Al_2O_3 as an electrolyte and Ir electrodes is presented, illustrating a novel approach for thermodynamic measurements of chemical potential and entropy in refractory melts.

Experimental Methods

Sample Rod and Electrode Probe Preparation

Rod-shaped green bodies of samples were prepared from fine aluminum oxide powders (Al_2O_3 > 99.95% metals basis, diameter Ø = 0.25 to 0.45 µm, Alfa Aesar) placed in latex balloons (Pioneer Balloon Co.) and hydrostatically pressed at 200 MPa for 5 minutes, followed by sintering in air at 1873 K for 5 hours in a horizontal tube furnace (1725HT Furnace, CM Inc.). The sintered samples were 5 to 7 mm in diameter and 60 to 80 mm in length with a density measured by an Archimedes principle-based method [40], [41] corresponding to > 90% of the theoretical density. The sintered samples were notched at one end and wound with a nichrome wire ($Ni_{60}Cr_{16}Fe_{24}$, Ø = 0.45 mm) loop for suspension from the upper furnace shaft.

Three Ir wire electrodes (Ir > 99.9%, Ø = 0.5 mm, 20 mm length, Furuya Metals Co., Ltd.) were spot-welded at their base to Ni wire leads (Ni >99.8% , Ø 0.38 mm, Alfa Aesar), and inserted through one end of a four-bore Al_2O_3 tube (Al_2O_3 > 99.6%, *Ø(outer)* = 6.35 mm, AdValue Technology LLC). The Ni wire leads were extended outside of the furnace tube by securely wrapping Ni-clad copper wire (27% Ni - 73% Cu, Ø = 0.81 mm, Anomet Products Inc.). No visible signs of melting or oxidation of the electrical connections were observed following operation due to the large temperature gradients present outside of

the furnace hot zone (up to 200 K mm^{-1}). The bottom end of the four-bore tube was sealed with epoxy outside of the furnace. The assembled electrode probe was typically 800 mm long and at least 10 mm of Ir wire was exposed above the Al_2O_3 four-bore tube.

Electrochemical Measurements

A three-electrode configuration was employed using Ir wires for the working (WE), counter (CE) and pseudo-reference (RE) electrodes. The RE consisted of an Ir wire immersed in the molten droplet. All measured potentials are referred to this RE, unless stated otherwise. One of three geometries was employed for the WE and CE: 1) a single Ir wire with an approximate geometric surface area (A_G) of 0.07 cm^2, 2) a single Ir wire that was approximately 2 mm longer (A_G = 0.13 cm^2), or 3) two Ir wires TIG-welded together at their tips forming a spherical junction (approximately Ø = 1 mm, A_G = 0.25 cm^2).

Open circuit potential (OCP), electrochemical impedance spectroscopy (EIS), direct current (DC) linear sweep voltammetry (LSV), large amplitude Fourier transform alternating-current voltammetry (ACV) and potentiostatic and galvanostatic electrolysis measurements were performed. The details of the equipment and measurement methods are available elsewhere [42], and only important variations are reported herein.

The cell voltage, WE potential and current were recorded during potentiostatic electrolysis experiments using a data acquisition module (DAQ, DT9837B, Data Translation, Inc.) at 36,125 Hz sampling frequency. The sinewave signal for ACV measurements was generated by a digital-to-analog function generator (DS360, Stanford Research Systems). Signal processing was performed post-recording using a code written with Scilab. The DC, 1st and higher harmonics of the current signal were obtained by inverse Fourier transform after selection of the appropriate frequency range, as presented in reference [43]. Given the nearly linear behavior of the nonfaradaic current contributions, e.g. double-layer charging, and the inherently nonlinear response of faradaic reactions, the second and higher harmonics were used to confirm the presence of faradaic reactions and determine its half-wave potential, as described in more detail in [44]. The behavior of the WE at negative and positive potentials were studied in separate experiments. Additionally, during a subset of the ACV measurements, the cell voltage was simultaneously recorded. For this subset of measurements, the behavior of the WE at negative and positive potentials was studied on distinct electrodes (designated as “cathode” and “anode,” resp.) within the same experiment.

DC WE and cell voltages were corrected for ohmic drop using the product of the DC current with a resistance determined as follows. The uncompensated resistance (R_u) and additional model parameters for the impedance were obtained by fitting EIS spectra to the equivalent circuit detailed in Appendix A, using ZView® software (Scribner Associates, Inc). Voltammetry potential corrections for LSV and ACV

required typically 80% of R_u in order to observe a monotonic variation of the DC current response with the DC potential. Cell voltage measurements was corrected using the full cell resistance (R_{cell}) obtained upon fitting the open circuit EIS spectrum. While R_u proved to decrease (-20%, typically) from open circuit values during cathodic polarization, R_{cell} only slightly changed during cell polarization (<5%). The compensated resistance (R_c) between the CE and RE ($R_c \approx R_{cell} - R_u$) was found to increase during cathodic polarization of the WE (resp. anodic polarization of the CE) in such a way as to effectively balance the decrease in R_u, therefore justifying the negligible variation in R_{cell} during open circuit and polarization measurements.

Temperature Measurement

Variation in the open circuit uncompensated resistance (R_u) with TIF lamp power (P_L) was used to evaluate temperature, as described in Appendix B using Eq. (B2). At the minimum P_L required for electrode insertion into the droplet, the absolute temperature was assumed to be 2377 K, a 50 K superheat above the melting point of Al_2O_3, $T_m(Al_2O_3)$. The maximum error with respect to variation in temperature is estimated at less than 10 K, and the absolute temperature measurement error is approximately the superheat assumption, herein 50 K.

Operation

A TIF equipped with four Xe lamps (12 kW total) and ellipsoidal mirrors, schematically shown in Figure 1, was modified for electrochemical measurements. In practice, two TIFs were employed (models FZ-T-12000-X-IV-VP and TX-12000-I-MIT-VPO-PC, Crystal Systems Corp.), which will hereafter be designated TIF I and TIF II, resp. Unless noted otherwise, the results following were obtained with TIF II. The sample rod, suspended from the upper rotating shaft, was positioned with its bottom end at the focal point of the mirrors, hereafter called “hot zone”. The electrode probe was introduced through the bottom port. The vertical positions of the sample and probe were controlled independently by stepper motors with sub-millimeter precision. The probe and sample assembly were isolated from ambient atmosphere with a quartz tube (Technical Glass Products Inc.) sealed with Viton O-rings. A camera (EOS Rebel T5i DSLR, Canon Inc.) with a telescopic lens was employed for continuous monitoring and video recording of the sample and electrodes in the hot zone.

The inside of the quartz tube was evacuated and refilled three times with one of three gases designated “Gas A”, “Gas B” and “Gas C” hereafter. Gases A and B were > 99.999% Ar and Gas C was 990 ppm O_2 with the balance Ar (UHP and certified calibration gas resp., all products Airgas Inc.). After purging, the gas flow rate was set to 50 mL min^{-1} controlled by a digital mass flow controller (FC-260V, Tylan General Inc.). The Xe lamps were powered on and P_L was gradually increased until the bottom of

the rotating sample was visually molten. A stable pendant droplet formed, suspended by a balance between the melt surface tension and gravity. Rotation was halted, and the electrodes were raised upwards while monitoring the open circuit potential (E_{oc}). Visual observation and decrease in $|E_{oc}|$ ($|E_{oc}|$ < 5 mV, typically) confirmed electrode insertion into the droplet. A trace oxygen (O_2) gas sensor (model 2001RSM, Advanced Micro Instruments Inc., sensor calibrated with air) was connected to the furnace exhaust gas for O_2 concentration quantification. At the end of the electrochemical measurements, the lamps were shut off to quench the droplet and electrodes; with cooling rates greater than 100 K s^{-1}.

Post-Experiment Observation and Analysis

Following experiment, the droplet and electrodes were sectioned using a diamond saw. The sections were cast in epoxy (Buehler) and fully cured. The mounted specimens were ground with diamond abrasive pads and polished using a diamond suspension (Allied High Tech Products Inc.) down to 1 µm. Observations were made using an optical microscope and scanning electron microscope (SEM) equipped with an energy dispersive spectrometer (EDS). Further details regarding observation and analysis equipment can be found elsewhere [42].

Results

DC and AC Voltammetry

Figure 2 shows a typical DC linear sweep voltammogram in the negative-going potential scan where the current rapidly decreases with fluctuations from the starting scan limit (E = 1.05 V). Very large current densities (> 3.5 A cm^{-2}) are observed in this region. Further scanning toward negative potentials, a current plateau at 77 mA (label A) is observed at around E = 0.8 V. The current steadily decreases towards zero at open circuit (E = 0.03 V), close to the initial E_{oc}. On the cathodic portion of the curve (E < 0), the current smoothly decreases at an increasing rate (label B), until the current exhibits fluctuations (label C) at around E = -0.3 V. Extremely large current densities (> 10 A cm^{-2}) are observed for E < -0.4 V.

The typical results of ACV measurements for the first ($I_{1\omega}$), second ($I_{2\omega}$) and third ($I_{3\omega}$) harmonics of the current response are shown in Figure 3. For positive potentials, a faradaic event is observed at a half-wave potential E_A^* with the peak splitting feature across $I_{2\omega}$, $I_{3\omega}$ and higher harmonics [45]. Peak-splitting features are not clearly observed in lower harmonics possibly due to nonfaradaic contributions such as double layer charging. Gas composition was found to influence the position of E_A^*; in fact, increasing the furnace partial pressure of O_2 ($p_{O_2,furnace}$) systematically decreased E_A^*. For negative potentials, a faradaic event is observed at E_C^* with its own charateristic peak splitting. The

features of the shapes of the harmonic current responses for both anodic and cathodic faradaic reactions were found to be reproducible, independent of temperature and cycle number. While the peak heights in the second and third harmonic generally decreased during successive cycles at constant temperature, they remained readily distinguishable.

A summary of the measurements for E_A^* and E_C^* obtained using various experimental conditions is provided in Figure 4. Each data point corresponds to the mean of repeated measurements obtained from both positive- and negative-going scans. The error bars shown represent one standard deviation uncertainty arising from the lack of repeatability of the measured peak positions in successive cycles and scan directions. The error for R_u is estimated to be at most 10%. This corresponds to an additional error of +/- 10 mV for the position of E_A^* and E_C^* if instrument errors in measurement of the current and voltage are neglected. Results for the parameters of linear fitting for measurements of E_A^* and E_C^* versus temperature are shown in Figure 4. Note, E_A^* was fitted with a single parameter of first-order in temperature, and E_C^* was fitted with zeroth and first-order parameters.

ACV measurements were also conducted with simultaneous cell voltage measurement. The cell voltages (U) measured at E_A^* and E_C^* are also shown in Figure 3, hereafter designated $U(E_A^*)$ and $U(E_C^*)$. The cell geometry, i.e. the cathode and anode areas ($A_{G,C}$ and $A_{G,A}$, resp.) exposed to the electrolyte, was found to influence the relative values of $U(E_A^*)$ and $U(E_C^*)$, see Appendix D for further description. In practice, it was found that $U(E_C^*)$ was systematically greater than $U(E_A^*)$, when the cathode to anode area ratio ($A_{G,C}/A_{G,A}$) was greater than 0.5 and 0.3 for Gases A and C, resp. Regardless of cell geometry, oxygen gas evolution was detected in situ by visual observation near the anode for $U > U(E_A^*)$. For the condition $U(E_C^*) > U(E_A^*)$, achieved with careful cell design, $U(E_C^*)$ will hereafter be relabeled U^o. The variation of U^o as a function of temperature for Gases A and C is presented in Figure 5. A linear unweighted fitting of all the data using an equation of the form

$$U^o = \beta_0 + \beta_1 T$$

yields β_0 = 2380 +/- 570 mV and β_1 = -0.50 +/- 0.24 mV K^{-1}.

Electrolysis

To acquire further insight into the nature of the cathodic and anodic reactions coinciding with the faradaic events observed above, potentiostatic and galvanostatic electrolysis measurements were performed. As shown in Figure 6a, bubbling was observed perturbing the surface of the droplet above the anode when $U > U(E_A^*)$ during galvanostatic electrolysis measurements. The bubbling began immediately after applying current (typically 50 to 200 mA) to the cell. The bubbles successively emerged at a steady rate until the current was shut off, ceasing the bubbling. The O_2 gas sensor

subsequently recorded a sharp increase in p_{O_2} that steadily decreased back to its initial value prior to electrolysis, a behavior similar to that reported by Allanore et al. [46] in the study of another molten oxide electrolyte. After electrolysis at moderate cell voltages (i.e. $U(E_A^*) < U < U(E_C^*)$), a droplet was quenched by turning the lamps off and the droplet and electrodes were sectioned for further analysis. Despite the presence of small ($Ø$ < 1 μm) metallic particles evenly dispersed in the oxide phase, the cross-section and surface of the Ir anode remained unchanged. The Ir content in the oxide phase and Al content in the Ir cathode were both below the EDS detection limit.

Potentiostatic electrolysis measurements were also performed at high cell voltages (i.e. $U > U(E_C^*) > U(E_A^*)$) as presented in Figure 6b. For a current greater than 250 mA, gas bubbling in the vicinity of the anode and violently swirling convective currents were observed on the surface of the droplet. At very high current (> 1 A), the droplet destabilized and detached from the sample rod typically after only a few seconds of current flow. For the measurements presented in Figure 6b, the droplet remained stable for the duration of electrolysis. The lamps of the TIF were shut off after 60 s, prior to the end of electrolysis, quenching the droplet and electrodes. In Figure 7a, an optical micrograph shows a cross-section of the cathode in the solidified droplet. A deposit layer is observed on the cathode at its interface with the electrolyte. The apparent volume of the cathode increased along the section of the wire wetting the molten droplet, while the anode and RE appeared unchanged. Backscattered electron (BSE) images of the cathode microstructure are shown in Figure 7b and 7c. EDS analysis for the cathode cross-section reveals that the center of the cathode (region I in Figure 7a) is nearly pure Ir with a concentration of Al below detection limit. Region II, further from the central axis of the cathode, exhibits increasing Al concentration to a maximum mole fraction x_{Al} = 0.14. Region III consists of round particles of an Ir-rich phase (x_{Al} = 0.14, $Ø$ < 75 μm) surrounded by a lamellar two-phase structure composed of an Ir-rich phase with similar Al content and an Al-rich phase (x_{Al} = 0.40). A high magnification image of this region is shown in Figure 7c. Region IV contains a greater relative proportion of the lamellar two-phase field with dendritic-like structures composed of the Ir-rich phase (x_{Al} = 0.14). At the electrolyte-deposit interface, a thin (< 5 μm) layer of the Ir-rich phase (x_{Al} = 0.14) is observed.

Discussion

Anode and reference electrode behavior

The results and observations presented in Figures 2 to 4 and 6 demonstrate that the faradaic reaction measured on the anode WE at E_A^* and at a cell voltage $U(E_A^*)$ features O_2 gas evolution. In addition, the potential E_A^* proves sensitive to $p_{O_2,furnace}$. Experimental observations in this study show typically dispersed metallic particles of Ir in the melt similar to those reported in [47], but no detectable

signs of Ir loss were observed both while operating Ir as an anode during bulk electrolysis or as a RE. These findings are consistent with prior thermodynamic considerations, i.e. limited solubility of IrO_x in silicates and likely presence of both IrO_x (g) and O_2 (g) [48], [49]. Iridium in molten Al_2O_3 is therefore hereafter considered as an inert electrode under both open circuit and anodic polarization, within the parameters and limits of detection employed in this study.

Therefore, occurring simultaneously to a cathodic reaction on the CE to be discussed later, the half-cell reaction at the WE coinciding with E_A^* is envisaged to involve oxidation of oxide ions (O^{2-}) from molten Al_2O_3 into gaseous O_2 at the furnace pressure (0.1 MPa)

$$O^{2-}(\text{melt}) = 2e^-(\text{Ir}) + \frac{1}{2}O_2(\text{g}, 0.1\ \text{MPa}) \quad (1)$$

The thermodynamic equilibrium potential for Reaction (1) is associated with inner potential ϕ_A^*, which can be defined by

$$\phi_A^* = \frac{1}{4F}\mu_{O_2}^{anode} - \frac{1}{2F}\mu_{O^{2-}}^{anode} \quad (2)$$

where F = 96,485 C mol^{-1} and $\mu_{O^{2-}}^{anode}$ and $\mu_{O_2}^{anode}$ are the chemical potentials of O^{2-} and O_2 (g) at the anode. The standard state for O_2 (g) is chosen as pure O_2 (g) at temperature T and fugacity 0.1 MPa. Since low total pressures are encountered in this study, hereafter fugacity and partial pressure are assumed equivalent for O_2 (g), i.e. O_2 is an ideal gas and $\mu_{O_2}^{anode} = \mu_{O_2}^{o}$. The standard state for O^{2-} for $\mu_{O^{2-}}^{o}$ is defined as O^{2-} at its postulated molar concentration (85 mol L^{-1}) in pure molten Al_2O_3 at temperature T in the presence of pure O_2 (g) at 0.1 MPa. $\mu_{O^{2-}}^{anode}$ variation as a function of O^{2-} activity at the anode $a_{O^{2-}}^{anode}$ is described by

$$\mu_{O^{2-}}^{anode} = \mu_{O^{2-}}^{o} + RT\ln\left(a_{O^{2-}}^{anode}\right) \quad (3)$$

In such conditions one can consider in more detail the overall chemical equilibria controlling the electricochemical potential E_A^* recorded versus the Ir pseudo-reference ($\phi_{ref,A}^*$) such as reported in Figure 3 where

$$E_A^* = \phi_A^* - \phi_{ref,A}^* \quad (4)$$

Because no gas bubbles were visible on the RE electrode, the equilibria at the RE is assumed to involve O^{2-} from molten Al_2O_3 and dissolved atomic oxygen, the corresponding half-cell reaction being

$$O^{2-}(\text{melt}) = 2e^-(\text{Ir}) + O(\text{melt}) \quad (5)$$

And the associated potential $\phi_{ref,A}^*$ can be defined by

$$\phi_{ref,A}^* = \frac{1}{2F}\mu_O^{ref,A} - \frac{1}{2F}\mu_{O^{2-}}^{ref,A} \quad (6)$$

where $\mu_O^{ref,A}$ and $\mu_{O^{2-}}^{ref,A}$ are the chemical potentials of dissolved atomic oxygen and O^{2-}, respectively, at the RE, while Reaction (1) occurs at the WE. Using the same $\mu_{O^{2-}}^{o}$ defined previously for Eq. (3), enables

the expression of $\mu_{O^{2-}}^{ref,A}$ variation with $a_{O^{2-}}^{ref,A}$, the O^{2-} activity at the RE. The chemical potential of dissolved atomic oxygen ($\mu_O^{ref,A}$) is assumed to be related to the equivalent partial pressure of oxygen $p_{O_2,ref}^*$ assuming equilibrium between dissolved atomic oxygen and O_2 (g) in the furnace atmosphere:

$$\mathrm{O(melt)} = \frac{1}{2}\mathrm{O_2(g)}$$

In such conditions, $\mu_O^{ref,A}$ can be expressed as [50]:

$$\mu_O^{ref,A} = \frac{1}{2}\mu_{O_2}^o + \frac{RT}{2}\ln p_{O_2,ref}^* \quad (7)$$

Combining Eqs. (6) and (7), yields the following expression for $\phi_{ref,A}^*$

$$\phi_{ref,A}^* = \frac{1}{4F}\mu_{O_2}^o - \frac{1}{2F}\mu_{O^{2-}}^o + \frac{RT}{4F}\ln\left[\frac{p_{O_2,ref}^*}{\left(a_{O^{2-}}^{ref,A}\right)^2}\right] \quad (8)$$

E_A^* can then be related to $p_{O_2,ref}^*$ by combining Eqs. (2), (3) and (8) with (4):

$$E_A^* = \phi_A^* - \phi_{ref,A}^* = -\frac{RT}{4F}\ln\left[\left(\frac{a_{O^{2-}}^{anode}}{a_{O^{2-}}^{ref,A}}\right)^2 p_{O_2,ref}^*\right] \quad (9)$$

Assuming the ratio of oxide ion activities $\frac{a_{O^{2-}}^{anode}}{a_{O^{2-}}^{ref,A}}$ to be unity, which seems justifiable considering Ir as an inert anode and RE and molten Al_2O_3 as an electrolyte comprised primarily of O^{2-} and aluminum ions (Al^{3+}) satisfying charge neutrality, simplifies Eq. (9) to:

$$E_A^* = -\frac{RT}{4F}\ln\left(p_{O_2,ref}^*\right) \quad (10)$$

The single parameter fitting for E_A^* versus temperature reported in Figure 4 combined with Eq. (10) yields values of $p_{O_2,ref}^*$ for the three gas atmospheres investigated. The goodness of fit with a single first-order parameter suggests that the quantity

$$\left(\frac{a_{O^{2-}}^{anode}}{a_{O^{2-}}^{ref,A}}\right)^2 p_{O_2,ref}^*$$

is indeed invariant with temperature. Furthermore, $p_{O_2,ref}^*$ is evaluated by Eq. (10) to be 0.4, 21, and 190 Pa for Gas A ($P_{O_2,furnace}$ = 0.8 Pa, measured by trace O_2 gas sensor), Gas B ($p_{O_2,furnace}$ = 10 Pa, measured by trace O_2 gas sensor), and Gas C ($p_{O_2,furnace}$ = 990 Pa, certificate of analysis), resp. While limitations of the experimental procedure for controlling p_{O_2} at the droplet surface could at least partially explain discrepancies, the possibility of $\frac{a_{O^{2-}}^{anode}}{a_{O^{2-}}^{ref,A}}$ variation cannot be eliminated entirely. A systematic study with precise p_{O_2} control along with melt composition (i.e. basicity) variation is foreseen to provide enhanced understanding of $\frac{a_{O^{2-}}^{anode}}{a_{O^{2-}}^{ref,A}}$ and, more interestingly perhaps, oxide ion activity measurement.

Nevertheless, these observations support the validity of the assumptions for deriving Eq. (9) and, furthermore, exemplify a direct proportionality between $p^*_{O_2,ref}$ and $p_{O_2,furnace}$. The large surface area to volume ratio of a pendant droplet justifies the rapid equilibration of oxygen species between electrodes and furnace atmosphere required for $p_{O_2,furnace}$ sensitivity. While nearby concomitant reactions occurring at the CE (cathode) or even the absence of a supporting electrolyte, i.e. electromigration effects, may limit the accuracy of the proposed interpretation, the Ir pseudo-RE is demonstrated to exhibit oxygen-electrode-like behavior. Furthermore, the results are found to be insensitive to the CE surface areas examined in this study, indicating that the current density at the CE has either negligible or exactly equivalent effect on the reactions at the WE and RE. The former is more likely given the later would require exactly reproducing the cell geometry at each measurement, which is unlikely.

All our experimental results and their interpretation, nevertheless, support that the reaction coinciding with E^*_A and $U(E^*_A)$ on an Ir anode is indeed Reaction (1). This finding provides a well-defined energy level of reference for further thermodynamic analysis of the cathode reaction, described in the following sections.

Cathode behavior

For the cathode, the results and observations presented in Figures 2, 3, 4, 6 and 7 indicate that the faradaic reaction coinciding with E^*_C and $U(E^*_C)$, corresponds to aluminum reduction. Formation of aluminum suboxide gaseous species, e.g. AlO (g) or Al_2O (g), are thermodynamically unfavorable in the temperature range of interest and therefore need not be considered further in this discussion [51]. The electrolysis results demonstrate the reduction reaction sensitivity to the cell voltage U with respect to $U(E^*_C)$, as Al was not detected in the cathode post experiments for $U < U(E^*_C)$. Comparison with the recently assessed phase diagram for Al-Ir presented in Figure 8 indicates that the formation of a solid solution of Al in Ir at moderate concentrations (x_{Al} < 0.15) is possible. Estimates of the diffusion length of Al in the solid cathode for the duration of the measurements (60 s) suggest that Al will not diffuse far into the Ir cathode (< 5 μm) [52]. On the other hand for $U > U(E^*_C)$, the post-quenched cathode contained Al-Ir alloy phases and a morphology comprised of fine lamellae and dendrites indicative of a rapidly solidified liquid, as exemplified in Figure 7. Comparison with Figure 8 confirms the formation of a liquid given the operating temperature ($T \approx$ 2485 K) for the phase compositions observed by EDS (x_{Al} = 0.14 and 0.40). The discrepancy between the measured composition of the Al-rich phase (x_{Al} = 0.40) and that of the minimum solubility limit for the $AlIr_X$ intermetallic compound from Abe et al. [2] (x_{Al} = 0.454) is presumably due to the fine microstructure (< 1 μm) and spatial resolution limits of the analytical technique (EDS, 1 μm, approx.). E^*_C and $U(E^*_C)$ are then hypothesized to coincide with the reduction of Al^{3+} leading to the formation of liquid Al-Ir metal alloy on the Ir cathode

$$\mathrm{Al^{3+}(melt) + 3e^{-}(Ir) = Al(l, Ir)} \quad (11)$$

At isothermal conditions in the measured temperature range (T = 2377 to 2489 K), the liquid metal formation on the Ir cathode at equilibrium conditions (see Figure 8) coincides with the two-phase (liquid and fcc solid solution) region in the Ir-rich portion of the Al-Ir system. For interpretation of E_C^* and $U(E_C^*)$ measurements, E_C^* can be expressed as

$$E_C^* = \phi_C^* - \phi_{ref,C}^*$$

where ϕ_C^* and $\phi_{ref,C}^*$ are respectively the cathode and RE inner potentials during E_C^* measurement. The latter is not necessarily the same as $\phi_{ref,A}^*$ for E_A^* measurements. For $E < E_C^*$, current densities significantly larger than that observed during O_2 gas evolution at and beyond E_A^* were measured, viz. comparing Figure 2 and 3. Such difference in magnitude of current density (6000 mA cm^{-2} vs. 1200 mA cm^{-2}, approx.) shares a candid agreement with the physical nature of the liquid-liquid versus liquid-gas reactions coinciding with E_C^* and E_A^*, resp. However, like for E_A^*, the CE (anode) surface area had negligible influence on E_C^*, as presented in Figure 4.

Although derivation of a model for the fitting parameters of E_C^* is possible, the discussion of the physical significance of β_0 and β_1 will be limited here due to the indefinite nature of the Ir pseudo-reference electrode. The parameter β_0 is associated with the enthalpy change accompanying aluminum reduction, for which the large negative value (β_0 = -2.62 V) agrees with tabulated data [2], [53], [54] at least in sign and order of magnitude. On the other hand, β_1 is related to the entropy change accompanying aluminum reduction and entropy of oxygen at the RE, and a similar agreement is observed for its value (β_1 = 0.966 mV K^{-1}). In contrast to E_A^*, the results for E_C^* do not exhibit clear dependence on $p_{O_2,furnace}$, as shown in Figure 4. This observation suggests that Al (l,Ir) formation at the cathode influences the potential of the reference electrode ϕ_{ref}. Assuming Reaction (5) describes ϕ_{ref} and charge neutrality again limits Al^{3+} and O^{2-} activity variation, a reduction in oxygen potential at the RE (i.e. $p_{O_2,ref}$) is concluded to accompany formation of Al (l,Ir) at the cathode. This phenomenon is hypothesized to occur when Al (l,Ir) is transported from the cathode to be oxidized by dissolved atomic oxygen in the RE vicinity more rapidly than oxygen can be replenished from the anode or furnace atmosphere.

Nevertheless, all our observations and experimental results further support the connection between Reaction (11) and E_C^* and $U(E_C^*)$.

Significance of U^o and thermodynamic analysis

Given the preceding discussion on E_A^* and E_C^*, the definition of U^o can be revisited and its significance discussed. Formally, U^o was defined as the value of $U(E_C^*)$ that satisfies $U(E_C^*) > U(E_A^*)$. Under such conditions, the required current density driving O_2 gas evolution via Reaction (1) on the

anode must have been achieved during measurement of $U(E_C^*)$ coinciding with Reaction (11). Figure 9 is a schematic illustration of the corresponding electrochemical configuration for $U > U(E_C^*) > U(E_A^*)$. Since $U^o = U(E_C^*)$, the postulated state of Al is well defined (see previous section). What remains is a question regarding the state of O_2 (g) at the anode. For bubble formation to occur, neglecting the vapor pressure of species other than O_2 (g), mechanical equilibrium requires that the internal bubble pressure exerted by p_{O_2} at least balances the total external pressure (p_{ext}) exerted on the Al_2O_3 droplet by the furnace gas, i.e. p_{ext} = 0.1 MPa. Assuming zero contact angle, the maximum pressure of O_2 (g) is estimated from the Young-Laplace expression

$$p_{O_2,max} = p_{ext} + \frac{2\gamma}{r} \tag{12}$$

where r and γ are the bubble's radius and surface tension, resp. The relative difference of O_2 (g) chemical potential μ_{O_2} and standard state $\mu_{O_2}^o$ with respect to variation in p_{O_2} is

$$\frac{\mu_{O_2} - \mu_{O_2}^o}{\left|\mu_{O_2}^o\right|} = \frac{RT}{\left|\mu_{O_2}^o\right|}\, ln\left(p_{O_2}\right) \tag{13}$$

At the surface of the droplet, the observed O_2 (g) bubble radii (r) are of the order 250 μm and the surface tension γ of molten Al_2O_3 was previously measured to be approximately 650 mN m^{-1} [27]. Combining these values with Eqs. (12) and (13) and tabulated data for $\mu_{O_2}^o$ [53], μ_{O_2} differs from $\mu_{O_2}^o$ by less than 1%. This remains valid even if the radii of the bubbles were an order of magnitude smaller at the surface of the droplet, i.e. detached bubbles coalesce and grow after leaving the anode surface. Thus, a reasonable assumption is that the energy of O_2 at the anode surface is essentially fixed at the standard state energy $\mu_{O_2}^o$ for $U > U(E_A^*)$ and p_{ext} = 0.1 MPa.

Therefore, U^o is the thermodynamic minimum decomposition potential difference, the minimum electrical work, to drive the overall cell reaction

$$\mathrm{Al_2O_3(l) \rightarrow 2\ Al(l, Ir) + 1.5\ O_2(g, 0.1\ MPa)}$$

with a corresponding Gibbs energy of reaction per mole Al_2O_3 computed via

$$\Delta_r G = 6FU^o = 2\,\mu_{Al(l,Ir)} + 1.5\,\mu_{O_2}^o - \mu_{Al_2O_3}^o \tag{14}$$

where $\mu_{O_2}^o$ and $\mu_{Al_2O_3}^o$ are the standard chemical potentials of O_2 (g) (standard state defined previously) and Al_2O_3 (l) (standard state pure liquid, T and p = 0.1 MPa), resp. and $\mu_{Al(l,Ir)}$, or simply μ_{Al}, is the chemical potential of Al in the two-phase region solid-solution and liquid. Using tabulated data for $\mu_{O_2}^o$ [53] and $\mu_{Al_2O_3}^o$ [54] and measured values for U^o shown in Figure 5, μ_{Al} is determined from the resulting expression derived from Eq. (14)

$$\mu_{Al} = 3FU^o + 0.5\mu_{Al_2O_3}^o - 0.75\,\mu_{O_2}^o \tag{15}$$

The results for μ_{Al} using Eq. (15) are plotted versus temperature in Figure 10. For comparison, the chemical potential of Al for the liquid and fcc solid solution phase equilibrium in the Ir-rich portion of

424 the binary Al-Ir system was also calculated using FactSage™ [51]. Model parameters for this binary
425 equilibrium are from the most recent Al-Ir thermodynamic assessment [2]. The fit of measured values for
426 μ_{Al}, averaging -285.4 kJ mol^{-1} for the measured temperature range (T = 2377 to 2489 K), is less than 7%
427 greater than those calculated using FactSage™. Furthermore, the average entropy $S_{Al,avg}$ for the same
428 temperature range is 114.4 J mol^{-1} K^{-1} which despite a large error (+/-60%) is also in close agreement. As
429 pointed out by Abe et al., no experimental data for the liquid phase was available, and the Gibbs energy
430 model for the liquid phase was fit to available data for the eutectic phase boundary (T = 2245 K) while
431 maintaining ideal entropy of mixing. Given these circumstances, the agreement is remarkable and further
432 supports the validity of the approach and postulated descriptions for Reaction (1), E_A^* and $U(E_A^*)$ as well
433 as Reaction (11), E_C^* and $U(E_C^*)$.
434 Since entropy is proportional to the first derivative of U^o with respect to temperature, errors in
435 the independent measures of the variation of U^o and T are the two most important factors in determining
436 the accuracy for entropy measurements with the proposed approach. The remarkable sensitivity to
437 changes in U^o with temperature variations has been demonstrated by the results presented in Figure 5.
438 Measurements of U^o were repeatable within 5% on average. Furthermore, these values were measured
439 with a precision of around 1 mV. Clearly, the method employed for temperature measurement in this
440 investigation could be refined (see Appendix B). Although, the sensitivity of the impedance-based
441 temperature measurement to tempearture change within the same experiment was quite good (error < 10
442 K); the absolute temperature, used to anchor an experimental dataset, could be determined only within an
443 estimated accuracy of +/-50 K. The latter uncertainty was responsible for the relatively large error on
444 $S_{Al,avg}$. The accuracy of the approach for entropy measurements would therefore benefit from of a
445 secondary means of measuring temperature in situ. Enhancing the accuracy in E_C^* evaluation and the
446 interpretation of the AC current harmonics also calls for development of an electrochemical theory for
447 ACV involving metal deposition on a non-inert substrate.
448
449 **Conclusions**

450 A containerless, pendant droplet technique utilizing a TIF and electrodes for electrochemical
451 study of refractory oxide melts was described. For the first time, the direct electrolytic decomposition of
452 molten Al_2O_3 to O_2 gas and Al metal (alloyed with Ir) was observed, confirming the ionic nature of
453 molten Al_2O_3. The reactions corresponding to oxygen evolution and Al deposition from a single-
454 component electrolyte (Al_2O_3) on an Ir electrode were systematically investigated. The decomposition
455 voltage of molten Al_2O_3 was measured with high precision using ACV, and the results demonstrated
456 remarkable sensitivity to temperature enabling measurement of Gibbs energy and entropy without the use

of a membrane. The chemical potential and entropy of Al in the liquid Al-Ir alloy at the Ir-rich solid-liquid phase boundary was measured for the first time. These results were in remarkably close agreement with the most recent thermodynamic assessment of the Al-Ir system. A significant error for entropy (+/- 60%) persisted due to error in determining absolute temperature. Nevertheless, these results have illustrated a viable pathway for measuring chemical potential and entropy at UHT in refractory melts by combining the enhanced sensitivity of ACV and flexibility of containerless processing by pendant droplet technique.

Acknowledgements

The authors thank Dr. Guillaume Lambotte and Ms. Sara Warkander for their pioneering effort to implement electrochemical measurements in the TIF furnace. The authors also gratefully wish to acknowledge contributions from Ms. Melody Wang, Mr. Erick I. Hernandez and Prof. Joseph Checkelsky. This research was funded by the US Office of Naval Research (ONR) under grant Contract # N00014-11-1-0657.

References

[1] J. Sato, T. Omori, K. Oikawa, I. Ohnuma, R. Kainuma, and K. Ishida, "Cobalt-base high-temperature alloys," *Science*, vol. 312, no. 5770, pp. 90–91, 2006.

[2] T. Abe, C. Kocer, M. Ode, H. Murakami, Y. Yamabe-Mitarai, K. Hashimoto, and H. Onodera, "Thermodynamic re-assessment of the Al-Ir system," *Calphad*, vol. 32, no. 4, pp. 686–692, 2008.

[3] A. Allanore, "Features and challenges of molten oxide electrolytes for metal extraction," *J. Electrochem. Soc.*, vol. 162, no. 1, pp. 13–22, 2014.

[4] M. Zinkevich, "Thermodynamics of rare earth sesquioxides," *Prog. Mater. Sci.*, vol. 52, no. 4, pp. 597–647, 2007.

[5] S. V. Ushakov and A. Navrotsky, "Experimental approaches to the thermodynamics of ceramics above 1500°C," *J. Am. Ceram. Soc.*, vol. 95, no. 5, pp. 1463–1482, 2012.

[6] H. L. Lukas, S. G. Fries, and B. Sundman, *Computational Thermodynamics*. New York: Cambridge University Press, 2007.

[7] O. Kubaschewski, C. B. Alcock, and P. J. Spencer, *Materials Thermochemistry*, 6th ed. Oxford: Pergamon Press Ltd, 1993.

[8] E. E. Shpil'rain, D. N. Kagan, and L. S. Barkhatov, "Thermodynamic properties of the condensed phase of alumina near the melting point," *High Temp.-High Press.*, vol. 4, no. 6, pp. 605–609, 1972.

[9] S. V. Ushakov and A. Navrotsky, "Direct measurements of fusion and phase transition enthalpies in lanthanum oxide," *J. Mater. Res.*, vol. 26, no. 7, pp. 845–847, 2011.

[10] S. Ansell, S. Krishnan, J. K. R. Weber, J. Felten, P. Nordine, M. Beno, D. Price, and M.-L. Saboungi, "Structure of liquid aluminum oxide," *Phys. Rev. Lett.*, vol. 78, no. 3, pp. 464–466,

1997.

[11] L. B. Skinner, A. C. Barnes, P. S. Salmon, L. Hennet, H. E. Fischer, C. J. Benmore, S. Kohara, J. K. R. Weber, A. Bytchkov, M. C. Wilding, J. B. Parise, T. O. Farmer, I. Pozdnyakova, S. K. Tumber, and K. Ohara, "Joint diffraction and modeling approach to the structure of liquid alumina," *Phys. Rev. B*, vol. 87, no. 2, p. 24201, 2013.

[12] H. Itoh, S. Akira, M. Takashi, and Y. Toshio, "Electromotive-force measurements of molten oxide mixtures," *J. Chem. Soc.*, vol. 80, pp. 473–487, 1984.

[13] R. O. Colson, "In situ voltammetric observation of transitions above the liquidus in silicate melts," *Contrib. Mineral. Petr.*, vol. 159, no. 5, pp. 703–717, 2009.

[14] R. O. Colson, A. M. Floden, T. R. Haugen, K. M. Malum, M. Sawarynski, M. K. B. Nermoe, K. E. Jacobs, and D. Holder, "Activities of NiO, FeO, and O2− in silicate melts," *Geochim. Cosmochim. Acta*, vol. 69, no. 12, pp. 3061–3073, 2005.

[15] K. Takahashi and Y. Miura, "Electrochemical behavior of glass melts," *J. Non. Cryst. Solids*, vol. 96, pp. 119–130, 1987.

[16] Y. Miura, Y. Akiyama, and K. Takahashi, "Electrolysis of molten sodium borate glasses," *J. Ceram. Soc. Jpn.*, vol. 94, no. 4, pp. 425–431, 1986.

[17] K. Kawamura and T. Yokokawa, "Linear sweep voltammetry of Pb2+/Pb in oxide melts," *J. Electrochem. Soc.*, vol. 135, no. 6, pp. 1447–1451, 1988.

[18] A. Sasahira, K. Kawamura, M. Shimizu, N. Takada, M. Hongo, and T. Yokokawa, "Pb2+/Pb redox equilibria in sodium borate, silicate, and aluminosilicate melts," *J. Electrochem. Soc.*, vol. 136, no. 7, pp. 1861–1864, 1989.

[19] P. F. Paradis, T. Ishikawa, G. W. Lee, D. Holland-Moritz, J. Brillo, W. K. Rhim, and J. T. Okada, "Materials properties measurements and particle beam interactions studies using electrostatic levitation," *Mater. Sci. Eng. R*, vol. 76, no. 1, pp. 1–53, 2014.

[20] J. K. R. Weber, A. Tamalonis, C. J. Benmore, O. L. G. Alderman, S. Sendelbach, A. Hebden, and M. A. Williamson, "Aerodynamic levitator for in situ x-ray structure measurements on high temperature and molten nuclear fuel materials," *Rev. Sci. Instrum.*, vol. 87, no. 7, p. 73902, 2016.

[21] J. E. Enderby, S. Ansell, S. Krishnan, and D. L. Price, "The electrical conductivity of levitated liquids," *Appl. Phys. Lett.*, vol. 71, no. 1, pp. 116–119, 1997.

[22] Y. Arai, P.-F. Paradis, T. Aoyama, T. Ishikawa, and S. Yoda, "An aerodynamic levitation system for drop tube and quenching experiments," *Rev. Sci. Instrum.*, vol. 74, no. 2, pp. 1057–1063, 2003.

[23] E. G. Lierke, "Acoustic levitation - a comprehensive survey of principles and applications," *Acustica*, vol. 82, no. 2, pp. 220–237, 1996.

[24] D. Langstaff, M. Gunn, G. N. Greaves, A. Marsing, and F. Kargl, "Aerodynamic levitator furnace for measuring thermophysical properties of refractory liquids," *Rev. Sci. Instrum.*, vol. 84, no. 12, p. 124901, 2013.

[25] L. B. Skinner, C. J. Benmore, J. K. R. Weber, M. A. Williamson, A. Tamalonis, A. Hebden, T. Wiencek, O. L. G. Alderman, M. Guthrie, L. Leibowitz, and J. B. Parise, "Molten uranium dioxide structure and dynamics," *Science*, vol. 346, no. 6212, pp. 984–987, 2014.

[26] L. B. Skinner, C. J. Benmore, J. K. R. Weber, J. Du, J. Neuefeind, S. K. Tumber, and J. B. Parise, "Low cation coordination in oxide melts," *Phys. Rev. Lett.*, vol. 112, p. 157801, 2014.

[27] P. F. Paradis and T. Ishikawa, “Surface tension and viscosity measurements of liquid and undercooled alumina by containerless techniques,” *Jpn. J. Appl. Phys. 1*, vol. 44, no. 7A, pp. 5082–5085, 2005.

[28] P. F. Paradis, T. Ishikawa, Y. Saita, and S. Yoda, “Non-contact thermophysical property measurements of liquid and undercooled alumina,” *Jpn. J. Appl. Phys. 1*, vol. 43, no. 4A, pp. 1496–1500, 2004.

[29] M. R. Null and W. W. Lozier, “Carbon arc image furnaces,” *Rev. Sci. Instrum.*, vol. 29, no. 2, pp. 163–170, 1958.

[30] R. E. De La Rue and F. A. Halden, “Arc-image furnace for growth of single crystals,” *Rev. Sci. Instrum.*, vol. 31, no. 1, pp. 35–38, 1960.

[31] R. P. Poplawsky and J. E. Thomas, “Floating zone crystals using an arc image furnace,” *Rev. Sci. Instrum.*, vol. 31, no. 12, pp. 1303–1308, 1960.

[32] W. G. Field and R. W. Wagner, “Thermal imaging for single crystal growth and its application to ruby,” *J. Cryst. Growth*, vol. 4, pp. 799–803, 1968.

[33] K. Kitazawa, K. Nagashima, T. Mizutani, K. Fueki, and T. Mukaibo, “A new thermal imaging system utilizing a Xe arc lamp and ellipsoidal mirror for crystallization of refractory oxides,” *J. Cryst. Growth*, vol. 39, pp. 211–215, 1977.

[34] J. J. Diamond and A. L. Dragoo, “Studies of molten alumina in the arc-image Furnace,” *Rev. Hautes Temp. Refract.*, vol. 3, no. 3, pp. 273–279, 1966.

[35] K. Eickhoff and K. Gürs, “Tiegelfreies zonenschmelzen von rubinkristallen durch aufheizen der schmelzzone mittels laser,” *J. Cryst. Growth*, vol. 6, pp. 21–25, 1969.

[36] D. B. Gasson and B. Cockayne, “Oxide crystal growth using gas lasers,” *J. Mater. Sci.*, vol. 5, no. 2, pp. 100–104, 1970.

[37] L. S. Nelson, N. L. Richardson, K. Keil, and S. R. Skaggs, “Effects of oxygen and argon atmospheres on pendant drops of aluminum-oxide melted with carbon-dioxide laser radiation,” *High Temp. Sci.*, vol. 5, no. 2, pp. 138–154, 1973.

[38] S. Krishnan, J. K. R. Weber, R. A. Schiffman, P. C. Nordine, and R. A. Reed, “Refractive index of liquid aluminum oxide at 0.6328 μm,” *J. Am. Ceram. Soc.*, vol. 74, no. 4, pp. 881–883, 1991.

[39] T. Katsumata, T. Shiina, M. Shibasaki, and T. Matsuo, “Electrical measurements on molten TiO2 using a floating zone furnace,” *J. Cryst. Growth*, vol. 239, pp. 1791–1796, 2002.

[40] “Standard test methods for apparent porosity, liquid absorption, apparent specific gravity, and bulk density of refractory shapes by vacuum pressure,” *ASTM Standard C830-00 (2011)*. ASTM International, West Conshohocken, PA, 2011.

[41] S. W. Hughes, “Archimedes revisited: a faster, better, cheaper method of accurately measuring the volume of small objects,” *Phys. Educ.*, vol. 40, no. 5, pp. 468–474, 2005.

[42] S. Sokhanvaran, S.-K. Lee, G. Lambotte, and A. Allanore, “Electrochemistry of molten sulfides: copper extraction from BaS-Cu2S,” *J. Electrochem. Soc.*, vol. 163, no. 3, pp. D115–D120, 2016.

[43] A. M. Bond, D. Elton, S. X. Guo, G. F. Kennedy, E. Mashkina, A. N. Simonov, and J. Zhang, “An integrated instrumental and theoretical approach to quantitative electrode kinetic studies based on large amplitude Fourier transformed a.c. voltammetry: A mini review,” *Electrochem. Commun.*, vol. 57, pp. 78–83, 2015.

[44] D. J. Gavaghan and A. M. Bond, “A complete numerical simulation of the techniques of alternating current linear sweep and cyclic voltammetry: analysis of a reversible process by conventional and fast Fourier transform methods,” *J. Electroanal. Chem.*, vol. 480, no. 1–2, pp. 133–149, 2000.

[45] S. O. Engblom, J. C. Myland, and K. B. Oldham, “Must ac voltammetry employ small signals?,” *J. Electroanal. Chem.*, vol. 480, no. 1–2, pp. 120–132, 2000.

[46] A. Allanore, L. Yin, and D. R. Sadoway, “A new anode material for oxygen evolution in molten oxide electrolysis.,” *Nature*, vol. 497, no. 7449, pp. 353–6, 2013.

[47] H. Kim, J. Paramore, A. Allanore, and D. R. Sadoway, “Electrolysis of molten iron oxide with an iridium anode: the role of electrolyte basicity,” *J. Electrochem. Soc.*, vol. 158, no. 10, pp. E101–E105, 2011.

[48] M. S. Chandrasekharaiah, M. D. Karkhanavala, and S. N. Tripathi, “The pressure of iridium oxides over iridium at high temperatures in 1 atm of dry oxygen,” *J. Less-Common Met.*, vol. 80, no. 1, 1981.

[49] D. Wang, A. J. Gmitter, and D. R. Sadoway, “Production of Oxygen Gas and Liquid Metal by Electrochemical Decomposition of Molten Iron Oxide,” *J. Electrochem. Soc.*, vol. 158, no. 6, pp. E51–E54, 2011.

[50] C. H. P. Lupis, *Chemical Thermodynamics of Materials*. New York: North-Holland, 1983.

[51] C. W. Bale, E. Bélisle, P. Chartrand, S. A. Decterov, G. Eriksson, A. E. Gheribi, K. Hack, I. H. Jung, Y. B. Kang, J. Melançon, A. D. Pelton, S. Petersen, C. Robelin., J. Sangster, and M.-A. Van Ende, “FactSage thermochemical software and databases, 2015-2016,” *Calphad*, vol. 54, pp. 35–53, 2016.

[52] A. M. Brown and M. F. Ashby, “Correlations for diffusion constants,” *Acta Metall.*, vol. 28, no. 8, pp. 1085–1101, 1980.

[53] D. R. Stull and H. Prophet, “JANAF thermochemical tables,” *J. Phys. Chem. Ref. Data*, 1985.

[54] M. W. Chase, J. L. Curnutt, A. T. Hu, H. Prophet, A. N. Syverud, and L. C. Walker, “JANAF thermochemical tables, 1974 supplement,” *J. Phys. Chem. Ref. Data*, vol. 3, no. 2, pp. 311–480, 1974.

[55] M. E. Orazem and B. Tribollet, *Electrochemical Impedance Spectroscopy*. Hoboken: John Wiley & Sons, Inc., 2008.

[56] A. E. van Arkel, E. A. Flood, and N. F. H. Bright, “The electrical conductivity of molten oxides,” *Can. J. Chem.*, vol. 31, no. 11, p. 1009, 1953.

[57] H. Fay, “The electrical conductivity of liquid Al2O3 (molten corundum and ruby),” *J. Phys. Chem.*, vol. 70, no. 3, pp. 890–893, 1966.

[58] V. P. Elyutin, B. S. Mitin, and Y. A. Nagibin, “Electrical conductivity of molten aluminum oxide,” *Izv. Akad. Nauk SSSR, Neorg. Mater.*, vol. 7, no. 5, pp. 880–881, 1971.

[59] V. I. Aleksandrov, V. V. Osiko, and V. M. Tatarintsev, “Electrical conductivity of aluminum oxide in the molten state,” *Izv. Akad. Nauk SSSR, Neorg. Mater.*, vol. 8, no. 5, pp. 956–957, 1972.

[60] E. E. Shpil’rain, D. N. Kagan, L. S. Barkhatov, and L. I. Zhmakin, “Experimental study of specific electrical conductivity of molten aluminum oxide at temperature up to 3000 K,” *Teplofiz. Vys. Temp.*, vol. 14, no. 5, pp. 948–952, 1976.

[61] B. Glorieux, M.-L. Saboungi, F. Millot, J. Enderby, and J.-C. Rifflet, “Aerodynamic levitation: an approach to microgravity,” *AIP Conf. Proc.*, vol. 552, pp. 316–324, 2001.

[62] M. L. Saboungi, J. Enderby, B. Glorieux, H. Schnyders, Z. Sungaila, S. Krishnan, and D. L. Price, “What is new on the levitation front?,” *J. Non. Cryst. Solids*, vol. 312–314, pp. 294–298, 2002.

[63] A. N. Shatunov, A. I. Maksimov, A. Y. Pechenkov, and I. V. Poznyak, “Method of electrical resistivity measurement for high-temperature melts,” *Inorg. Mater.*, vol. 47, no. 14, pp. 1579–1583, 2011.

[64] S. J. Schneider, “Cooperative determination of the melting point of alumina,” *Pure Appl. Chem.*, vol. 21, p. 115, 1970.

[65] R. E. Bedford, G. Bonnier, H. Maas, and F. Pavese, “Recommended values of temperature on the International Temperature Scale of 1990 for a selected set of secondary reference points,” *Metrologia*, vol. 33, pp. 133–154, 1996.

[66] F. Henning and H. T. Wensel, “The freezing point of iridium,” *Bur. Stand. J. Res.*, vol. 10, no. 6, pp. 809–821, 1933.

[67] E. Thibodeau and I. H. Jung, “A structural electrical conductivity model for oxide melts,” *Metall. Mater. Trans. B*, vol. 47, no. 1, pp. 355–383, 2016.

Appendix A

Impedance Measurements

A typical open-circuit Nyquist plot is shown in Figure A1. The magnitude of the impedance $|Z|$ decreases with decreasing frequency f = 200 kHz to 15 kHz with little variation in the real component of impedance Z_{Re}, attendant behavior of the electrode lead inductance. At around f = 15 kHz, the impedance crosses a point in which the imaginary component of impedance Z_{Im} is zero, the marked "X" in Figure A1. As f is further decreased from 15 kHz to 5 Hz, $|Z|$ continues to increase with an approximately unity slope. At low frequencies, $|Z|$ approaches an asymptotic value and Z_{Im} approaches zero.

A model of the equivalent circuit (also shown in Figure A1) was used to fit the data and estimate values for the circuit elements. The external inductance L_{ext} was estimated by a separate measurement of the impedance of the shorted leads in the TIG-welded electrode configuration and was arbitrarily fixed during the fitting along with the charge transfer resistance R_{ct}, which was taken as a negligibly small value (10^{-8} ohms). This is a reasonable assumption given the UHT's and relatively fast kinetics anticipated for the faradaic reaction controlling the impedance at open circuit. A generalized finite Warburg element (GFW) was taken as the element descriptive of mass transfer of the electroactive species. The GFW impedance (Z_W) is given by [55]

$$Z_W = R_W \frac{\tanh[(\mathrm{i}T_W\omega)^{P_W}]}{(\mathrm{i}T_W\omega)^{P_W}}$$

where $\omega = 2\pi f$, $\mathrm{i} = \sqrt{-1}$, and R_W, T_W and P_W are fitting parameters. The results for R_u, C_{dl}, R_W, T_W and P_W are presented in Table A1. Temperature was estimated based upon variations of R_u with P_L (as described in Appendix B).

Appendix B

Temperature Measurement

Temperature (T) was evaluated from changes to the solution resistance with lamp power (P_L). The solution resistance (R_s) can be calculated by

$$R_s = R_u - R_{ext}$$

where R_u is the uncompensated resistance evaluated from open circuit EIS measurements, and R_{ext} is the external resistance between the Ir electrode-electrolyte interface and potentiostat. R_{ext} was determined as a function of P_L by measuring the impedance of the shorted loop in the TIG-welded electrode configuration. R_{ext} was found to be a weakly increasing function of P_L, which is expected of a metallic conductor. The relation between R_s and conductivity (σ) of the electrolyte is given by

$$R_s = \frac{G}{\sigma}$$

where the geometric factor (G) depends upon factors such as electrode configuration in the droplet and droplet size. Assuming σ obeys an Arrhenius dependence with respect to temperature, then

$$\sigma = \sigma_0 \exp(-E_\sigma / k_B T) \quad \text{(B1)}$$

where σ_0 is the Arrhenius pre-exponential factor, E_σ is the activation energy of conductivity and k_B is the Boltzmann constant. If E_σ and σ_0 are assumed to be constants in the temperature range of interest, then the following relation applies

$$T = \left[\frac{1}{T_0} + \frac{k_B}{E_\sigma}\left\{\ln\left(\frac{G_o}{G}\right) + \ln\left(\frac{R_s}{R_{s,0}}\right)\right\}\right]^{-1} \quad \text{(B2)}$$

which connects R_s measured at an unknown T and the solution resistance ($R_{s,0}$) measured at a reference temperature (T_0). Several workers reported measurements of σ for Al_2O_3 (l) as a function of T in the literature [21], [56]–[63]. A critical assessment of these results in the temperature range $T_m(Al_2O_3)$ = 2327 K [64], [65] to T_m(Ir) = 2719 K [65], [66] is provided in Appendix C, yielding E_σ = 1.67 +/- 0.15 eV. At the minimum P_L required for electrodes' insertion into the droplet, this condition is assigned the temperature T_0 = 2377 K, a 50 K superheat above $T_m(Al_2O_3)$. The error associated with T_0 is estimated to be 50 K. This assumption is expected to be reasonable considering the vicinity of the droplet to the solid-liquid interface and temperature measurements during other experiments with a nearby thermocouple.

Taking geometric effects into account, the perpendicular distance between wires in the droplet varies by a negligible amount over the course of an experiment, so only the effective area (A_e) described by an effective radius (r_e) can influence G, and the following approximate relation applies

$$\frac{G_o}{G} \approx \frac{A_e}{A_{e,o}} \approx \left(\frac{r_e}{r_{e,o}}\right)^2$$

Where G_o, $A_{e,o}$ and $r_{e,o}$ are the geometric constant, effective area and radius, resp., at the reference temperature T_o. Assuming the behavior of r_e varies similarly to the droplet radius (r) and only moderate changes to P_L ($\Delta P_L = P_L - P_{L,o}$ < 5% for lamp power $P_{L,o}$ at T_o), the Taylor series expansion applies (neglecting second and higher order terms)

$$\frac{r_e}{r_{e,o}} \sim 1 + \frac{1}{r_o}\frac{dr}{dP_L}\Delta P_L$$

where r_o is the droplet radius at T_o. By comparing images of the droplet at various lamp powers with image analysis software, the approximate relation $\frac{1}{r_o}\frac{dr}{dP_L} = \frac{0.02}{P_L}$ was determined valid for all experiments.

Considering only errors associated with E_σ and T_0 and neglecting all other contributions, the error with respect to measurement of the variation in temperature within the same experiment is less than 10 K. However, as decribed earlier, the error for absolute temperature is estimated to be 50 K.

Appendix C

Assessment of Al_2O_3 conductivity

Previous efforts to measure the electrical conductivity of Al_2O_3 (l) are numerous [21], [56]–[63], which is uncommon for refractory melts. Although recent researchers have compared their results with a partial selection of previous efforts, the last complete review of Al_2O_3 (l) conductivity is that of Shpil'rain et al. [60]. More recent reviews, e.g. [67], have omitted without justification contributions from the aerodynamic levitation method [21], [61], [62]. Thus, an updated review of Al_2O_3 (l) conductivity is prudent. Substantial disagreement exists, given the errors reported, along with the effect of atmosphere (oxygen potential). The atmosphere employed is noted where possible, but its effect is neglected in the current assessment. Careful study of the effect of impurities and atmosphere (oxygen potential) would help resolve the discrepancies. A summary of previous measurements and the results of this assessment in the temperature range range $T_m(Al_2O_3)$ = 2327 K [64], [65] to T_m(Ir) = 2719 K [65], [66] are presented in Figure C1.

Van Arkel et al. [56] were the first to report the conductivity of Al_2O_3 (l). Their estimate, 15 S cm^{-1}, was derived indirectly from the performance of an electric arc above Al_2O_3 (l) in an electric arc furnace. They assigned an error of at least 50% owing to the approximate nature of their calculations. For this reason, this result was not included in this assessment.

Fay [57] reported conductivity at 2400 K to be 3.84 S cm^{-1} with an estimated error of 5% using the two concentric electrode technique with an Ir electrode and crucible. The atmosphere was air, but the heat source was an oxygen-hydrogen flame that Fay conceded likely made the atmosphere reducing. Temperature was measured with an optical pyrometer pointed at the melt, but the author assumed unity emittance, so T = 2400 K represents a slight underestimate of the actual temperature.

Elyutin et al. [58] used the two electrode technique with induction heating from $T = T_m(Al_2O_3)$ to 2800 K. They found that conductivity varied from 0.71 S cm^{-1} at 2325 K to 1.26 S cm^{-1} at 2775 K with 11% estimated error. At the same temperatures, they reported, for the first time, the activation energy varied from E_σ = 0.89 eV to 0.60 eV. Helium and vacuum atmospheres were used with no apparent effect on conductivity. Later, Shpil'rain et al. first questioned the induction heater's electromagnetic field on the results, which might at least partially explain why Elyutin et al.'s results are an order of magnitude lower the other reports. For these reasons, these results were not included in this assessment.

Aleksandrov et al. [59] used the two electrode method with an inductively-heated cold crucible from $T = T_m(Al_2O_3)$ to 2473 K. They measured 10 S cm^{-1} with a reported error of 3% and no temperature dependency. The atmosphere was air. Later, Shpil'rain et al. [60] suggested that the error was probably

much greater than this given the significant temperature gradients likely present in the melt. For this reason, this result was not included in this assessment.

Shpil'rain et al. [60] used the two concentric electrode technique from $T = T_m(Al_2O_3)$ to 3000 K with an estimated error of 10%. The atmosphere was either pure Ar or vacuum, and conductivity was exactly the same in both atmospheres. Mo and W electrodes were employed with Mo and W crucibles, resp. Temperature was measured by an optical pyrometer using a black body cavity in the crucibles. They reported E_σ varied from 1.85 eV at 2400 K to 0.93 eV at 3000 K.

Enderby et al. [21] measured conductivity at a single temperature near $T_m(Al_2O_3)$ to be 6 S cm^{-1} with 15% error using the contactless radio frequency resonator technique (RFR) coupled with aerodynamic levitation. The atmospheric composition was not reported. A pyrometer is shown in the schematic of the setup, but no temperature was reported. Glorieux et al. and Saboungi et al. report suspiciously similar values at the $T_m(Al_2O_3)$. However, since no temperature was reported in [21], this common value from [21], [61], [62] was not included in this assessment.

Continuing measurements by contactless RFR coupled with aerodynamic levitation, Glorieux et al. [61] reported measurements extending from under-cooled liquid at T = 2000 K to 3300 K with an estimated accuracy of 15%. Here, they calibrated a pyrometer for temperature measurement using the thermal arrest upon melting. They mentioned that Ar and O_2 gas compositions were used, but do not specify which data points correspond to which gas environments.

Further continuing measurements by contactless RFR coupled with aerodynamic levitation, Saboungi et al. [62] report the conductivity as a function of temperature with an error of 15%. They mention that the levitation gas composition had an influence on the conductivity. However, the exact numerical change in conductivity, nor the atmospheric compositions (presumably Ar and O_2 as reported in [61]) used during measurements were not reported. No effort was made to explain the details for temperature measurement (emittance, etc.), but it can be assumed they calibrated the pyrometer using melting thermal arrest as described in [61].

More recently, Shatunov et al. [63] reported conductivity by energy balance considerations using an induction-heated cold crucible in air. They reported 0.47 S cm^{-1} to 1.64 S cm^{-1} with 17% estimated error for T = 2573 K to 3223 K. Their results are substantially lower than that of all previous measurements, which they attributed to impurities and atmosphere (oxygen potential). Given the significant difference from previous reports, the validity of this justification requires more evidence. They did not report the purity of the samples used in their experiments, nor the method of pyrometer calibration. Additionally, temperature appears to have been measured only at the top surface of melt. Furthermore, given the indirect nature of the methodology, this approach measures an effective conductivity for the entire crucible charge, in which substantial temperature gradients were present (> 100

763 K cm^{-1}). No effort was made to explain the contribution of this effect on their results. For these reasons,
764 the single data point in the desired temperature range was not included in this assessment.
765
766 **Appendix D**
767 *Influence of cell geometry on $U(E_A^*)$ and $U(E_C^*)$*
768 The DC current (I) is related to the DC current density (j) by the electroactive surface area (A)
769 according to
770 $$I = Aj \tag{D1}$$
771 Assuming that the cell voltage (U) is a monotonically increasing function of I, then the condition for
772 $U^o \equiv U(E_C^*)$, i.e. $U(E_C^*) > U(E_A^*)$, can be rewritten as
773 $$I(E_C^*) > I(E_A^*) \tag{D2}$$
774 where $I(E_C^*)$ and $I(E_A^*)$ are the DC current magnitudes occurring at $U = U(E_C^*)$ and $U(E_A^*)$, resp.
775 Substituting Eq. (D1) into (D2),
776 $$A_C j(E_C^*) > A_A j(E_A^*) \tag{D3}$$
777 Where A_C (A_A) is the cathode (anode) electroactive surface area and $j(E_C^*)$ ($j(E_A^*)$) is the DC current
778 density magnitude at the cathode (anode) concomitant with potential E_C^* (E_A^*). Rearranging (D3), and
779 assuming $\frac{A_C}{A_A} = \frac{A_{G,C}}{A_{G,A}}$ yields
780 $$\frac{A_{G,C}}{A_{G,A}} > \frac{j(E_A^*)}{j(E_C^*)} \tag{D4}$$
781 In practice, Eq. (D4) was satisfied for $\frac{A_{G,C}}{A_{G,A}} > 0.5$ and 0.3 for Gases A and C, resp.
782
783

Tables, Figures and Captions

Table 1. List of symbols, definitions and SI units or values.

Symbol	Name	SI unit or value
a_i	activity of species i	
A	area	m^2
A_G	geometric surface area	m^2
β_n	fitting parameter of order n	varies
C_{dl}	double-layer capacitance	F
$Ø$	diameter	m
E	electrode potential	V
E_A (E_C)	anode (cathode) potential	V
E_{ac}	applied potential AC amplitude	V
E_{oc}	open circuit potential	V
E_σ	Arrhenius activation energy of conductivity	eV
f	frequency	Hz
F	Faraday constant	96,485 C mol^{-1}
$\Delta_r G$	reaction Gibbs energy	J mol^{-1}
G	geometric factor	m^{-1}
γ	surface tension	N m^{-1}
$\mathbf{i}$	imaginary unit	$\sqrt{-1}$
I	electric current	A
$I_{n\omega}$	n^{th} harmonic of electric current	A
j	electric current density	A m^{-2}
k_B	Boltzmann constant	8.617 eV K^{-1}
L_{ext}	external inductance	H
μ_i	chemical potential	J mol^{-1}
μ_i^o	standard chemical potential	J mol^{-1}
ν	potential scan rate	V s^{-1}
ω	angular frequency	rad s^{-1}
ϕ	inner electric potential	V
p	pressure	Pa
p_i	partial pressure of species i	Pa
P_L	relative lamp power	%
P_W	generalized finite Warburg element (GFW) fitting parameter	
Q	electric charge	C
r	radius	m
R	gas constant	8.314 J mol^{-1} K^{-1}
R_c	compensated resistance	Ω
R_{ct}	charge transfer resistance	Ω
R_{cell}	cell resistance	Ω
R_{ext}	external resistance	
R_s	solution resistance	Ω
R_u	uncompensated resistance	Ω
R_W	GFW fitting parameter	Ω
σ	conductivity	S m^{-1}
σ_o	Arrehnius pre-exponential factor of conductivity	S m^{-1}
S	entropy	J K^{-1}
S_i	partial molar entropy	J mol^{-1} K^{-1}
t	time	s
T	temperature	K
T_m	melting point	K
T_W	GFW fitting parameter	s

U	cell voltage	V
x_i	mole fraction of species i	
Z	impedance	Ω
Z_{im}	imaginary component of impedance	Ω
Z_{re}	real component of impedance	Ω

787

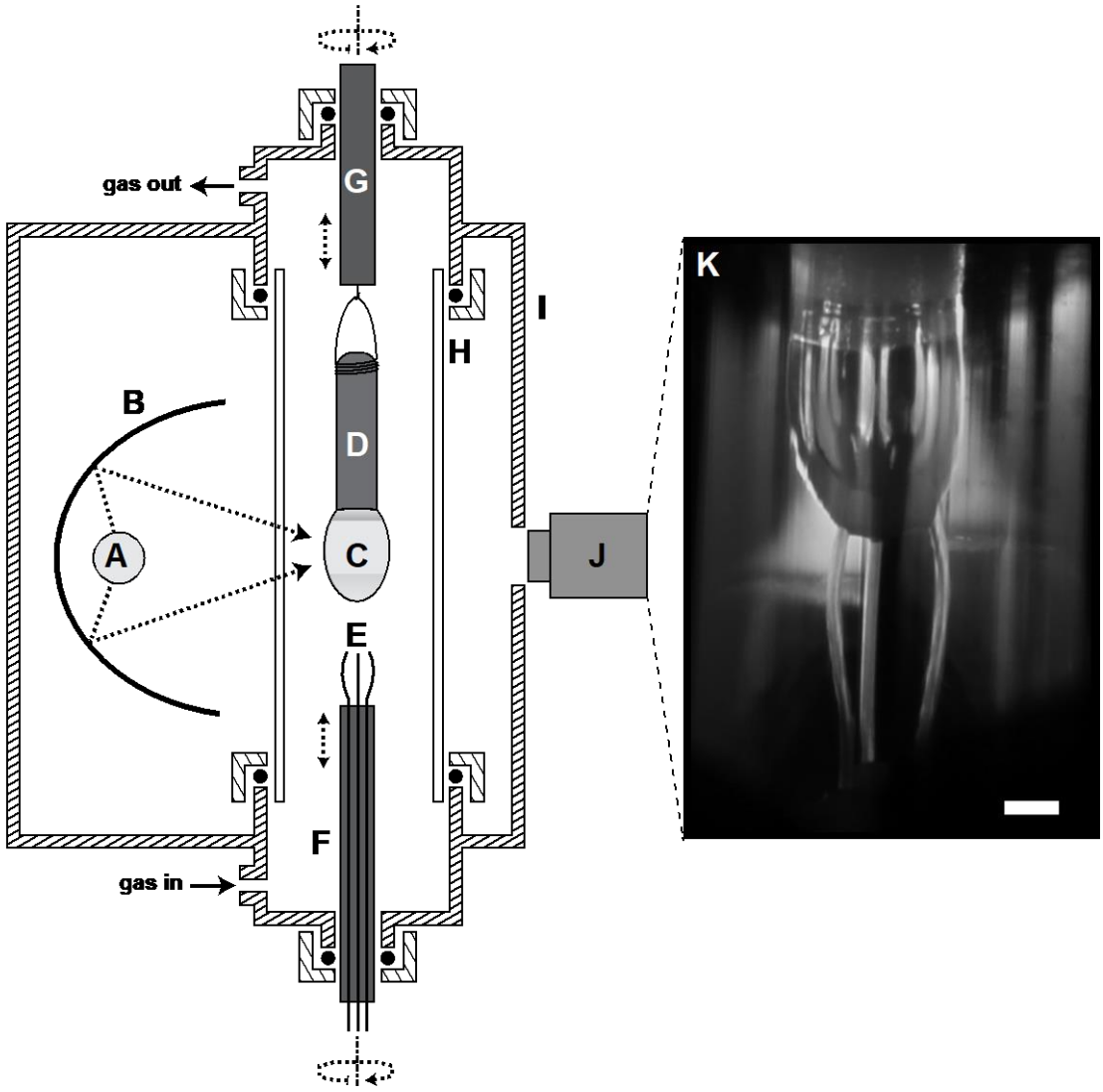

788

789 Figure 1. Schematic of the experimental setup (not to scale): (A) Xe lamp and (B) ellipsoidal mirror (one
790 of four pairs shown), (C) molten pendant droplet (0.1 mL volume, typically) in the hot zone, (D) solid
791 sample rod suspended by wire loop, (E) electrodes, (F) electrode leads and lower shaft, (G) upper shaft,
792 (H) quartz tube, (I) furnace shell, (J) camera, and (K) photograph of Ir electrodes inserted into a molten
793 Al_2O_3 droplet (scale bar 2 mm).

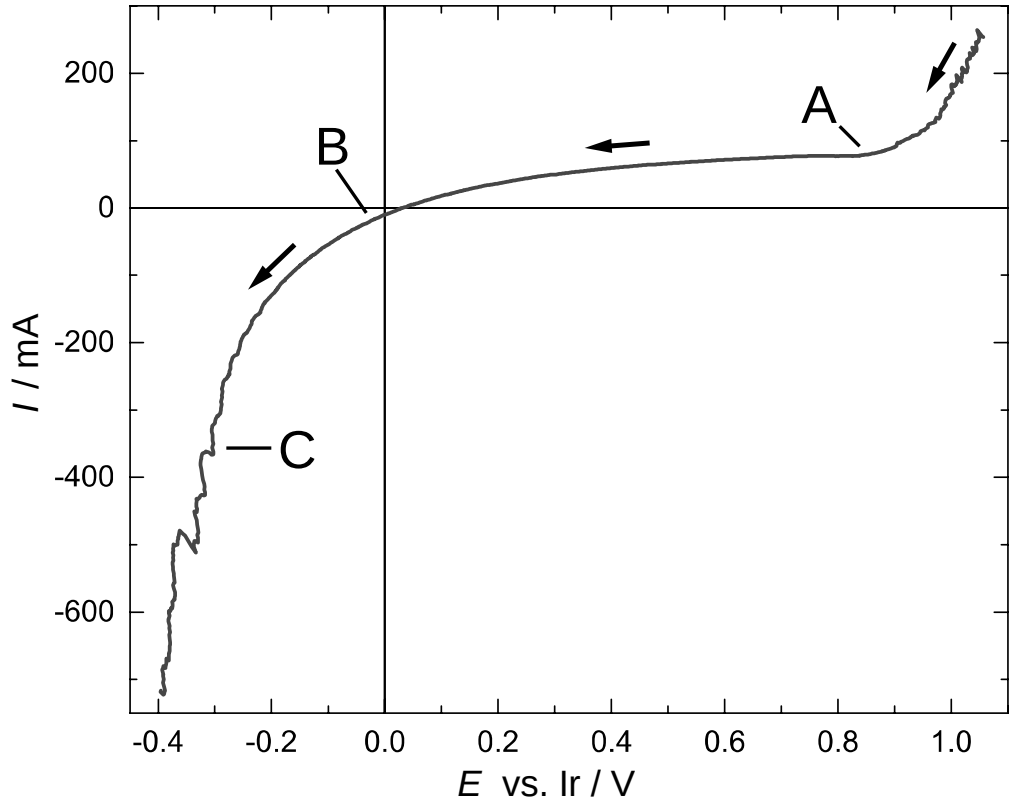

794

795 Figure 2. Typical DC voltammogram for Ir in Al_2O_3 (l) recorded in TIF I. Potential scan limits: 1.05 to -

796 0.40 V vs. Ir, scan rate ν = 250 mV s^{-1}, T = 2377 K, Gas B, geometric surface areas for WE ($A_{G,WE}$) and

797 CE ($A_{G,CE}$) were approximately 0.07 and 0.13 cm^2, resp.

798

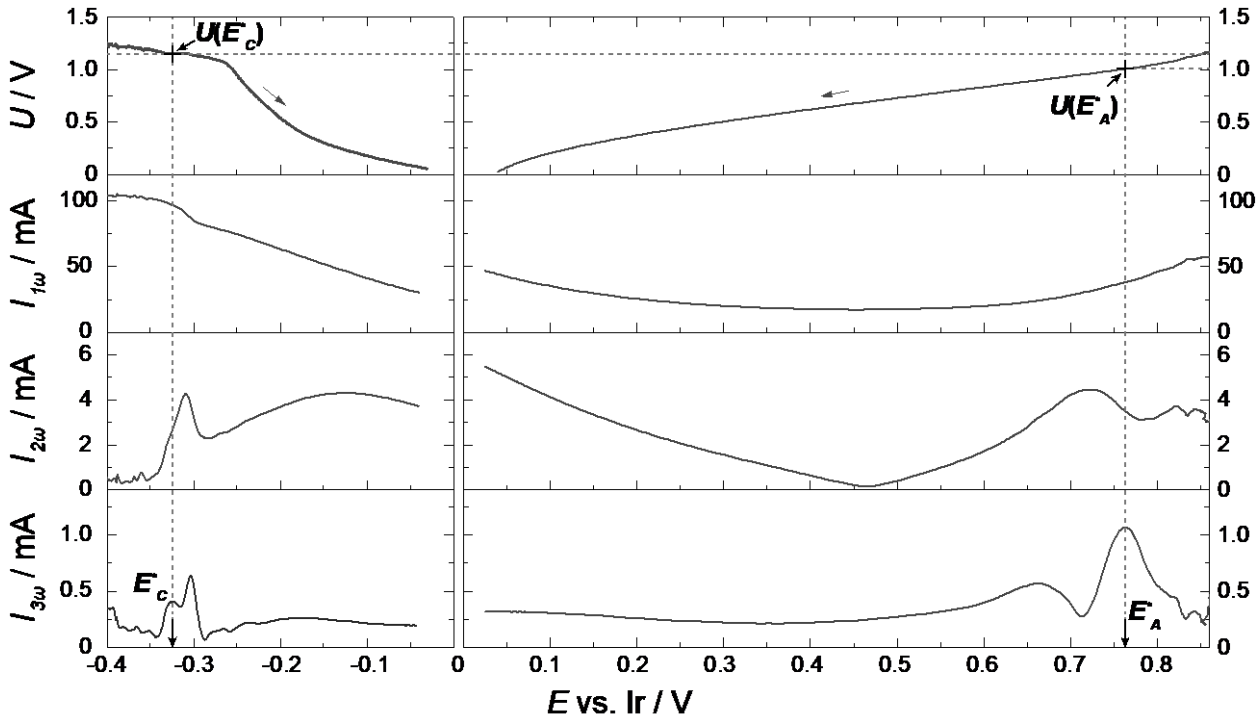

Figure 3. From top to bottom panel, DC component of cell voltage and first, second and third harmonic current responses obtained during ACV measurements. $E < 0$ corresponds to cathodic polarization study (cathode geometric surface area $A_{G,C}$ = 0.07 cm^2, applied DC potential scan limits -0.55 to 0 V vs. Ir); while $E > 0$ is an anodic polarization study (anode $A_{G,A}$ = 0.13 cm^2, +0.95 to 0 V vs. Ir). For both, E_{ac} = 120 mV, f = 23 Hz, ν = 20 mV s^{-1}, T = 2377 K and Gas A. The quantities $U(E_C^*)$, E_C^*, $U(E_A^*)$ and E_A^* are defined in the text.

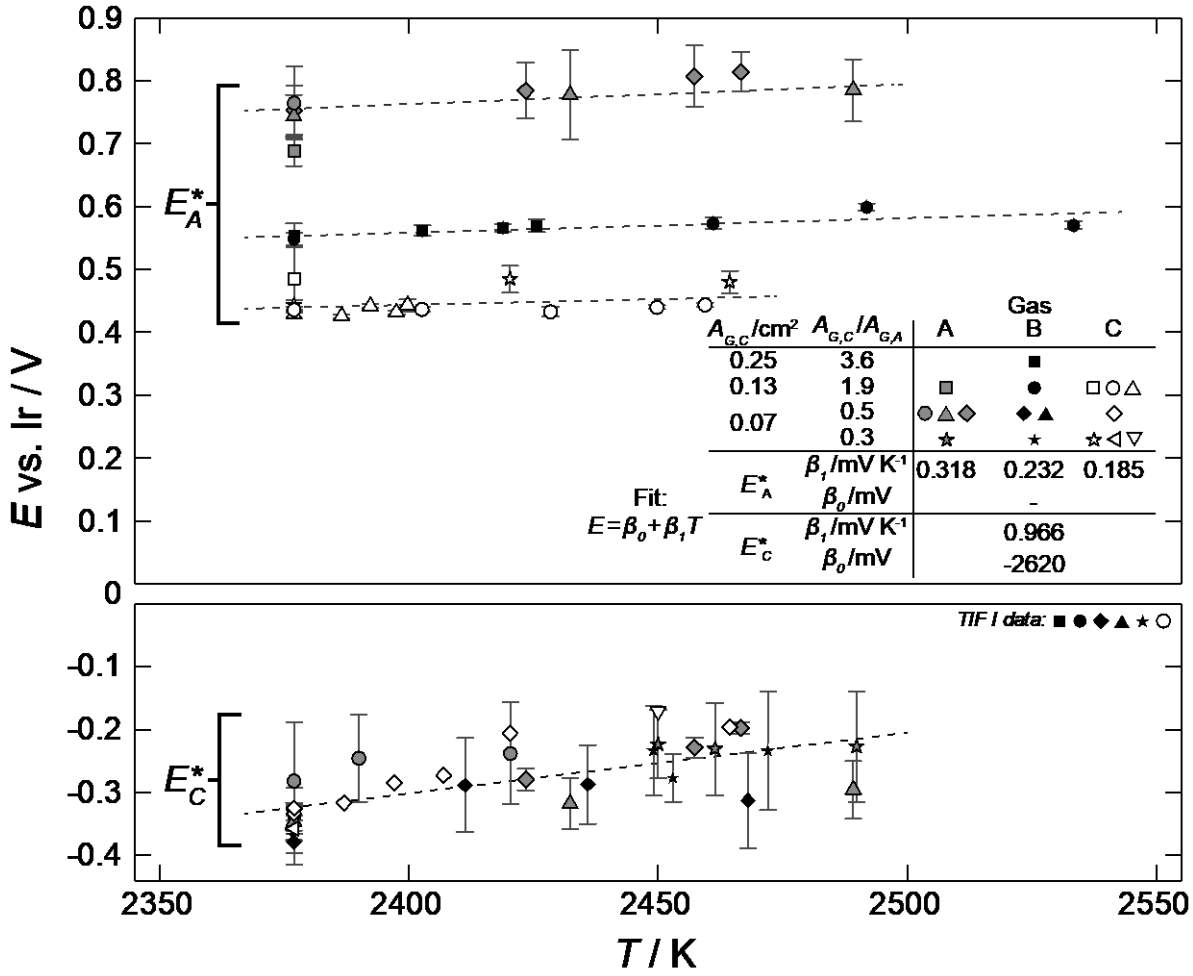

807

808 Figure 4. Variation of E_A^* (top) and E_C^* (bottom) with temperature for various electrode configurations and
809 gas atmospheres (error bars represent 1σ uncertainty from multiple scans in both cathodic and anodic
810 directions and lines show fitting according to $E = \beta_0 + \beta_1 T$). Note, E_A^* was fitted with a single, first-
811 order parameter (β_1), and E_C^* was fitted with zeroth (β_0) and first-order (β_1) parameters.

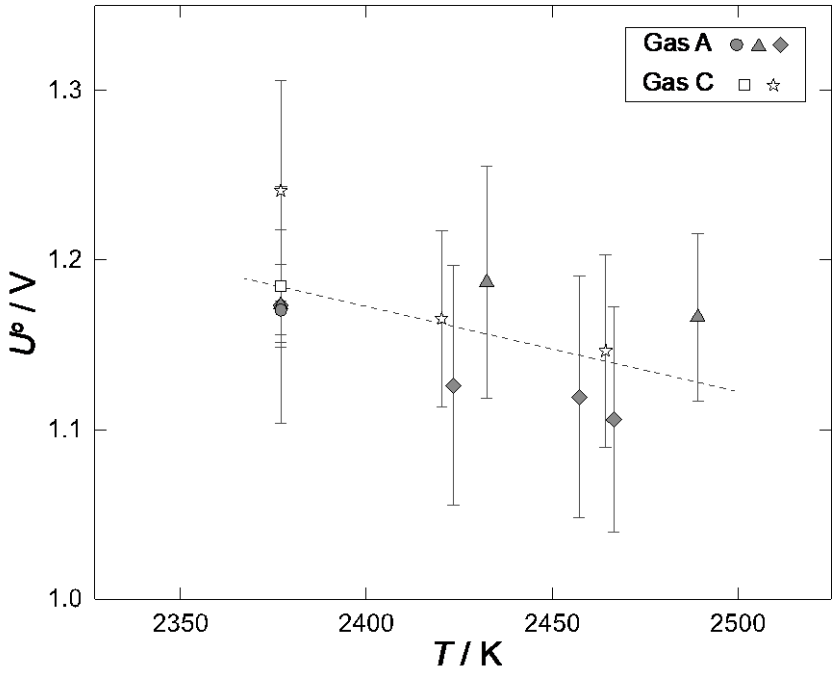

812

813 Figure 5. Variation of U^o versus temperature for Gases A and C. Linear fit of data (dashed line, U^o =

814 $\beta_0 + \beta_1 T$) yields β_0 = 2380 +/- 570 mV, β_1 = -0.50 +/- 0.24 mV K^{-1}.

815

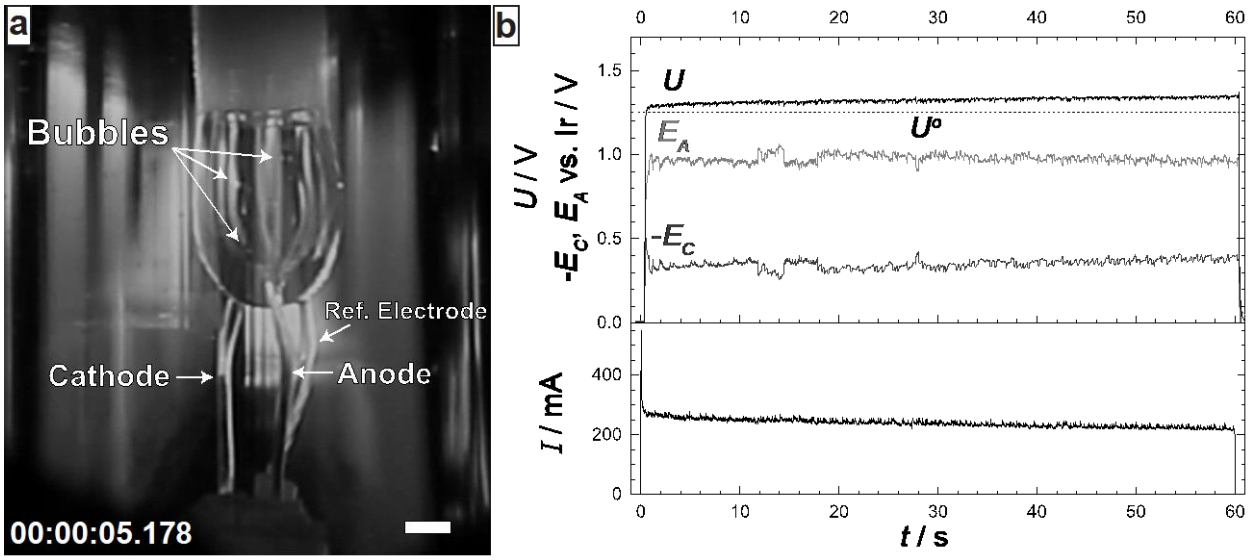

Figure 6. **a.** Droplet and electrodes during galvanostatic electrolysis (scale bar 2 mm). Bubbles are observed at the droplet surface near the anode (source video in supplementary materials). **b.** Anode (E_A) and cathode (E_C) potentials, cell voltage (U), and current (I) during potentiostatic electrolysis at 1.6 V applied cell voltage; at t = 60 s, the lamps were shut off (Q = 14.32 C, $A_{G,C}$ = 0.07 cm^2, $A_{G,C}$ = 0.25 cm^2, T = 2465 K, Gas C; source video in supplementary materials).

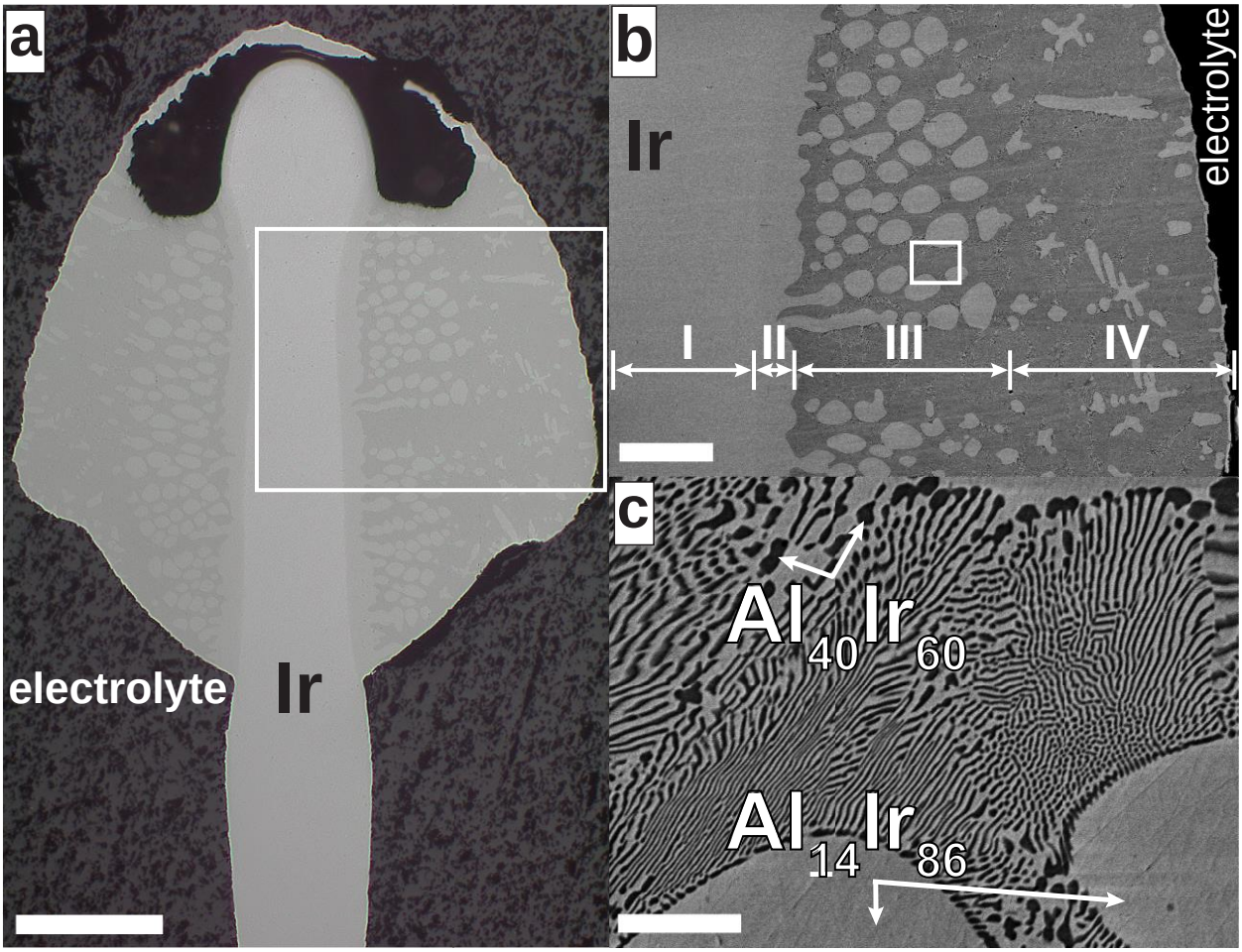

Figure 7. **a.** Optical micrograph of cathode cross-section after experiment shown in Figure 6b. (scale bar 300 µm). **b.** BSE image of boxed area in **a.** (scale bar 100 µm). **c.** High-magnification BSE image of boxed area in **b.** revealing the resultant solidified microstructure (scale bar 10 µm, quantitative analysis from EDS).

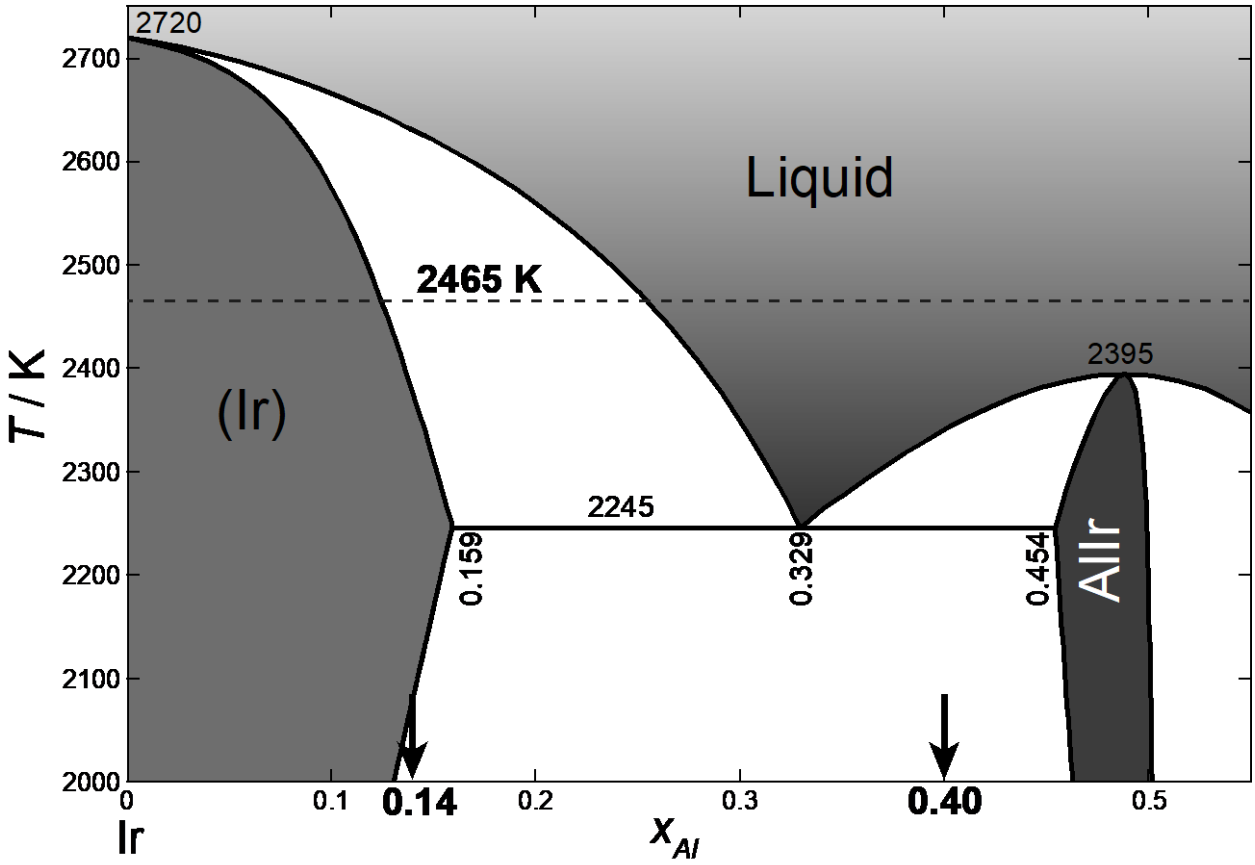

Figure 8. Ir-rich portion of the Ir-Al phase diagram calculated using FactSage [54] using the optimized parameters of Abe et al [2]. The approximate temperature during electrolysis is shown by the dashed line; arrows mark the alloy phase compositions observed upon solidification of the cathode after potentiostatic electrolysis, cf. Figure 7a-c.

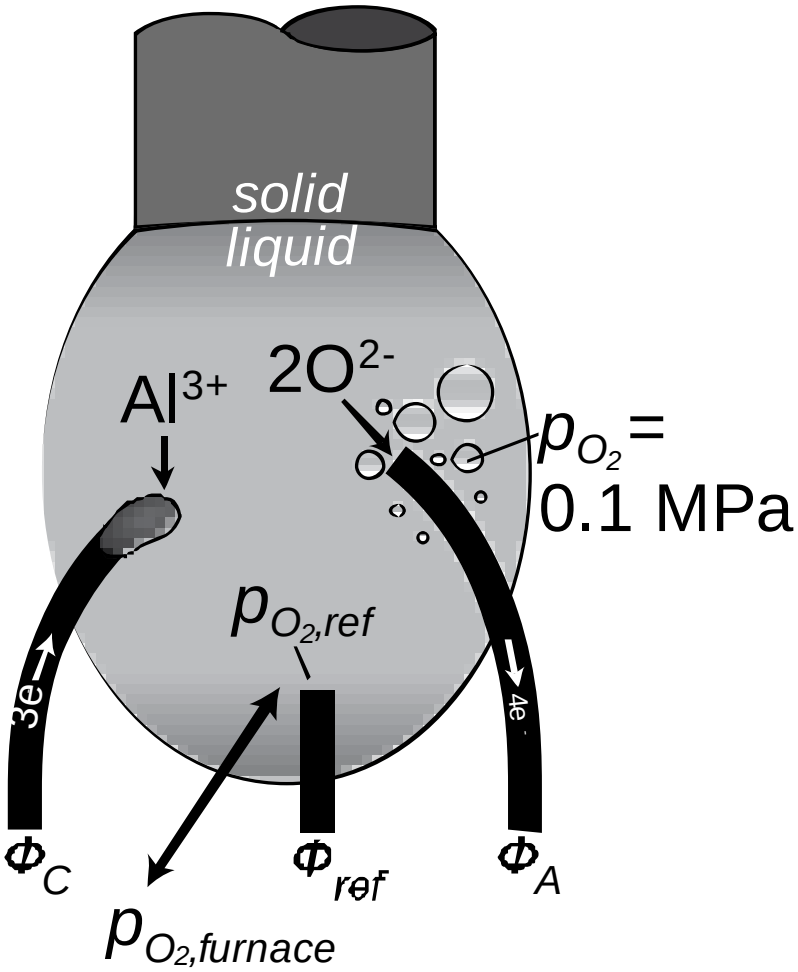

Figure 9. Electrochemical situation for the droplet and electrodes during cell polarization $U > U(E_C^*) > U(E_A^*)$. ϕ_C, ϕ_{ref} and ϕ_A are the inner electric potentials of the cathode, RE and anode, resp. Details described in text.

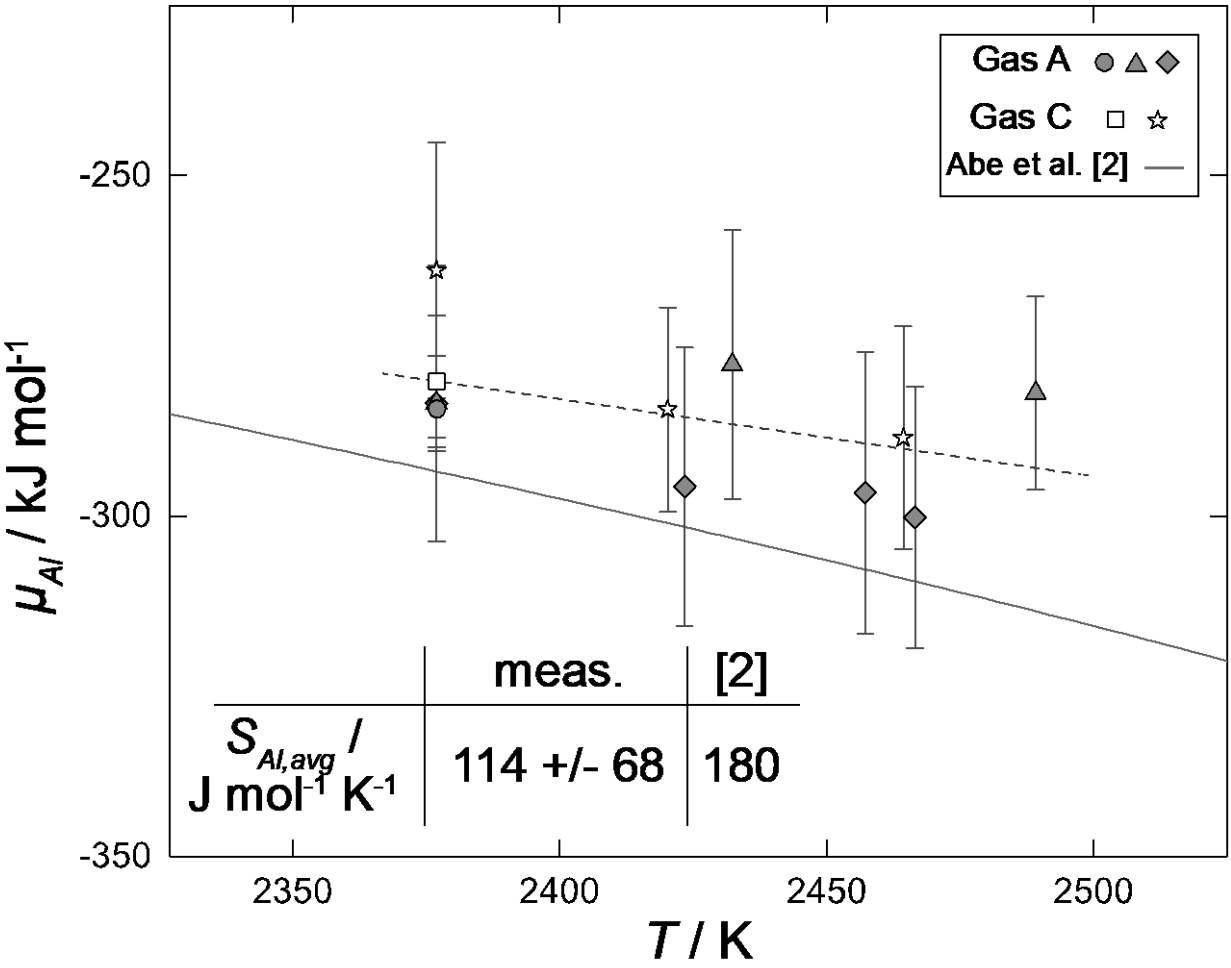

841

842 Figure 10. Variation versus temperature of the measured chemical potential (μ_{Al}) and average partial
843 molar entropy (S_{Al}) of Al at the solid-liquid phase boundary of the Ir-rich portion of the phase diagram;
844 linear fit (dashed line). Shown for comparison are those values calculated from the recent thermodynamic
845 assessment [2].

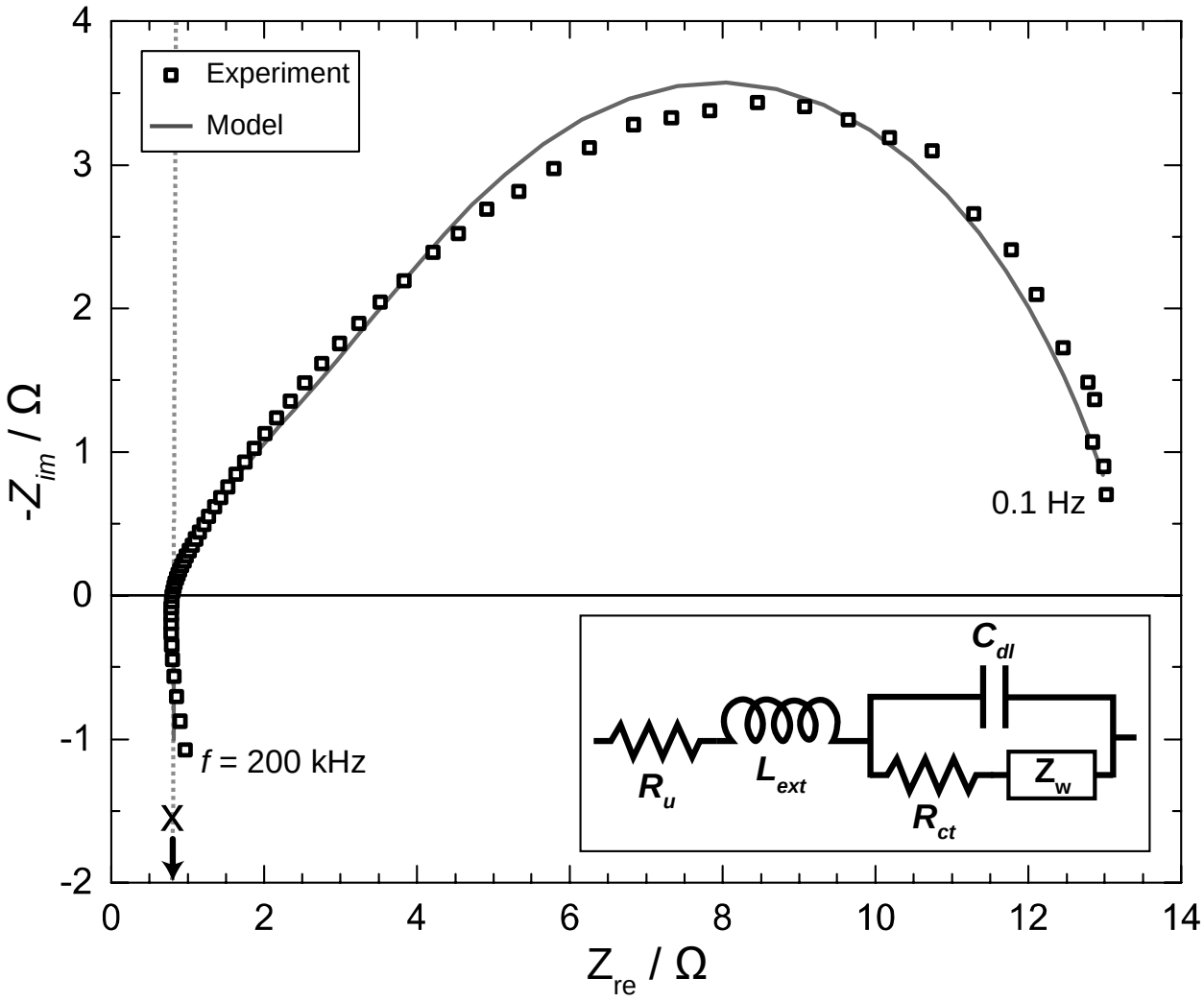

846

847 Figure A1. Impedance spectrum recorded at open circuit. The experimental data points are shown along
848 with the model fit. Model parameters are reported in Table A1. E_{ac} = 10 mV, f = 200 kHz to 0.1 Hz with
849 10 points per decade, P_L = 55%, Gas C, and $A_{G,WE}$ = 0.07 cm^2 and $A_{G,CE}$ = 0.13 cm^2, approx. TIF I was
850 employed to obtain the data shown here.

851 Table A1. EIS Fitting Parameters

852 TIF I was employed to obtain the data shown here.

853 *Arbitrarily fixed parameters, required for least-squares fitting convergence

Gas	P_L/ %	L_{ext}*/ µH	R_{ct}*/ 10^{-8} ohm	R_u/ mohm	C_{dl}/ µH	R_W/ ohm	T_W/ ms	P_W/ 10^{-3}
B	56	0.8	1	704 (6)	396 (36)	5.7 (0.1)	330 (30)	355 (6)
	57			691 (6)	404 (38)	5.5 (0.1)	340 (30)	404 (6)
	58			678 (6)	435 (43)	5.0 (0.1)	350 (30)	435 (6)
	59			674 (6)	454 (44)	4.7 (0.1)	370 (30)	454 (5)
C	55	0.8	1	814 (6)	154 (8)	12.6 (0.1)	280 (10)	371 (4)
	56			794 (6)	170 (9)	10.7 (0.1)	260 (10)	370 (4)
	57			772 (5)	197 (11)	9.5 (0.1)	260 (10)	368 (4)
	58			753 (5)	225 (13)	8.5 (0.1)	260 (10)	367 (4)
	59			743 (5)	252 (15)	7.6 (0.1)	260 (10)	366 (4)

854

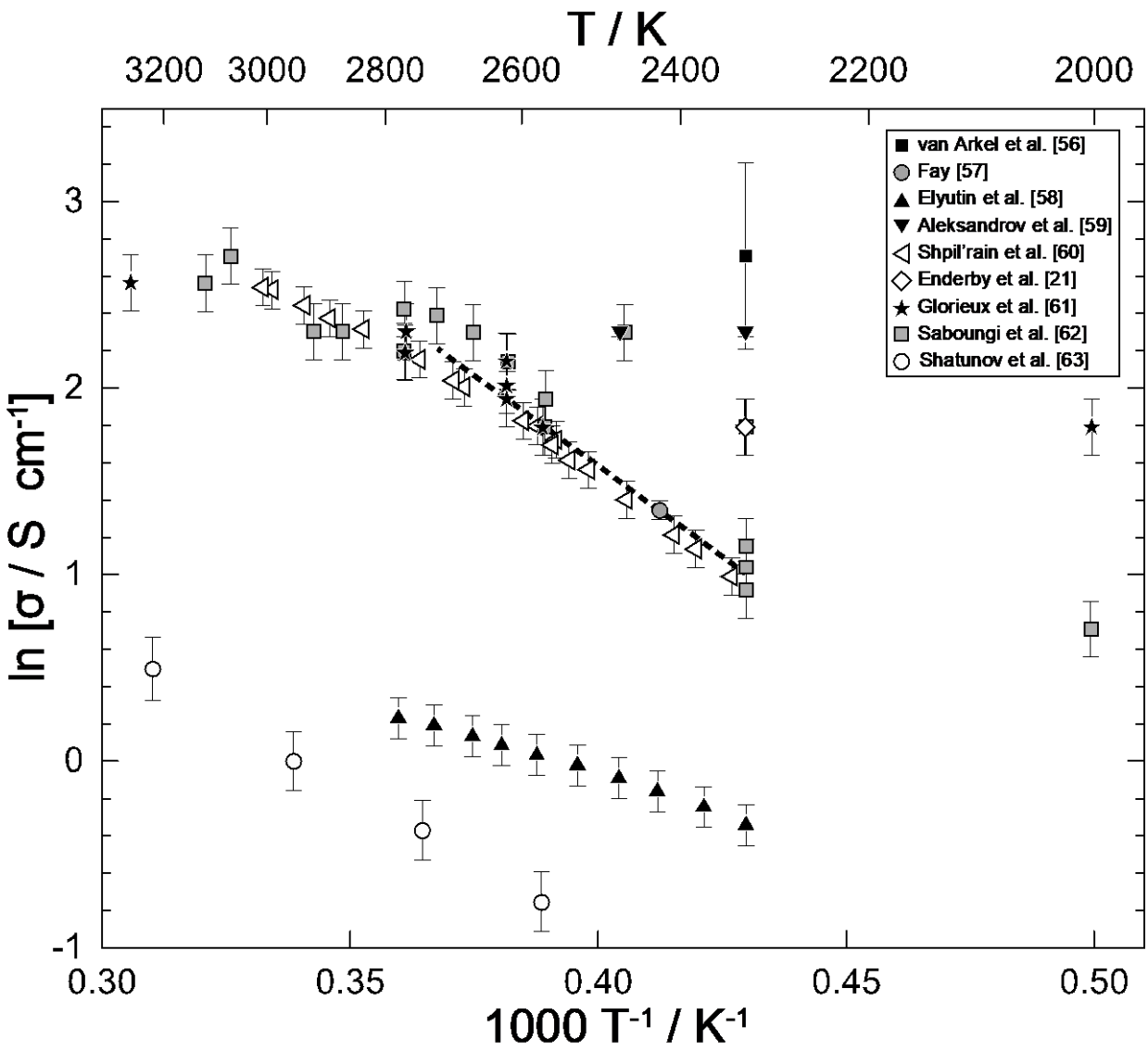

855

856 Figure C1. Arrhenius plot comparing previously reported conductivity measurements for Al_2O_3 (l).
857 Comparing the fit (dashed line, see text for details) with Eq. (B1), the activation energy of conductivity
858 E_σ and Arrhenius pre-exponential factor σ_0 were found to be 1.67 +/- 0.15 eV and 11 +/- 8 kS cm^{-1}, resp.
859 for the temperature range $T_m(Al_2O_3)$ = 2327 K [64],[65] to T_m(Ir) = 2719 K [65],[66].